Development of diode end-pumped Nd:YLF lasers at 1314 nm for high power operation

by

Roelof Cornelis Botha

Thesis presented for the degree of Doctor of
Philosophy in Physics
at the Stellenbosch University

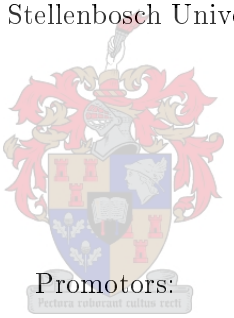

Promotors:

Prof. Ludwig Combrinck
Hartebeesthoek Radio Astronomy Observatory

Prof. Hubertus von Bergmann
Department of Physics
Stellenbosch University

Dr. Hencharl Strauss
CSIR National Laser Center

March 2016

Declaration

By submitting this thesis/dissertation electronically, I declare that the entirety of the work contained therein is my own, original work, that I am the sole author thereof (save to the extent explicitly otherwise stated), that reproduction and publication thereof by Stellenbosch University will not infringe any third party rights and that I have not previously in its entirety or in part submitted it for obtaining any qualification.

December 2015

Abstract

Development of diode end-pumped Nd:YLF lasers at 1314 nm for high power operation

Roelof Cornelis Botha

Hartebeesthoek Radio Astronomy Observatory, PO Box 443, Krugersdorp, 1740, South Africa

University of Stellenbosch, Private Bag X1, Matieland, 7602, Stellenbosch, South Africa

CSIR National Laser Centre, PO Box 395, Pretoria, 0001, South Africa

High-power 1.3 µm solid-state lasers have a wide range of scientific and commercial applications such as ultra-high resolution spectroscopy and red-green-blue (RGB) display technologies. The Hartebeesthoek Radio Astronomy Observatory (HartRAO) is currently developing a new Lunar Laser Ranging (LLR) system. This new system is a next-generation space geodetic instrument and is being developed with the objective to measure sub-centimeter orbital positions of the Moon. Initially it will use an Nd:YAG laser with a beam quality of $M^2 \sim 2$, which will lead to an estimated return photon detection rate of $\ll 1$ photon per laser pulse. Using a laser host material that can deliver high pulse energies but with a better beam quality will result in less beam divergence, to enable the detection of more return photons.

Nd:YLF as a birefringent laser host material is a promising alternative to Nd:YAG due to its ability to deliver high pulse energies as well as operate with a very good beam quality. The σ-polarization emission should result in a weaker thermal lens than for the π-polarization, due to the weakly negative thermo-optical coefficient dn_o/dT associated with it. Operating Nd:YLF on the σ-polarization wavelength of 1314 nm will allow us to quantify a lower limit for laser energy during 1053 nm operation, due to the lower emission cross-section σ_{em} that 1.3 µm has relative to 1.0 µm.

The growth process of Nd:YLF crystals results in a natural doping gradient. By using a relatively low average Nd doping concentration within the YLF crystal as well as pumping from the lower-doping crystal end-face, one can reduce energy transfer upconversion (ETU) which, in turn, reduces excited-state absorption (ESA). A reduction in the Nd doping therefore helps to lower the thermal load as well as spread it out longitudinally in the crystal. This increases the thermal fracture pump limit, allowing operation at higher pump power.

The power-scaling of 1314 nm Nd:YLF lasers was investigated for CW, passively as well as actively Q-switched operation. Both a single- and a dual-crystal resonator were designed and built. These lasers were operated in the CW and Q-switched modes. Passively Q-switched operation was achieved by using a V:YAG saturable absorber while actively Q-switched operation was achieved by using an acousto-optic modulator (AOM).

Power-scaling of 1314 nm Nd:YLF lasers was successfully demonstrated for CW, passively and actively Q-switched operation. It was concluded that 1314 nm Nd:YLF exhibits a netto positive thermal lens at high pump powers, this result being ascribed to the positive lensing effect from end-face bulging being slightly more pronounced than the negative thermo-optical coefficient dn_o/dT. The CW power and pulse energies obtained were higher than reported at that stage for any Nd-doped 1.3 µm lasers in an end-pumped configuration. These results indicate that Nd:YLF is an ideal active medium to obtain high power and energies for lasers operating in the 1.3 µm region, and that further power-scaling of 1.0 µm Nd:YLF should also result in very high output power and pulse energies, with an expected beam quality of $M^2 < 2$. The successful energy-scaling of σ-polarization $Q-$switched Nd:YLF lasers enables the subsequent investigation of mode-locked Q-switched (< 20 ps) pulses at the millijoule level, which are applicable to laser ranging.

Opsomming

Die ontwikkeling van hoë-krag diode end-gepompte Nd:YLF 1314 nm lasers

Roelof Cornelis Botha
Hartebeesthoek Radio-Astronomie Observatorium, Posbus 443, Krugersdorp, 1740, Suid Afrika
Universiteit van Stellenbosch, Privaat Sak X1, Matieland 7602, Stellenbosch, Suid Afrika
CSIR National Laser Centre, Posbus 395, Pretoria 0001, Suid Afrika

Hoë-krag 1.3 µm lasers het 'n wye verskeidenheid van wetenskaplike en kommersiële toepassings soos ultra-hoe resolusie spectroskopie en vertoningstegnologieë. Die Hartebeesthoek Radio-Astronomie Observatorium (HartRAO) ontwikkel tans 'n Maan-laser-afstandstaster. Dit is 'n nuwe generasie geodetiese instrument en poog om, as hoofdoel, sub-sentimeter wentelbaan posisies van die maan te meet. Aanvanklik sal 'n Nd:YAG laser met 'n geskatte straal-gehalte van $M^2 \sim 2$ gebruik word. Dit het 'n weerkaatsings-foton metingstempo van $\ll 1$ foton per laserpuls. Die gebruik van 'n laser materiaal wat hoë puls-energie met 'n beter straalkwaliteit kan lewer, sal lei tot 'n laer divergensie en 'n hoër weerkaatsings-foton metingstempo.

Die dubbelbrekende Nd:YLF laser kristal is 'n belowende plaasvervanger vir Nd:YAG aangesien dit hoë-energie pulse met 'n baie goeie straalkwaliteit kan lewer. Uitstraling van die σ-polarisasie behoort te lei na 'n swakker termiese lens as vir die π-polarisasie as gevolg van die swak negatiewe termo-optiese koëffisiënt dn_o/dT wat dit het. 'n Ondersoek van 1314 nm σ-polarisasie Nd:YLF werking sal ons in staat stel om 'n onder-limiet te bepaal vir die laser energie tydens 1053 nm werking, aangesien 1.3 µm 'n baie laer emissie-deursnit het as 1.0 µm.

Die groei-proses van Nd:YLF kristalle lei tot 'n natuurlike doperingsgradient. Deur 'n relatiewe lae Nd doperingskonsentrasie in die YLF kristal te gebruik en dan vanaf die laer-doperingskant te pomp, stel dit mens in staat om energie-oordrag-opwekking te verminder wat gevolglik weer opgewekte-toestand-absorpsie verminder. 'n Verlaging in die Nd-dopering maak die termiese las dus minder en versprei dit deur die kristal in 'n longitudinale rigting. Dit verhoog die termiese kraak pomplimiet wat mens in staat stel om 'n hoër pomp-intensiteit te gebruik.

Ondersoek van die krag-opgradering van 1314 nm Nd:YLF lasers vir kontinuë-straal, passiewe Q-skakelende en aktiewe Q-skakelende werking is gedoen. Beide 'n enkel- en dubbel-kristal resonator is ontwerp en gebou. Hierdie lasers is beide in die kontinuë-straal en Q-skakelende opstellings gebruik. Passiewe Q-skakelende werking is verkry deur van 'n V:YAG versadigbare absorbeerder gebruik te maak en aktiewe Q-skakelende werking deur van 'n akoesties-optiese-modulator gebruik te maak.

Die krag-opgradering van 1314 nm Nd:YLF lasers vir kontinuë-straal en Q-skakelende opstellings is suksesvol gedemonstreer. Die gevolgtrekking was dat 1314 nm Nd:YLF by 'n hoë pomp-intensiteit 'n netto positiewe termiese lens het. Dit kan toegeskryf word aan die effense positiewe lens vanaf die eindpunt uitbulting wat sterker is as die negatiewe termo-optiese koëffisiënt dn_o/dT. Die kontinuë-straal-krag en puls-energieë wat verkry is, was in daardie stadium hoër as enige gepubliseerde waardes vir alle eind-gepompte Nd-gedopeeerde 1.3 µm lasers. Hierdie resultate dui aan dat Nd:YLF ideaal is om 1.3 µm lasers met hoë-krag en -energie te verkry. Verdere krag-opgradering van 1.0 µm Nd:YLF behoort baie hoë uitsetkrag en pulsenergieë te lewer met 'n straalkwaliteit van $M^2 < 2$. Die demonstrasie van effektiewe krag-opgradering van 1314 nm Q-skakelende Nd:YLF lasers stel mens in staat om geslote-modus Q-skakelende pulse (< 20 ps) teen milli-Joule vlak, toepaslik vir laser-afstandstasters, te ondersoek.

Acknowledgements

During the course of this research and write-up I have been supported by many people, whose help and encouragement made the conclusion of this work possible.

I would like to thank Prof. Ludwig Combrinck for his continuous support in this research. The initial training and guidance received from Dr. Christoph Bollig and subsequently from Dr. Hencharl Strauss is greatly appreciated. I also appreciate the guidance and in-depth knowledge received from Prof. Hubertus von Bergmann.

The support and encouragement received from all my colleagues at HartRAO helped to make this project a success. A big *Thank you* to my all my family members and friends who supported me through the easier and more difficult parts of the past few years.

The author hereby also acknowledges the financial support received from the Hartebeesthoek Radio Astronomy Observatory and the Inkaba yeAfrica project.

Contents

List of Figures

List of Tables

Lists of Abbreviations and Frequently Used Symbols

Abbreviations

AOM	**Acousto-Optic Modulator**
CC	**Concave**
CW	**Continuous Wave**
CX	**Convex**
ESA	**Excited State Absorption**
ETU	**Energy Transfer Upconversion**
FWHM	**Full Width at Half Maximum**
GNSS	**Global Navigation Satellite Systems**
HartRAO	**Hartebeesthoek Radio Astronomy Observatory**
HR	**Highly Reflective**
HT	**Highly Transmissive**
IC	**Input Coupler**
Laser	**Light Amplification by the Stimulated Emission of Radiation**
LLR	**Lunar Laser Ranger**
NA	**Numerical Aperture**
Nd:YAG	**Neodymium-doped Yttrium Aluminium Garnet**
Nd:YLF	**Neodymium-doped Yttrium Lithium Fluoride**
Nd:YVO_4	**Neodymium-doped Yttrium Orthovanadate**

OC **Output Coupler**

PID **Proportional-Integral-Derivative**

PRF **Pulse Repetition Frequency**

RF **Radio Frequencies**

SLR **Satellite Laser Ranging**

V:YAG **Vanadium-doped Yttrium Aluminium Garnet**

VBG **Volume Bragg Grating**

VLBI **Very Long Baseline Interferometry**

YAG **Yttrium Aluminium Garnet**

YLF **Yttrium Lithium Fluoride**

YVO_4 **Yttrium Orthovanadate**

Frequently Used Symbols

α_{th} **Thermal expansion coefficient**

E **Photon energy**

η_o **Optical link efficiency**

f_{th} **Focal length due to thermal lensing**

G_t **Transmitter gain**

I **Current**

k_{th} **Thermal conductivity**

L **Distance between mirrors**

λ **Photon wavelength**

M^2 **Beam quality factor**

n_o, n_e **Refractive index along the a- and c-axis respectively**

dn_o/dT **Thermo-optical coefficient**

n_t **Number of transmitted photons**

N_x **Number of atoms in energy level x**

n_d **Number of detected return laser photons**

ν **Photon frequency**

w_0 **Beam radius at the waist**

P **Power (laser / pump)**

q_{defect} **Quantum defect**

R_{object} **Range to the object**

ρ_0 **Transverse atmospheric coherence length**

σ_{abs} **Absorption cross-section**

σ_{em} **Emission cross-section**

σ_{esa} **Excited-state absorption cross-section**

σ_{gsa} **Ground-state absorption cross-section**

T **Temperature**

τ **Decay rate half life**

θ_{pe} **Beam pointing error**

θ_t **Far field divergence half-angle**

Chapter 1

Background and Motivation

The Hartebeesthoek Radio Astronomy Observatory (HartRAO) Space Geodesy Programme is currently developing a Lunar Laser Ranger (LLR) (Combrinck and Botha, 2013; Botha and Combrinck, 2013). The primary system goal is to achieve sub-centimeter lunar orbital positions. These data can then be used for precise Lunar ephemeris, tests of the General Theory of Relativity and determination of the time-dependence of the universal gravitational constant, $\dot{G}$ (Guochang, 2012). This LLR system is envisioned to also be utilized for various other secondary tasks like Satellite Laser Ranging (SLR), time transfer experiments (Degnan, 2002; Prochazka et al., 2011) and laser deep space communication, similarly as done by Sun et al. (2013). The system will initially be operated with Nd:YAG lasers, as these have been employed traditionally for SLR and LLR. Since our system has an expected return photon detection rate of $\ll 1$ photon per transmitted laser pulse (Ndlovu et al., 2015), an investigation was made into other laser host materials. An increase in the return photon detection rate will greatly increase data points and thus lower the error margins of calculated orbits. The use of Nd:YLF as a laser host material has promising possibilities due to the high pulse energies it can deliver as well as the expected high beam quality, especially when operated at extremely high pulse energies.

Nd:YLF as a laser host material is a promising alternative to Nd:YAG because it should be able to deliver higher pulse energies (due to the longer excited state lifetime τ) as well as deliver a better beam quality, especially on the σ-polarization. Operating Nd:YLF on the σ-polarization wavelength of 1314 nm will:

- allow us to quantify a lower limit for laser energy during 1053 nm operation, due to the higher emission cross-section σ_{em} that 1.0 µm has relative to 1.3 µm
- result in a higher thermal load within the gain medium than for 1.0 µm operation. By obtaining the beam quality M^2 for 1.3 µm operation one can quantify the upper limit to the M^2 one can expect for 1.0 µm operation.

High-power 1.3 µm lasers also have a wide range of applications in remote sensing, free-space optical communication and display technologies (see Section 1.2.2).

1.1 Lunar Laser Ranging as a Geodetic technique

1.1.1 Space Geodesy

Geodesy is the scientific discipline which deals with the continuous measurement and representation of the Earth, especially the time-varying shape and gravitational field. It is an inter-disciplinary branch of applied mathematics and Earth sciences but uses techniques from various other scientific disciplines such as physics, engineering and statistics. Global and national measurement and control networks, using space and terrestrial techniques, are designed, implemented and maintained, to establish datums and coordinate systems as well as to measure various types of data within these reference systems. These coordinate systems, datums and datasets are then used to study geodynamical phenomena such as crustal and polar motion as well as global change.

The Hartebeesthoek Radio Astronomy Observatory (HartRAO) is located near Johannesburg in South-Africa and hosts research programmes in both Radio Astronomy as well as Space Geodesy. Space Geodesy is the practice of Geodesy using space-based techniques such as astronomical sources and satellites. The HartRAO Space Geodesy Programme currently hosts 4 main space geodetic techniques at the same site:

1. Very Long Baseline Interferometry (VLBI) using radio telescopes, to accurately determine datums for the celestial reference frame as well as the changing position and orientation of Earth in space.

2. Global Navigation Satellite Systems (GNSS) using satellite positioning systems such as Global Positioning System (GPS), to tie the celestial and several terrestrial reference frames together.

3. Satellite Laser Ranging (SLR) which uses laser pulses to determine the orbits of various scientific-mission satellites, as well as to calibrate the orbital data of GNSS satellites.

4. A DORIS station, using the Doppler effect to precisely determine satellite orbits, is also located nearby.

The combination of these four fundamental geodetic techniques on one site establishes HartRAO as one of only seven core sites in the international network and it is the only site of it's kind on the African continent. This, together with the LLR development, enables HartRAO to play an important role in the international network, especially in the development of new geodetic technologies and towards achieving millimetre-level precision.

1.1.2 Laser Ranging

Geodesy utilises both Satellite as well as Lunar Laser Rangers. These systems utilize corner cube reflectors on satellites or the reflector arrays, which were placed at various locations on the Moon during the Apollo and Lunakhod missions, as targets. The rangers operate by transmitting short laser pulses to these corner cube reflectors and then detect the reflected light signal via a large optical telescope. The transmitted and received pulses are time-tagged at the pico-second level to determine the effective distance the laser light travelled.

To attain the desired sub-centimeter accuracies the timing and detection systems needs to be accurate to $\leq 20\,\text{ps}$ (since $1\,\text{ps} \equiv 0.15\,\text{mm}$ for the final range) and laser pulses with pico-second time duration are required.

The expected number of detected return laser photons n_d for a laser ranger are given by the modified radar equation (Degnan, 1993), which can be simplified to:

$$n_d = \eta_o G_t \left(\frac{1}{4\pi R_{object}^2} \right)^2 n_t \tag{1.1}$$

with η_o the overall optical link efficiency, G_t the transmitter gain, R_{object} the range and n_t the number of transmitted photons. The main factor that influences the number of detected return photons n_d adversely is the distance R_{object}, since it results in a quadratic decrease in the photon density for each of the transmit and return paths due to beam divergence (the R^{-4} in Equation 1.1). Satellite and Lunar orbit ranges typically imply that $R_{sat}^{-4} \sim 10^{-9} - 10^{-18}\,\text{m}^{-4}$ and $R_{Lunar}^{-4} \sim 10^{-34}\,\text{m}^{-4}$ respectively, giving a clear indication of just how low the expected photon detection rate is for LLR. For SLR one can expect $> 10^5$ photons as a return, while for LLR the expected return is at the single photon level. The effective maximum range of the system is when one can detect at least a single photon per $\sim$200 emitted pulses ($n_d \sim 0.005$) to obtain an appropriate signal to noise ratio, while ideally detecting an average of a single photon per laser pulse ($n_d \sim 1$) is preferred. Usually LLR systems operate at $n_d < 0.1$. Assuming that the optical path efficiency η_o is optimal, the number of detected LLR photons is influenced by either the number of transmitted photons n_t or the transmitter gain G_t. The transmitter gain is defined as

$$G_t\left(\theta_{pe}, \theta_t\right) = \frac{8}{\theta_t^2} \exp\left[-2 \left(\frac{\theta_{pe}}{\theta_t} \right)^2 \right] \tag{1.2}$$

with θ_t the far field divergence half-angle (between the beam centre and the $1/e^2$ point) and θ_{pe} the overall beam pointing error (the combined effects of the laser and the reflecting telescope) (Degnan, 1993). This factor is the ratio of the power flux density at the detector, relative to that of an isotropic energy source (since Equation 1.1 is deduced from the radar equation used in engineering). Since laser light is highly directional this gain factor is very large. Equation 1.2 is only valid for the simplistic case of an unobstructed outgoing Gaussian laser beam, just to give the reader a qualitative insight into the typical influence of the transmitter gain G_t on the number of detected photons n_d.

Laser beams can only have near-perfect parameters at best. Since ranging occurs through Earth's atmospheric layer to space and back, atmospheric effects (turbulence) play a major role in the beam quality. Even if one could start off with a near-perfectly collimated laser beam, the resulting beam after leaving Earth's atmosphere will be diverged. Atmospheric effects therefore imply a lower limit on the far-field beam divergence, defined as

$$\theta_{tmin} = \frac{\lambda}{\pi \rho_0} \tag{1.3}$$

with λ the photon wavelength and ρ_0 the transverse atmospheric coherence length. The transverse atmospheric coherence length is defined as the circular diameter over which the

RMS wavefront aberration is 1 radian, due to passage through the atmosphere. Equation 1.3 defines the theoretical lower limit assuming all other factors are ideal. Sites which are suitable for astronomical observatories and laser rangers usually have an atmospheric coherence length value of at least $\rho_0 \sim 100\,mm$ (Walters and Bradford, 1997). A typical lower limit to the divergence half-angle for a visible beam as it leaves Earth's atmosphere is therefore $\theta_{tmin} \sim 0.35$", assuming one started off with a near-perfect laser beam.

From Hodgson and Weber (2005), one can relate the laser beam quality M^2 to the actual beam divergence (through vacuum) by

$$\theta_t = \frac{4M^2\lambda}{\pi w_0} \tag{1.4}$$

where w_0 is the beam radius at the waist and $M^2 = 1$ defines a perfect laser beam while $M^2 > 1$ an imperfect beam. A lower laser M^2 factor provides for a wider range of beam waist choices (thus far-field divergence half-angles) at the laser ranger since the aperture of the transmitting telescope provides an upper limit to the beam waist w_0.

1.1.3 Lunar Laser Ranging

Since the inception of Satellite and Lunar Laser Ranging in the early 1960's, Neodymium-doped Yttrium Aluminium Garnet (Nd:YAG) based lasers have been the workhorses in these systems. These lasers are frequency-doubled and the 532 nm emission is used for ranging to satellites and the Moon. The beam quality of the Nd:YAG lasers employed for these Laser Ranging purposes usually falls in the range of $2 \leq M^2 \leq 4$ (Degnan, 1993) which leads to higher divergence as they travel through the atmosphere than for $1 \leq M^2 \leq 2$ beams. Thus changing the laser system to operate with a host material that can deliver a beam quality of $M^2 < 2$ will mean less divergence and a higher energy density in the beam which will ensure more return photons and increase overall system accuracy and efficiency.

Figure 1.1 depicts the influence of beam divergence on transmitter gain G_t, for a range of pointing errors that can realistically be achieved by HartRAO's Lunar Laser Ranger system. The transmitter gain can be increased dramatically by having a combination of a small pointing error and low beam divergence. A higher transmitter gain G_t implies that more return photons can be detected. Due to the expected typical pointing error of about 1.0" (1.0 arc-seconds) for the HartRAO LLR, we would like to aim for a beam divergence half-angle of between 1.0" and 2.0" as the beam leaves Earth's atmosphere. Furthermore, an ideal laser beam waist radius for the HartRAO LLR would be $\leq$20 cm at the telescope, due to the size and construction of the telescope. Using this beam waist range in Equation 1.4 and keeping in mind the minimum divergence contribution due to the atmosphere (Equation 1.3) one arrives at an ideal laser ranger beam quality range of $M^2 < 2$ for visible lasers (Equation 1.4). The expected pointing error of the HartRAO LLR system of about 1.0" implies that using a laser with a beam quality $M^2 < 2$ will result in less beam divergence, which will increase the transmitter gain G_t and thus ensure the detection of more return photons. Neodymium-doped Yttrium Lithium Fluoride (Nd:YLF) as a laser host material is a promising alternative to Nd:YAG because it should be able to deliver higher pulse energies as well as better beam quality, especially on the σ-polarization (see Section 1.2.1).

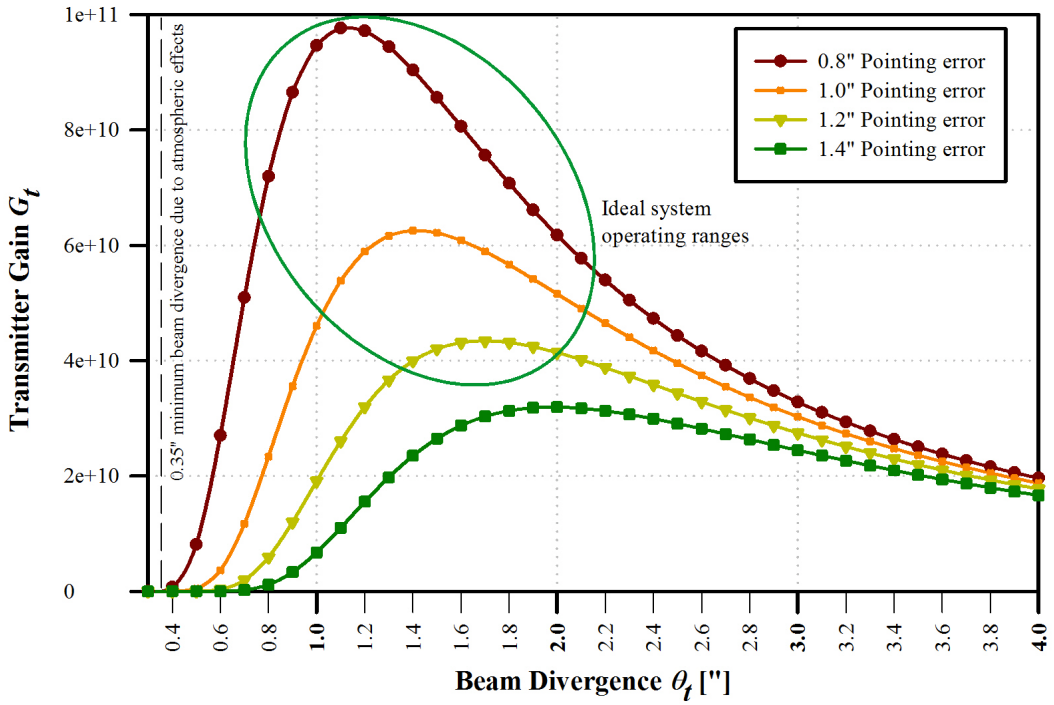

Figure 1.1: The influence of beam divergence on transmitter gain G_t, for various pointing errors.

1.2 High-power 1.3 µm Nd:YLF lasers

1.2.1 Nd:YLF as a laser host material

Since the initial investigation of its spectroscopic properties by Ryan and Beach (1992), Nd:YLF has increasingly been investigated due to it's potential to deliver high energy laser pulses with a good beam quality. The upper-laser-level ($^4F_{3/2}$) lifetime of $\tau \sim 520\,\mu s$ for Nd:YLF is longer compared to the $\sim 250\,\mu s$ for Nd:YAG (Ryan and Beach, 1992; Czeranowsky, 2002). The resulting high energy storage capability makes Nd:YLF suitable for generating high pulse energies during $Q-$switched operation (Ryan and Beach, 1992; Koechner, 1999; Czeranowsky, 2002; Bollig et al., 2010). Furthermore, operating Nd:YLF lasers is attractive due to the weak thermal lens when emitting on the σ-polarization (Pollnau et al., 1998b; Hardman et al., 1999). This results in the potential for an excellent beam quality over a wide range of output powers.

The main emission lines for Nd:YLF are around 1053 nm and 1314 nm for the σ-polarization. The 1314 nm emission cross-section is a factor of 6 lower than the emission cross section for 1053 nm Nd:YLF and a factor of 3 less than the that of Nd:YAG at 1.3 µm. Power scaling of 1.3 µm Nd:YLF lasers is therefore more difficult than for 1.0 µm Nd-lasers, however, the relatively long upper-laser-lifetime τ of Nd:YLF partially compensates for this.

Power-scaling of 1.0 µm has been investigated extensively by other groups (Pollnau et al., 1998a; Wetter and Deana, 2014) as well as our own group (Bollig et al., 2008; Koen, 2009; Bollig et al., 2010)and operation at sub-100 W power with very good beam qualities and high pulse energies have been demonstrated. CW output powers at 1053 nm delivered up

to 44 W from 110 W of absorbed pump power at 797 nm (optical-to-optical efficiency of 42%)(Wetter and Deana, 2014) and up to 87 W from 280 W of incident pump power at 806 nm (36.5% optical-to-optical efficiency of 36.5%) (Koen, 2009). Pulsed output from a 1053 nm Q-switched laser delivered up 10.4 mJ of energy per pulse (Bollig et al., 2010). The crystals and pump sources available to our group did not allow for power scaling of 1.0 µm to the levels required by LLR. We could however investigate power-scaling of 1.3 µm Nd:YLF since this would provide a lower limit expected for 1053 nm pulse energies when Q-switched, due to the lower emission cross-section σ_{em} for 1.3 µm relative to 1.0 µm. It would also provide an indication of the worst beam quality (upper limit to $M^2_{1.0}$) one could expect from 1.0 µm Nd:YLF that has been power-scaled and operated just below the thermal fracture limit.

As a laser material, Nd:YLF therefore has the potential in delivering both a good beam quality and high pulse energies for Laser Ranging (Section 1.1) and various other applications (Section 1.2.2). Investigating the power-scaling of 1.3 µm Nd:YLF lasers is therefore advantageous to a wide range of applications.

1.2.2 Some applications requiring high-power 1.3 µm lasers

High-power 1.3 µm lasers have a wide range of applications, including remote sensing, communications, timing systems, ultrahigh-resolution spectroscopy and display technology:

- The 1.3 µm output can be Raman-shifted to the 1.5 µm region, which is useful for applications requiring eye-safe operation at high powers such as Lidar and free-space optical communication (Murray et al., 1995).
- 1314.0 nm (specifically the 657.0 nm harmonic) is required to probe the relevant transition for optical Calcium clocks (Louyer et al., 2003). These optical clocks have a quality factor of $\sim 10^{15}$ compared to $\sim 10^{10}$ for their microwave counterparts such as Cs fountain clocks; Nd:YLF sources are therefore ideal candidates for next-generation high accuracy systems.
- Lasers are essential tools for probing fundamental theories using ultra high-resolution spectroscopy (Louyer et al., 2003). Tests of quantum electrodynamics and determination of some fundamental constants can be done by using 1.3 µm Nd:YLF lasers. Measurement of the $2S-3S$ interval in hydrogen with 1312.6 nm photons would help to better determine the Rydberg constant. Spectroscopy with 328.1 nm (second harmonic) of the He^+ $2S-3S$ resonance should provide a precise measurement of the $2S$ Lamb shift.
- Harmonic conversion of 1.3 µm can be used for the generation of red and blue light in red-green-blue (RGB) display technologies (Hu et al., 2008).

Pulsed high-power 1.3 µm lasers can benefit especially Lidar and free-space optical communication by increasing the operational distances as well as enable large-scale RGB display technologies. Power scaling of end-pumped 1.3 µm lasers was mainly investigated for Nd:vanadate gain media. Nd-doped 1.3 µm CW and Q-switched lasers were investigated

and compared for Nd:YAG, Nd:$YAlO_3$, Nd:YVO_4 and Nd:$YGdVO_4$ (Krennrich et al., 2008) for both CW as well as $Q-$switched modes. Both Nd:YVO_4 and Nd:$GdVO_4$ have an 1.3 µm emission cross section in the same order as for 1064 nm Nd:YAG (Czeranowsky, 2002). However, the vanadates exhibit a strong thermal lens, which is worsened by exited-state absorption (ESA) around 1340 nm (Fornasiero et al., 1998). In addition, their upper-laser-level lifetime is only 100 µs, limiting the available energy per pulse under continuous pumping. Nd-vanadate lasers can not easily produce ∼1314 nm radiation as required by some applications. Nd:YLF therefore should be able to deliver better beam quality than for vanadates, with a high pulse energy at a wavelength of ∼1.31 µm.

1.3 Conclusion and Experimental work

There is an international drive to develop new geodetic technologies, towards achieving millimeter-level precision in position measurements. The HartRAO Space Geodesy Programme has a core geodetic site as part of the international network and is currently developing a new Lunar Laser Ranging (LLR) system. This new LLR system is a next-generation space geodetic technique and aims to achieve sub-centimeter lunar orbital positions. Initially it will use a Nd:YAG laser with an estimated beam quality of $M^2 \sim 2$, which will lead to an estimated photon detection rate of $\ll 1$ photon per pulse (every 100 - 200 laser pulses will deliver one detected photon on average). If one can use a laser host material that will deliver better beam quality, it will result in less beam divergence which will increase the transmitter gain G_t and thus ensure the detection of more return photons.

The stronger 1.3 µm emission line of Nd:YLF is at 1314 nm for σ-polarization emissions, which has a weak negative thermal lens and should therefore deliver better beam quality than for the π-polarisation wavelength of 1321 nm. Nd:YLF as a laser host material is a promising alternative to Nd:YAG because it should be able to deliver higher pulse energies (due to the longer excited state lifetime τ) as well as deliver a better beam quality, especially on the σ-polarization. Investigating Nd:YLF operation on the σ-polarization wavelength of 1314 nm will:

- provide a lower limit expected for Q-switched 1053 nm pulse energies, due to the higher emission cross-section σ_{em} for 1.0 µm relative to 1.3 µm and
- enable us to quantify the highest 1.0 µm M^2 one can expect, due to the higher thermal load the gain medium experiences for 1.3 µm relative to 1.0 µm operation.

High-power 1.3 µm lasers also have a wide range of applications such as remote sensing and large-scale RGB display technologies.

Demonstration of the energy-scaling of σ-polarization $Q-$switched Nd:YLF lasers will enable subsequently investigation into mode-locked Q-switched (< 20 ps) pulses at the millijoule level, which are applicable to laser ranging. However, such experiments require stronger pump sources, longer Nd:YLF crystals rods of a low doping (for increased absorption), optics that will be able to handle the higher peak energies and additional optical elements to obtain mode-locking and pulse-picking. An investigation was therefore launched into the

power-scaling of 1.3 µm Nd:YLF lasers, both for CW as well as $Q-$switched operation. The lasers were operated at power levels just below the crystal damage threshold.

Chapter 2

Theoretical overview of laser operation

The basic physics of four-level lasers, as well as implementation of this knowledge to create a diode end-pumped solid-state laser for effective Continuous Wave (CW) and Q-switched operation, are reviewed in this chapter.

2.1 Laser operation at an atomic level

The term LASER is an acronym for *L*ight *A*mplification by the *S*timulated *E*mission of *R*adiation, hereafter referred to only as laser. Stimulated emission, first described by Einstein (1917), is the process whereby a photon with frequency ν can stimulate (influence) a nearby excited atom or molecule to release some or all of the excitation energy in the form of a photon with the same frequency (see Figure 2.1). The energy E and frequency ν of a photon is related by Planck's constant h through $E = h\nu$. Suppose one has an atom with a ground-state energy level E_1 and excited state level E_2. If this atom is in the excited state, the electron is in energy level E_2 (Figure 2.1(a)). If a photon with energy $E_{photon} = h\nu_{photon} \sim E_2 - E_1$ passes this excited atom, it stimulates the atom to make a transition back to the ground state E_1 (Figure 2.1(b)) by emitting a photon identical to the incident one (Figure 2.1(c)). This released photon is the same as the stimulating photon in terms of three important properties: energy, phase and propagation direction. The process of stimulated emission therefore amplifies light by creating an exact duplicate, or clone, of the incident photon. This amplification process is defined as gain and a material that can amplify light by the process of stimulated emission is called a gain medium.

Pumping and emission processes in real laser systems usually involve a large number

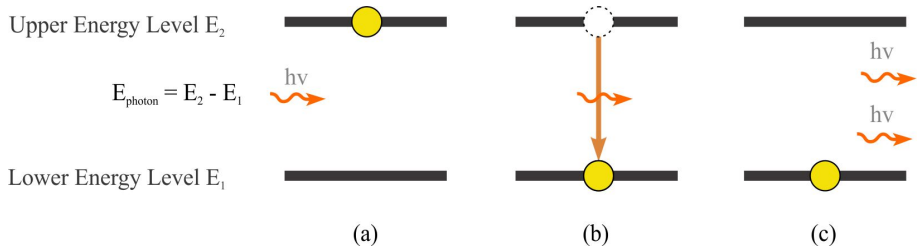

Figure 2.1: The process of stimulated emission, as first described by Einstein (1917).

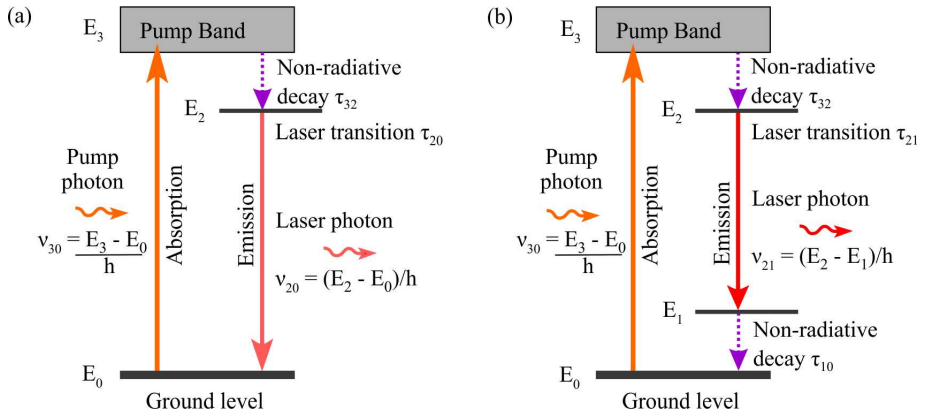

Figure 2.2: Simplified diagrams of laser operation: (a) a three-level and (b) a four-level lasing system. The dashed lines depict some possible heat-generating transitions (via multi-phonon relaxations), the solid lines indicate transitions involving photons.

of energy levels with complex excitation and cascaded relaxation processes between these different levels (Koechner, 1999). The main features of typical laser operation via the interaction of radiation and matter can be understood through the simplified three- and four-level diagrams as depicted in Figure 2.2. In this figure we explain the pumping as well as emission mechanisms which are central to the short discussion that follows.

In solid-state laser media, as discussed here, most of the energy level relaxation transitions of atoms are rapid non-radiative decay processes since there is a strong coupling between the internal atomic oscillations and the surrounding lattice (Koechner, 1999). This implies that the energy lost by an atom is transferred to vibrational and / or thermal energy within the lattice (see Section 2.5). Radiative decay processes can occur but these usually have short lifetimes and broad line widths. There are only a few transitions, associated with selected atomic elements, where the transitions are decoupled from the lattice vibrations (Koechner, 1999). Such transitions have a relatively long lifetime and lead to radiative decay with narrow line widths. These energy levels are called *metastable levels* and are crucial for laser action to occur.

Optically pumped three- and four-level lasers can be explained using Figure 2.2. The three-level laser are not used often due to the lower efficiency than for four-level systems, but is depicted in the figure for completeness. Four-level lasers are characteristic of rare earth ions in glass or crystalline host materials. Initially all atoms are in the ground state E_0. The atom can be excited to a wide absorption band (hereafter called the pump band) with energy E_3 if a photon with energy

$$E_{photon} \sim E_3 - E_0 \tag{2.1}$$

is absorbed by the atom. One would ideally like to excite a gain medium only to the pump band (E_3 in Figure 2.2). Most of the pump-band atoms are transferred into the intermediate sharply defined energy level E_2 by a fast non-radiative decay with half-life τ_{32}. The electron is now in a metastable level with a relatively long lifetime $\tau_{21} \gg \tau_{32}$ and can lose its associated energy via a radiative transfer to energy level E_1. This energy level E_1 has a

short lifetime $\tau_{10} \ll \tau_{21}$ and quickly decays via non-radiative processes to the ground state E_0.

The usual ground and pump bands as depicted by Figure 2.2 have associated energy levels E_0 and E_3. When a large collection of such similar atoms are in thermal equilibrium at temperature T, we know from statistical physics that the relative population of these two energy levels are related by the Boltzmann ratio, such that

$$\frac{N_3}{N_0} = \exp\left(\frac{-(E_3 - E_0)}{kT}\right) \tag{2.2}$$

with N_0 and N_3 the number of atoms in energy levels E_0 and E_3 respectively (Ohanian, 1995; Koechner, 1999). Typically the number of atoms in any upper energy level (excited state) will be extremely small at room temperature ($T = 300\,K$) if the energy gap corresponds to photons with energies $h\nu_{30}$ in the near-infrared or visible regions (from $E_3 - E_0 = h\nu_{30} \gg kT$). Since the lifetimes τ_{32} and τ_{10} are small compared to τ_{21} one can assume that the atom is either in metastable state E_2 or ground state E_0. Therefore, for thermal equilibrium, one can assume that the population is such that $N_0 \gg N_2$. Through the absorption of energy via some physical mechanism, one can obtain the situation in which more atoms are in the excited E_2 state (via state E_3 with a fast decay to E_2), than are in the ground state E_0. This implies that $N_0 \ll N_2$ and one has then effectively achieved a state called *population inversion*. The source of energy used to create the population inversion is called *pump energy* and photons are a good energy source to use in obtaining this population inversion.

The decay of metastable state E_2 usually occurs via spontaneous radiative decay. If a population inversion exists in the bulk material, the decay of metastable state E_2 will occur via spontaneous as well as stimulated emission. It is this process of stimulated emission that can be exploited to amplify light (multiply photons) and thus create a laser.

The intrinsic efficiency of the lasing action (the so-called quantum efficiency) is determined by the energy of the laser photon relative to the energy of the pump photon. The difference between these energies is lost via mostly heat-generating mechanisms within the material which are summarised in Section 2.5.1.

2.2 Laser operation at a macroscopic level

Figure 2.3 demonstrates the process whereby stimulated emission within a bulk material can be exploited to enable laser action. First one creates a laser resonator by positioning two reflectors to face each other so that they ensure a closed optical path between them. A closed optical path exists when a photon that passes a point in a certain directions within the resonator, will pass the same point again in the same direction after a finite time. The gain medium is placed within this optical path inside the resonator. The atoms within a gain medium are then excited by an external source of energy. A population inversion will occur within the gain medium, which causes both spontaneous and stimulated emission. If a photon of the right energy as per Equation 2.1 is spontaneously emitted along the resonator optical path, it causes a cascaded stimulated emission effect as it travels back and forth

along the resonator optical path. By choosing one of the reflector elements to be partially transmissive, some of the photons will leak out of the laser cavity, creating the laser beam.

Optical resonance is an important (and often essential) method to enable laser action. Within most gain media, the gain is not high enough to ensure efficient stimulated emission for laser action to occur. By reflecting light between two mirrors one can trap the optical wave between them (see Figure 2.4). A resonator is only stable as long as it ensures a stable periodic focussing or reflection system (Siegman, 1986) and if the mirrors have large enough transverse dimensions. Otherwise it is an unstable system. To test whether a resonator is stable the following equation needs to be valid:

$$0 < \left(1 - \frac{L}{R_1}\right)\left(1 - \frac{L}{R_2}\right) < 1,$$

with R_1 and R_2 the radii of curvature for mirrors 1 and 2 and L the separation between them. In addition to trapping the light between the mirrors, a resonator can only support certain spatial Eigen modes (shapes) (Siegman, 1986). A simple explanation is that any mode (shape) that does not reproduce itself after one round-trip, is not amplified sufficiently. The simplest functions (shapes) that are able to do this are the Hermite and Laguerre Gaussian functions (for rectangular and circular symmetry respectively). These types of waves are shape invariant as they propagate. The fundamental Gaussian mode is referred to as the Transverse Electromagnetic 00 (TEM_{00}) mode and has the classical Gaussian distribution. All the higher order modes have sizes that are larger than this mode. Usually

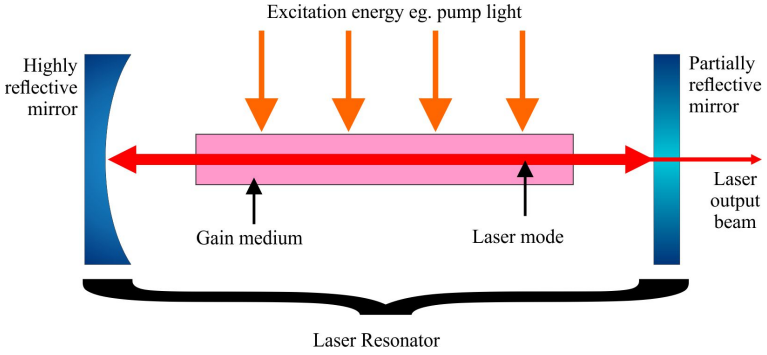

Figure 2.3: A basic side-pumped laser resonator setup.

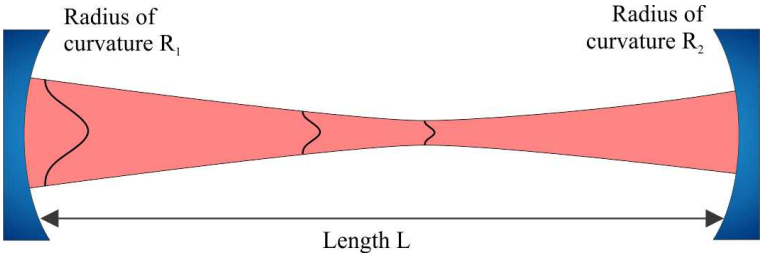

Figure 2.4: A resonator and some parameters used to define stable operation. Mirrors of the proper radii of curvature R_1 and R_2 and separation L can trap a Gaussian beam. The Gaussian intensity profile stays the same throughout the resonator, only the scale changes.

Dielectric constant	Crystallographic axis	Light with $E \parallel$ axis	Refractive index	Polarisation
κ_1	c-axis	extraordinary / e-ray	n_e	π-polarised
$\kappa_2 = \kappa_3$	a-axis	ordinary / o-ray	n_o	σ-polarised

Table 2.1: Polarisation summary for uni-axial birefringent crystals

one wants to select only the TEM_{00} mode. To do this, one changes the physical parameters of the cavity to introduce extra losses for the larger, higher order modes.

By pumping a gain medium within an optical resonator, laser action can be achieved and a laser beam will be emitted from the resonator through a partially reflective output-coupler (OC). This laser radiation is a collimated beam because the light is only amplified in a specific direction. It is also coherent and has a narrow wavelength range (monochromatic) due to the stimulated emission process. Laser radiation can be distinguished from other radiation mainly by it's coherence.

2.3 Birefringent gain media

Birefringence, also called double refraction, is a property of non-isotropic crystallographic materials. Most birefringent materials are uniaxial which means that they have the same dielectric constants for two of the three optical axes (the lines along which there are some degrees of rotational symmetry) (Hobbs, 2000). The crystallographic direction along the axis with the unique dielectric constant κ_1 is called the c-axis of the birefringent crystal, the other two axes are both called a-axes. Light polarised parallel to the c-axis is called an extraordinary ray (or e-ray) and light polarised perpendicular to this is called an ordinary ray (or o-ray). These plane polarised ordinary and extraordinary rays have different indexes of refraction n_o and n_e and, in solid state lasers, are said to be σ-polarised and π-polarised respectively.

If a birefringent crystal is used as a laser gain medium, the resulting laser is usually polarised along one of these crystallographic directions because of the difference in gain between the two axes (also see Sections 3.1 and 3.2). This results in the laser beam experiencing only a single refractive index n_o or n_e. Both these refractive indexes have near-linear temperature dependencies

$$\frac{dn_o}{dT} = C_o, \qquad \frac{dn_e}{dT} = C_e, \qquad C_o \neq C_e \neq 0 \tag{2.3}$$

and are also wavelength dependent

$$\frac{dn}{d\lambda} \neq 0, \tag{2.4}$$

with λ the wavelength of the light.

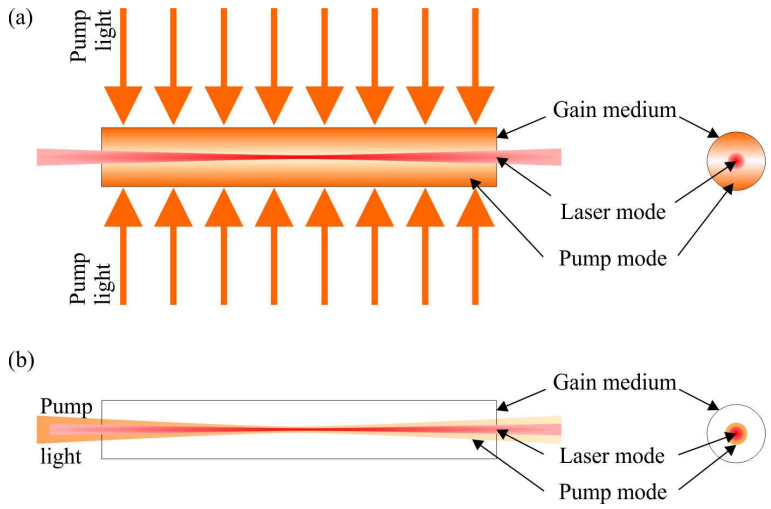

Figure 2.5: Schematic diagrams of pump schemes: (a) side-pumped and (b) end-pumped schemes, as applicable to laser rods.

2.4 Diode end-pumped solid-state lasers

Considering all viable sources of pump energy, optical sources are commonly used to achieve excitation to a metastable energy state within a solid-state gain medium (Hobbs, 2000). Typical optical pump schemes are side- and end-pumping, as demonstrated in Figure 2.5. The gain medium is usually shaped as a rod (round or square) or a flat disc. Side-pumping is usually employed for rods while end-pumping is usually employed for discs.

Side-pumping of rods has the disadvantage of exciting the whole gain medium while the resonator mode only extracts energy from a subsection of the gain medium. This leads to increased and inhomogeneous heat generation within the gain medium. Since the sides of the gain medium rods are utilised for pumping it rather than cooling, it leads to increased thermal effects (see Section 2.5).

In contrast, end pumping has two main advantages: 1) it can only excite the volume of the gain medium which overlaps to the resonator mode and 2) it leaves the sides of the gain medium accessible for implementing cooling mechanisms. These two advantages imply less heating of the gain medium, reduced detrimental thermal effects and therefore increased overall efficiency. One drawback of end-pumping is that one needs to employ special optics to separate the pump and laser light.

Optical pump sources can emit either in a spectral continuum, isolated spectral lines or a mix of broadened lines and continuum spectral bands (Hobbs, 2000). Commonly used broadband pump sources include flash lamps and arc lamps while narrowband sources include laser diodes.

Flash lamps and arc lamps used as an optical pump source have the advantage of delivering high pulse energies and peak powers for pulsed laser systems, but have the disadvantage of a low efficiency. The overall electrical to optical efficiency of lamp-pumped solid-state lasers generally only reaches a few percent. Other drawbacks include the low optical coupling efficiency into the gain medium, both due to the spectral characteristics of the emission

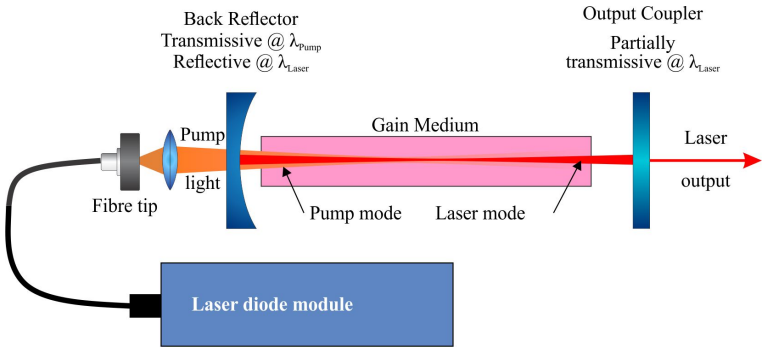

Figure 2.6: A schematic diagram of a typical diode end-pumped solid state laser.

not completely matching the gain media absorption spectra, as well as the low spatial coupling that can be achieved from the omni-directional emission source into the gain medium. The broad spectral emission will lead to excitation in the gain media to energy manifolds other than the pump band, such absorption will not contribute to laser action but rather to heat generation within the gain media. These types of optical sources also require bulky and hazardous high-voltage power supplies and the lamps themselves have a limited lifetime.

Laser diodes have high powers and narrow line widths (3 nm $\equiv$ 900 GHz) compared to other types of sources (Hobbs, 2000). They are also of the most efficient (electrical to optical), cost effective (cost per laser photon) pump sources available. To obtain the combined positive effects of narrow-band pump sources as well as efficient pumping, laser diodes are typically used (Hobbs, 2000). Their output is also highly directional, so it can be fed into a fibre-optic cable, which allows for a much wider range of pump schemes. End-pumping of a gain medium is usually achieved by means of a fibre, while side-pumping schemes are implemented without fibre-optics. Laser diodes are therefore a good choice for implementing an efficient high-power system, and are typically used for Continuous Wave (CW) and high Pulse Repetition Frequency (PRF) systems.

Practically one would like to achieve optimal spatial coherence by focussing as much of the pump energy as possible into an area that is about as large as the resonator mode. This spatial overlap between the resonator and pump modes is called mode-matching. Furthermore, the resulting heat load within solid gain media is much less when using narrow-band type pump sources (see Section 2.5). This implies that higher pump powers and thus higher laser energies can be achieved using narrow-band sources, with an overall higher conversion efficiency of source energy into laser energy.

The threshold of a laser quantifies the minimum pump power that must be supplied to the laser for lasing action to occur. For diode-pumped solid-state lasers this threshold P_{th} can be determined by

$$P_{th} = \frac{\pi h \nu_p}{4 \eta_{p-g} \sigma_{em} \tau_{21}} \left(\omega_l^2 + \omega_p^2\right) (T + L), \tag{2.5}$$

with ν_p the pump frequency, η_{p-g} the pump quantum efficiency, σ_{em} the emission cross-section of the laser wavelength, τ_{21} the excited state lifetime (see Figure 2.2), ω_l and ω_p

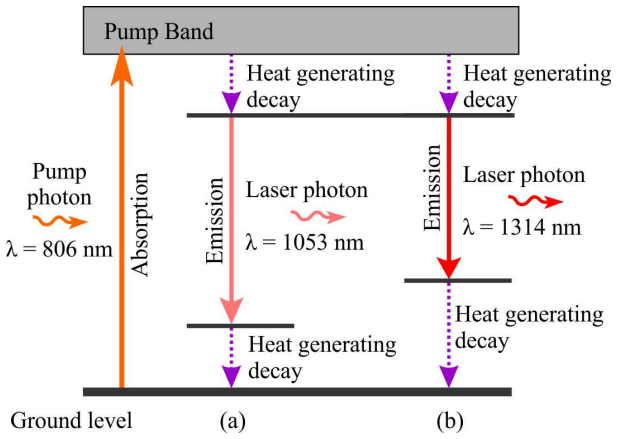

Figure 2.7: Heat generation due to quantum defect of Nd:YLF pumped by 806 nm photons for a) 1053 nm and b) 1314 nm laser operation. The dashed lines depict some possible heat-generating transitions (via multi-phonon relaxations), the solid lines indicate transitions involving photons.

the laser and pump beam radii, T the output coupler transmission and L losses within the resonator (Bollig, 1997).

Figure 2.6 depicts the schematic of a typical diode end-pumped solid-state laser. The optical resonator is made up of a Back Reflector (BR) which will transmit pump wavelengths but reflect laser wavelengths, while the Output Coupler (OC) partially reflects laser wavelengths. The pump and laser (resonator) modes overlap within the gain medium. These type of laser implementations have long lifetimes, high efficiencies and high output powers with very good laser beam quality, all from a compact package (Paschotta, 2015).

2.5 Thermal effects in solid state lasers

2.5.1 Heat generation mechanisms

Heat-generation in the gain medium is the main obstacle in maintaining good beam quality while power-scaling diode end-pumped solid-state lasers (Clarkson, 2001). This is because not all of the pump energy is converted to laser energy but instead is deposited in the gain medium as heat energy via various mechanisms (Hardman et al., 1999; Koechner, 1999). An increase in the thermal load results in a decrease in beam quality (a higher M^2-value) due to thermal lensing (Pollnau et al., 1998b) and ultimately leads to crystal fracture.

The main mechanisms of heat generation within a gain medium are:

- Quantum Defect
- Non-radiative decay and fluorescence
- Absorption of pump light into energy levels other than the desired pump band
- Excited State Absorption
- Energy Transfer Upconversion

The Quantum Defect q_{defect} is the percentage energy difference of a laser photon relative to a pump photon:

$$q_{defect} = \left(1 - \frac{\lambda_{pump}}{\lambda_{laser}}\right) \cdot 100. \tag{2.6}$$

Equation 2.6 effectively describes the minimum amount of pump energy that is converted into heat within the gain medium (Pollnau et al., 1998b). Figure 2.7 depicts a practical example for the the Nd^{3+}-ion within an YLF lattice demonstrating the heat generating mechanisms. For the practical example in Figure 2.7 we have a quantum deficiency $q = 23.5\%$ for lasing at 1053 nm and $q = 38.7\%$ for lasing at 1314 nm. Using pump and laser wavelengths which are further apart thus leads to increased heat generation.

Non-radiative decay and fluorescence occurs when an excited ion does not decay via stimulated emission. The contribution from these effects becomes very small if there is a good overlap between the pump and laser modes and the laser is operated far above the lasing threshold (Pollnau et al., 1998b). In diode end-pumped lasers these effects are near-negligible due to the good spatial overlap between the pump and laser modes that can be achieved within the gain medium.

The absorption of pump light into other levels than the intended pump band occurs especially when employing sources with:

- a narrow band, but with a pump photon energy not matching the desired energy transition within the gain medium ions
- a wide line width or continuum spectral emission

These effects lead to the ground-state gain medium ions being excited to levels other than that of the desired pump band. Such excitations will not contribute to a population inversion (and thus not to stimulated emission) but only lead to heat generation. Using laser diode pump sources optimises absorption into the pump band because they have line widths of a few nanometres and can usually be chosen and controlled to emit close to the desired pump wavelength.

Excited State Absorption (ESA) is the process whereby an excited ion absorbs either a pump or laser photon due to the existence of multiple higher-energy levels. This process for Nd:YLF is illustrated in Figure 2.8, where a pump photon excited it to the $^4F_{3/2}$ state. The higher-energy levels can have an energy difference with some excited state (eg. the $^4F_{3/2}$ state) which is near the energy of pump and / or laser photons. Some ions are then excited into these higher energy states and decay both radiatively and non-radiatively back to either the metastable or ground states. At least one pump or laser photon is therefore lost (depending on which one was absorbed), its energy being transferred to heat in the crystal. The effects of ESA are an increase in heat as well as fluorescence in the crystal during lasing.

Energy Transfer Upconversion (ETU), sometimes referred to only as upconversion, is the process whereby an excited ion relaxes to a lower level by transferring its energy to a nearby ion which was already in the metastable excited state. ETU processes therefore convert two (or more) excited ions into a single higher-energy excited ion. This process is illustrated by

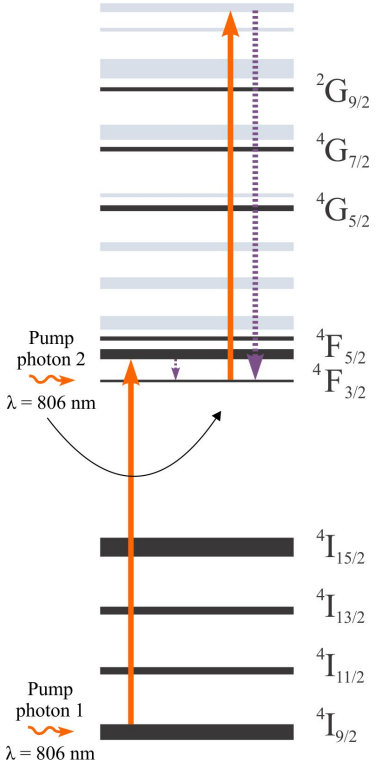

Figure 2.8: Excited State Absorption (ESA) as it can occur within the energy level scheme of Nd:YLF (Pollnau et al., 1998b). The dashed lines depict some possible heat-generating transitions (via multi-phonon relaxations), the solid lines indicate transitions involving photons.

Figure 2.9 for the case of Nd:YLF and was adapted from Pollnau et al. (1998a,b). Both Nd ions are in the excited $^4F_{3/2}$ state due to pump photon absorption. Nd ion 2 can absorb the energy, equivalent to a laser-transition energy, from Nd ion 1, placing it in either the $^4G_{7/2}$ or $^2G_{9/2}$ state. A photon that would have contributed to laser action is therefore lost to a neighbouring excited ion which then converts this energy to heat. The process of ETU reduces the population of the upper laser level, thus shortening the apparent metastable lifetime (τ_{21} in Figure 2.2). It also increases the heat generation within the gain medium. To decrease ETU one can use a lower doping concentration to increase the Nd^{3+} inter-ionic distance (Bollig et al., 2010). Such a longer inter-ionic distance decreases the probability of the energy transfer between two Nd-ions taking place. A lower doping concentration also results in an increase in the absorption length of the pump light and thus necessitates the use of pump sources of sufficiently high beam quality as well as longer gain media to achieve high efficiency.

2.5.2 Cooling of end-pumped crystals

All lasers that are pumped by optical means experience at least some detrimental thermal effects as a result of the various processes described in Section 2.5.1. Excessive heat build-up within the gain medium is the typical result and it is therefore necessary to extract this excess heat from the medium. Gain media are usually cooled by transferring heat from the crystal

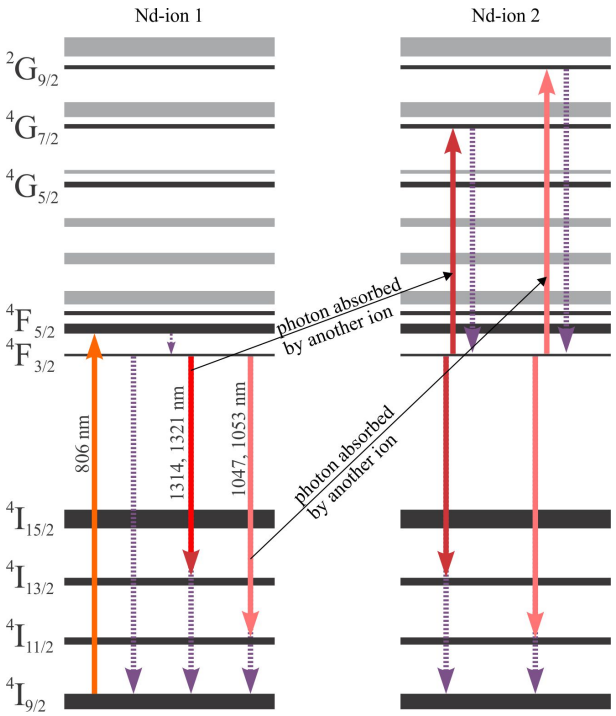

Figure 2.9: Energy transfer upconversion (ETU), as occurring within the energy level scheme of Nd:YLF (Pollnau et al., 1998b,a; Koechner, 1999). The dashed lines depict some possible heat-generating transitions (via multi-phonon relaxations), the solid lines indicate transitions involving photons. Nd-ion 1 (left) depicts a process without upconversion, while neighbouring Nd-ion 2 depicts the upconversion mechanism.

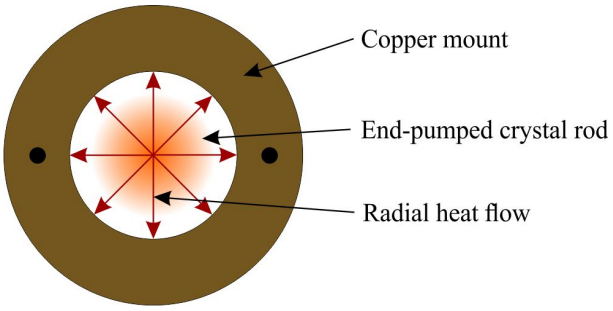

Figure 2.10: Uniform radial heat extraction from a cylindrical crystal rod.

to an externally-cooled heatsink. Side-cooling (cooling of the surfaces that are parallel to the propagation direction z of the laser mode) is the most commonly employed cooling method. Side-cooling is ideally suited for diode end-pumped solid-state lasers, as discussed in Section 2.4. Figure 2.10 illustrates side-cooling of end-pumped gain media. Utilising a round crystal rod has an advantage over other crystal shapes since it results in a near rotation invariant temperature distribution within the gain medium. Since the thermal effects ultimately influence the laser beam shape and quality, this type of temperature distribution should result in fewer detrimental effects than for other crystal shapes and cooling schemes. Figure 2.11 illustrates a modelled radial and longitudinal temperature

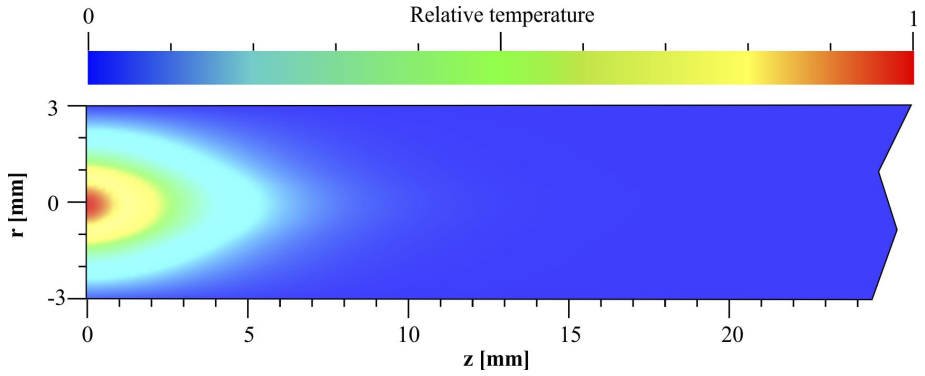

Figure 2.11: The temperature distribution for a cross-section through an Nd:YLF laser rod, which is pumped from the left by a top-hat beam with a radius of 500 µm, as partially simulated in LAS-CAD (LAS-CAD Altmann and Altmann, 2005).

distribution of an end-pumped Nd:YAG laser rod, using the commercial software package LAS-CAD (Altmann and Altmann, 2005). The highest temperature is found where the pump beam enters the gain medium, which also indicates where most of the pump photons are absorbed.

2.5.3 Effects resulting from heat generation

The combination of laser crystal heating (Section 2.5.1) and cooling (Section 2.5.2) leads to a non-uniform temperature distribution within the laser crystal, as can be seen in Figure 2.11. Heat builds up in a gain medium whilst being pumped, creating a temperature gradient which has several effects:

- The refractive index n is temperature dependent. The non-uniform temperature distribution within the laser crystal therefore causes a non-uniform refractive index throughout the volume of the crystal
$$\frac{dn(r,z)}{dT} \neq 0. \tag{2.7}$$
This leads to a lensing effect (of either a positive or negative focal length) along the z-axis. In Nd:YAG this effect is the most dominant contributor to thermal lensing (Clarkson, 2001).

- Differential thermal expansion occurs because of a temperature gradient within the crystal. This effect is even more complex for crystals which have different thermal expansion coefficients for the a- and c-axis. Furthermore, these thermal expansion coefficients may also be temperature dependent (Hardman et al., 1999). The differential thermal expansion of the crystal effectively leads to a bulging of the crystal end-face which is pumped, implying a positive lensing effect along the z-axis. This is denoted by the thermal expansion coefficient
$$\alpha_{th} = \frac{1}{L}\frac{dL}{dT} > 0, \tag{2.8}$$
with L the length of the material.

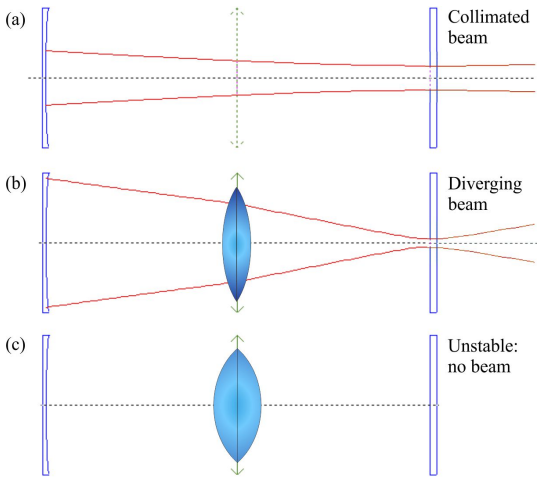

Figure 2.12: An example of the influence of thermal lensing on resonator stability. If all thermal lensing effects can be summarised by a single lens in the centre of a concave-flat resonator, we have for increasing thermal lens strength: a) no thermal lensing, b) an intermediate thermal lens, and c) a strong thermal lens, that makes this resonator unstable. The diagrams were partially simulated in Psst! (Dunn et al., 2014).

- The differential thermal expansion of the crystal leads to internal stresses, which contributes to a change in refractive index (Weber et al., 1999). The resulting gradient of refractive index within the material also causes a lensing effect (of either a positive or negative focal length) along the z-axis

$$\frac{dn(r,z)}{dz} \neq 0, \qquad \frac{dn(r,z)}{dr} \neq 0, \tag{2.9}$$

  with r the radial distance from the z-axis. For Nd:YAG, this effect has the smallest contribution to the overall thermal lens (Weber et al., 1999).

It is therefore clear that thermal effects within laser crystals result in lensing via various mechanisms. Thermal lensing has an impact on the properties and mode of the resonator as well as laser output, an example is depicted in Figure 2.12. One can summarise all thermal lens effects to a single lens in the centre of a concave-flat resonator. While this resonator has stable operation when no thermal lensing effects are present, an increase in the thermal lens strength will eventually lead to the resonator becoming unstable. These effects can, however, be controlled and the impact minimised by using various means. These include the use of round pump beams to end-pump round rods (to keep thermal effects rotation-invariant along the z-axis), lowering the doping concentration within gain media, employing certain suitable pump and laser wavelengths and implementing proper side-cooling of such setups. With birefringent gain media the two polarisations usually have different emission wavelengths as well as different thermal lensing properties, which can be exploited to help minimise detrimental thermal effects (see Section 2.6).

Thermal fracture (see Figure 2.13) is the ultimate limitation on pump power. As the pump power is increased, more heat builds up in the crystal and thermal effects become more pronounced. Especially the differential thermal expansion leads to internal stresses in the crystal material. Excessive differential thermal expansion will eventually lead to crystal

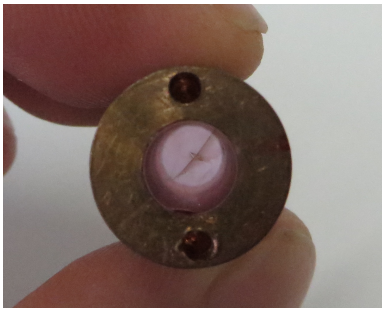

Figure 2.13: A fractured Nd:YLF crystal from one of our experiments. The 6 mm diameter rod fractured about 15 mm from the pump face, near the pump beam focus point.

fracture, where this type of fracture is referred to as thermal fracture. Optical distortions of the laser beam due to thermal effects usually occur before this upper pump power limit is reached. Thermal effects therefore determine the upper limits on the maximum achievable output power from diode end-pumped solid-state laser rods (Cousins, 1992).

2.6 Laser wavelength selection

Solid-state laser gain media generally have numerous possible lasing wavelengths, due to their multitude of available energy levels. These possible emission wavelengths can be depicted and statistically quantified by emission spectrum diagrams, such as the diagrams for Nd:YLF in Section 3.2. The stimulated emission build-up of photons within the resonator starts with all these wavelengths being amplified. The intensity levels of the wavelength with the highest emission cross-section σ_{em} quickly increases to such an extent that it extracts all available energy from the excited ions, leaving little or no excited ions for amplification of other wavelengths. There are several ways, however, to select a laser wavelength which has a lower emission cross section, some of them are utilising specially coated mirrors, thermal lensing effects or wedged crystals for birefringent gain media.

Specially coated mirrors with either broad-band or narrow-band (one or more) reflection or transmission properties are available or can be manufactured for use in laser systems. To diode end-pump a solid state gain medium one typically employs a mirror which is highly transmissive at pump wavelengths (usually $\leq 1\,\mu m$) and highly reflective for laser wavelengths (usually $\geq 1\,\mu m$). By choosing the mirror to have a high reflectance only for a certain wavelength region, one can ensure that only the wavelength with the highest emission cross-section σ_{em} in that chosen wavelength region is amplified by stimulated emission at the laser threshold level.

In birefringent crystals, thermal lensing strengths may be different along the various crystal axes. Specifically the a and c-axis have different refractive indices ($n_o \neq n_e$), different thermal expansion coefficients, and different corresponding emission wavelengths($\lambda_o \neq \lambda_e$). The different wavelengths thus experience different effective thermal lenses and one can force the laser to operate on the wavelength with the better thermal lensing properties. One way to exploit this effect is by designing the resonator in such a way that it will only be stable

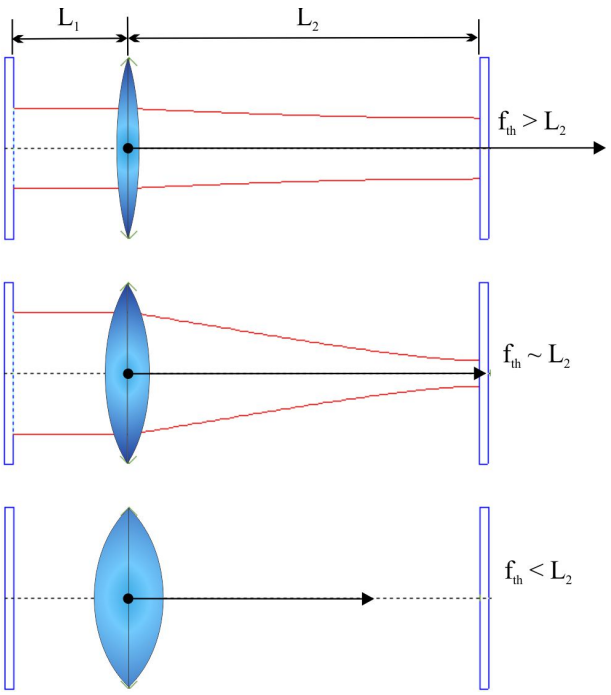

Figure 2.14: An example of the influence of thermal lens strength on resonator stability. This effect can be used in birefringent gain media for wavelength selection. In this example, the flat-flat resonator can be set up to enable lasing only on the wavelength (polarisation) with the weaker thermal lens. The diagrams were partially simulated in Psst! (Dunn et al., 2014).

for the desired wavelength (of one polarisation) but unstable for the other wavelength (on the other polarisation). An example is given in Figure 2.14.

Some other methods of wavelength selection include etalons and gratings. An intra-cavity tilted etalon is a versatile resonator mode selector due to it's simplicity. If an etalon is sufficiently tilted within the resonator, it only acts as a bandpass transmission filter and has no other influence on the resonator. Diffraction gratings can also be employed within laser resonators to aid wavelength selection. Classical plane gratings are good at dispersing different wavelengths. Within a laser resonator a plane grating can thus be used to select the resonating wavelength. Volume Bragg gratings (VBGs) are gratings within transparent media, which will reflect an incident beam if the Bragg condition is met, otherwise the beam passes through the material nearly undisturbed. The Bragg condition can be met when the effective grating spacing (due to the incidence angle) becomes an integer multiple if the incident wavelength.

2.7 Pulsing of lasers using Q-switching

Many different techniques can be employed to generate pulsed laser output from solid-state lasers. Amongst the most commonly used are active pulsing by means of an Acousto-Optic Modulator (AOM) and passive pulsing by means of a saturable absorber, these devices operate by changing the quality factor Q of a resonator. The Q of a resonator is defined as the ratio of energy stored in the cavity to the energy loss per cycle (Koechner, 1999).

A higher Q-value therefore implies lower resonator losses. By modulating the Q-value of a resonator one can control whether lasing action occurs or not. Lasers can be Q-switched by various means such as mechanical mechanisms, electro- and acousto-optical elements as well as passive Q-switching by means of saturable absorbers.

The process of Q-switching occurs as follows (Koechner, 1999; Paschotta, 2015):

- The initial losses of a resonator is kept at a high level (a low Q) so that laser action is prohibited (see Figure 2.15). Pump energy is absorbed by the gain medium and a build-up of energy occurs within it. This energy build-up is only limited by the spontaneous emission of the excited atoms. With continuous pumping one can obtain a population inversion at a level far above the threshold for normal lasing operation.
- The losses are suddenly changed to such a low level (a high Q) that laser action may occur. A very high gain is obtained by the high level of energy stored within the gain medium. The process of stimulated emission along the optical axis of the resonator therefore builds up a large photon flux at an exponential rate.
- The peak photon flux is reached and then rapidly decreases after this.
- Q-switched lasers are usually set up to repeat this process and generate regular pulse trains as a result.

Q-switching can therefore be used to obtain laser pulses by modulating the intra-cavity losses and this technique is mainly used to obtain high-energy nanosecond-level pulses from solid-state lasers. To obtain pulses of picosecond-level durations, one must employ mode-locking together with Q-switching. It operates on the principal that various effects influencing a circulating laser pulse are in balance - the pulse parameters are then unchanged after each round-trip and a regular pulse train is emitted as the pulse hits the output coupler.

A short discussion of AOMs and saturable absorbers follows since these devices were used in the experimental work as described in Chapters 4 and 5.

2.7.1 Active Q-switching with an Acousto-Optic Modulator

Active Q-switches in the form of AOMs are manufactured from a transparent optical material such as fused silica. Such an AOM device is then placed within the resonator so that the optical z-axiz runs through it, in such a way that it does not inhibit lasing action. When an ultrasonic wave is launched through the optical material of the AOM, it acts as an optical phase grating due to the photo-elastic effect which modulates the index of refraction. The AOM can then refract a portion of a beam to diverge from the resonator z-axis, thereby providing an energy loss which lowers the Q-value of the resonator. A sufficient lowering of the resonator Q-value will inhibit lasing action to occur (see Figure 2.15). When the ultrasonic wave is removed, the material returns to the normal unperturbed state which increases the Q-value of the resonator and lasing action can resume. A piezo-electric transducer is typically used to generate the ultrasonic wave. This component is controlled by supplying it with an electric current that varies at Radio Frequencies (RF) in the MHz range. The

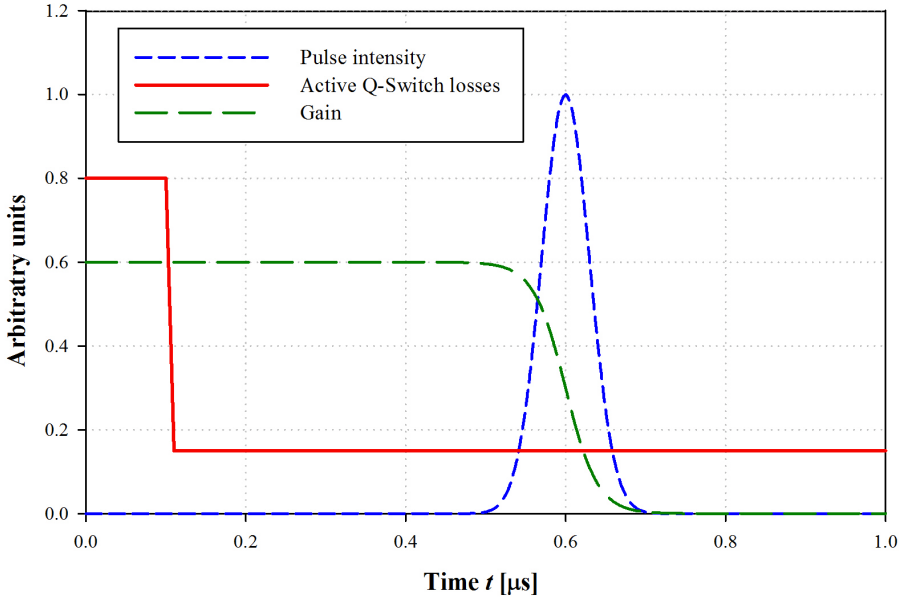

Figure 2.15: Creating a laser pulse by active Q-switching, in terms of the gain and losses.

external control of the resonator Q-value classes an AOM as an active device and lasers using such an optical element are called actively Q-switched.

2.7.2 Passive Q-switching with a saturable absorber

A saturable absorber is an optical material which becomes more transparent as the incident fluence increases. At high incident intensities, the material saturates (or bleaches), which results in the material appearing to be nearly transparent. This process of bleaching occurs due to the saturation of a spectral transition within the saturable absorber (refer to Section 4.2.1 for an example). A saturable absorber has varying absorption rates at various wavelengths and typically an absorber which has a high absorption at the lasing wavelength is used. Placing such a saturable absorber within a resonator will initially inhibit laser oscillation due to the absorption loss it introduces (low resonator Q-value, see Figure 2.16). The pump energy therefore builds up in the gain medium which increases the gain. As soon as this gain exceeds the round-trip losses the intra-cavity photon flux increases exponentially which cause the absorber element to saturate and become more transparent at that wavelength. This increases the resonator Q-value and a laser pulse forms. Since this process happens spontaneously without any external control or influence, pulsed lasers of this type are called passively Q-switched. Using such optical elements allows one to obtain a pulsed laser of a very simple design in a compact setup.

2.8 Summary

This chapter provided an introduction to stimulated emission and how it can lead to laser action on macroscopic level. Various components required to obtain laser actions were

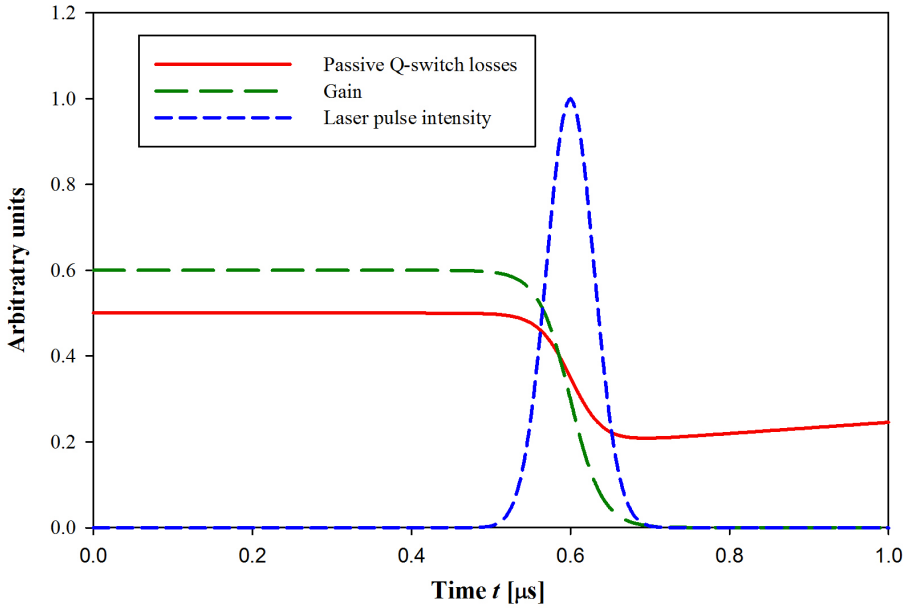

Figure 2.16: Creating a laser pulse by passive Q-switching, in terms of the gain and losses.

discussed and the advantages of diode end-pumped solid-state lasers were highlighted. An overview of heat generation within solid state lasers was given together with the effects resulting from it, as well as methods to mitigate these effects. Q-switching as a method to create pulsed laser output was also discussed.

In the next chapter Nd:YLF as a laser gain medium will be discussed in terms of its various properties, towards the implementation of a diode end-pumped solid-state laser.

Chapter 3

Nd:YLF properties and 1.3 µm operation

Solid-state laser gain media consist of a crystal host material (substrate) which has been doped with an element from the transition metals or lanthanides. The most commonly used host material is Yttrium Aluminium Garnet (YAG) which is isotropic (properties are invariant along all three crystallographic directions). Other host materials include Yttrium Orthovanadate (YVO_4) and Yttrium Lithium Fluoride (YLF) which are uni-axial (the properties for one crystallographic axis is different than for the other two). The process of doping replaces a certain percentage of one of the elements within the host material with a dopant element. Neodymium (Nd) is the most common dopant and others include Holmium (Ho), Thulium (Tm), Yttrium (Y) and Ytterbium (Yb). The combination of a host material and dopant is depicted by [dopant] : [crystal host], thus Neodymium-doped Yttrium Lithium Fluoride is depicted as Nd:YLF. The exact spectroscopic properties of the resulting gain media are determined by the dopant and perturbed by the crystal host (Koechner, 1999). The energy levels and transition rates of a transition metal dopant (such as Nd) are strongly influenced by the crystal field due to the electron energy-level structure of these transition metals. The YLF host material is known for its long upper state lifetime (τ_{21}) and weak thermal lensing. Crystal host materials doped with Nd have strong emission lines in the 1.0 and 1.3 µm region (Koechner, 1999). An Nd-doped YLF substrate (Nd:YLF) combines these properties and is therefore an ideal gain medium if one desires high pulse energies with good beam quality in either the 1.0 or 1.3 µm wavelength regions.

This chapter provides an overview of Nd:YLF which was used in the experimental work described in Chapters 4 and 5. Nd:YLF as an active material is discussed in terms of its material and spectroscopic properties as well as its various thermal lensing mechanisms. Specific focus on 1314 nm operation of Nd:YLF lasers follows.

3.1 Material properties

Table 3.1 compares Nd:YLF with two commonly used laser crystal materials: Nd:YAG and Nd:YVO_4. The material hardness is the lowest for Nd:YLF at 4 - 5 Mohs and the highest for Nd:YAG at 8 - 8.5 Mohs. Similarly, the tensile strength is the lowest for Nd:YLF at 33 MPa and the highest for Nd:YAG at 200 MPa. These low values for Nd:YLF indicate a greater

Material / Property	Nd:YLF	Nd:YAG	Nd:YVO_4
Chemical Formula	Nd:$LiYF_4$	Nd:$Y_3Al_5O_{12}$	Nd:YVO_4
Crystal structure	tetragonal	cubic	tetragonal
Nd atoms [cm^{-3}] (1% at. doping)	1.4×10^{20}	1.36×10^{20}	1.26×10^{20}
Density ρ [$g\,cm^{-3}$]	3.99	4.56	4.22
Hardness [Mohs]	4 - 5	8 - 8.5	5 - 6
Young's modulus E_{YM} [GPa]	75	280	133
Tensile Strength [MPa]	33	200	53
Poisson's ratio $\nu_{poisson}$	0.33	0.25	0.33
Melting Point [K]	1098	2243	2083
Thermal. conductivity k_{th} [$W\,K^{-1}\,m^{-1}$]	5.8 (c) 7.2 (a)	12	9.0 (c) 12.0 (a)
Thermal expansion coeff. α_{th} [K^{-1}]	8×10^{-6} (c) 13×10^{-6} (a)	$\sim 8 \times 10^{-6}$	11×10^{-6} (c) 4.4×10^{-6} (a)
Refractive index n ($\lambda \sim 1.06\,\mu m$)	$n_e = 1.470$ (c) $n_o = 1.448$ (a)	1.82	$n_e = 2.17$ (c) $n_o = 1.96$ (a)
Thermo-optical coefficient dn/dT [K^{-1}]	-4.3×10^{-6} (c) -2.0×10^{-6} (a)	7.3×10^{-6}	1.05×10^{-6} (c) 1.66×10^{-6} (a)
Excited state $^4F_{3/2}$ lifetime τ_{21} [µs]	520	230	100

Table 3.1: Comparison of the material properties of Nd:YLF, Nd:YAG and Nd:YVO_4 (Pollnau et al., 1998b; Koechner, 1999; Ma et al., 2007; Sato and Taira, 2007; Castech, 2015; Paschotta, 2015).

risk of crystal fracture at higher operating powers, and that care must be taken to manage internal stresses within the crystal. The cubic crystal structure of Nd:YAG implies that the material properties are the same along all three crystallographic directions. The tetragonal crystal structure of Nd:YLF and Nd:YVO_4 implies that the properties are the same along two crystallographic directions (the two a-axis) and different along a third direction (c-axis) (also see Table 2.1). Such tetragonal transmissive optical elements are called uni-axial and have unique values for the c-axis properties of thermal conductivity, the thermal expansion coefficient, the refractive index and the thermo-optical coefficient:

$$\kappa_{th(c)} \neq \kappa_{th(a)}, \quad \alpha_{th(c)} \neq \alpha_{th(a)}, \quad n_e \neq n_o \; and \quad \frac{dn_e}{dT} \neq \frac{dn_o}{dT}. \tag{3.1}$$

Nd:YLF has a relatively low thermal conductivity of 5.8 and 7.2 $W\,K^{-1}\,m^{-1}$for the c- and a-axis respectively, so special care must be taken to implement proper cooling mechanisms for such crystals. The thermal expansion coefficient of Nd:YLF along the c-axis is similar to that of Nd:YAG, but nearly double as much at $13 \times 10^{-6}\,K^{-1}$ along it's a-axis. The thermo-optical coefficient of Nd:YAG is positive and much larger than for Nd:YVO_4, where for Nd:YLF it is negative with values -4.3 and $-2.0 \times 10^{-6}\,K^{-1}$ for the c- and a-axis respectively. The excited state lifetime τ_{21} for the $^4F_{3/2}$ multiplet of Nd:YLF is more than double that of Nd:YAG and 5 times more than for Nd:YVO_4. The long excited state lifetime of Nd:YLF is of particular interest since it implies that during Q-switched opertation, higher pulse energies could be achieved due to the longer energy storage time.

Property \ Material	Nd:YLF	Nd:YAG	Nd:YVO_4
Main 1.0 µm emission line(s) [nm]	1047 (π) 1053 (σ)	1064	1064 (π and σ)
Main 1.0 µm emission cross-section σ_{em} [cm^2]	22×10^{-20} (π) 14×10^{-20} (σ)	29×10^{-20}	123×10^{-20} (π) 52×10^{-20} (σ)
Main 1.3 µm emission line(s) [nm]	1314 (σ) 1321 (π)	1339	1343 (π) 1344 (σ)
Main 1.3 µm emission cross-section σ_{em} [cm^2]	2.4×10^{-20} (σ) 2.3×10^{-20} (π)	7×10^{-20}	32×10^{-20} (π) 13×10^{-20} (σ)

Table 3.2: A comparison between Nd:YLF, Nd:YAG and Nd:YVO_4 in terms of spectroscopic properties (Czeranowsky, 2002).

3.2 Spectroscopic properties

Table 3.2 lists a comparison of the main spectroscopic properties of Nd:YLF with those of Nd:YAG and Nd:YVO_4. The main emission lines for Nd:YLF in both the 1.0 µm and 1.3 µm wavelength regions are typically at a slightly lower wavelength than for Nd:YAG and Nd:YVO_4. Nd:YLF also has lower emission cross-sections than Nd:YAG and Nd:YVO_4 for all it's main emission wavelengths. However, the 1.3 µm emission lines of Nd:YLF at 1314 and 1321 nm are of interest due to their various application possibilities. These wavelengths can not be obtained easily with either Nd:YAG or Nd:YVO_4 (see Section 1.2.2).

The absorption spectra of Nd:YLF are depicted in Figure 3.1. The main absorption regions are at 785 - 815 nm and 855 - 885 nm. The strongest absorption lines, in decreasing order of strength, are at ∼792 nm, 798 nm and 863 nm for the π-polarization and at ∼798 nm, 806 nm and 809 nm for the σ-polarization. Pumping at the strongest absorption cross section σ_{abs} of 792 nm requires the pump to be polarised because the π-polarization absorption is an order of magnitude stronger than for the σ-polarization absorption. At 805.5 nm the absorp-

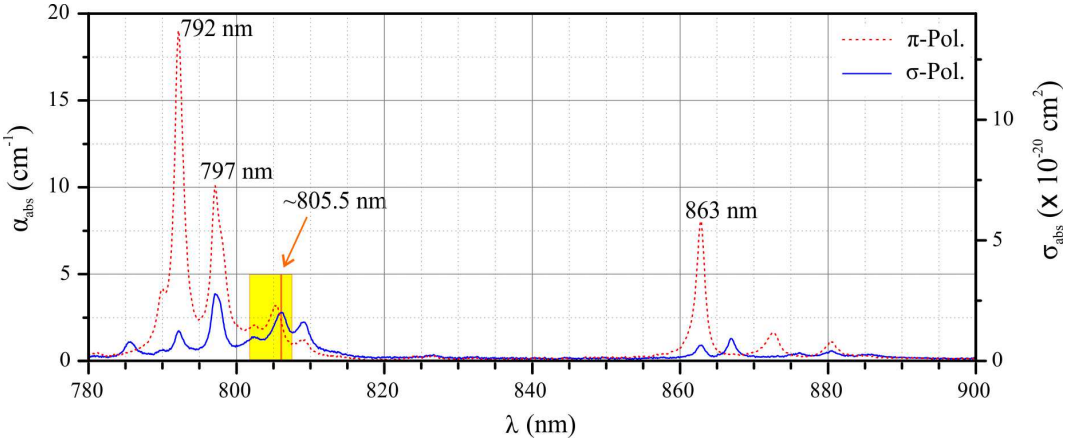

Figure 3.1: The absorption spectra of 1% at. doping Nd:YLF, as adapted from Czeranowsky (2002). The yellow band indicates the emission range of the pump diode modules (as used in the experimental work in Chapters 4 and 5), the orange arrow and line indicates the selected pump wavelength.

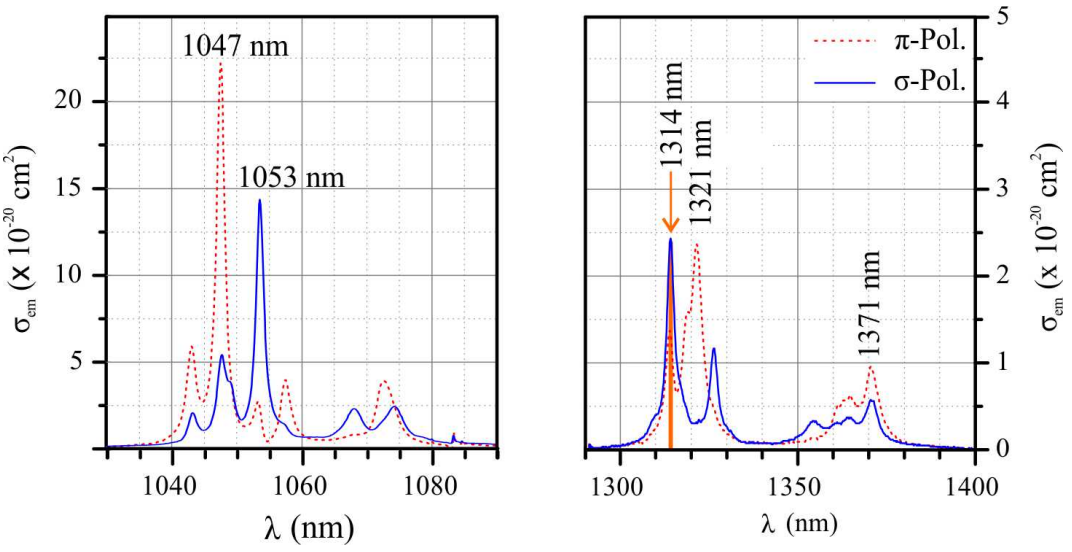

Figure 3.2: Emission spectra of Nd:YLF as adapted from Czeranowsky (2002). The orange arrow and line indicates the resonating wavelength chosen for the experimental work described in Chapters 4 and 5.

tion is the same for both the π- and σ-polarisations and one may then use an unpolarised pump source, such as the fibre-coupled laser diode modules discussed in Section 2.4. The absorption at 805.5 nm is, however, about five times lower than for 792 nm. This results in a longer absorption length along the z-axis of the laser gain medium, causing the heat load being spread longitudinally along the crystal. This heat load distribution reduces internal stresses within the crystal and subsequently lowers the risk of thermal fracture.

The emission spectra for Nd:YLF in the 1.0 and 1.3 µm regions are depicted in Figure 3.2. The strongest emission lines in the 1.0 µm region are at 1047 nm and 1053 nm for the π- and σ-polarizations, with respective emission cross-sections σ_{em} of $22 \times 10^{-20}\,\mathrm{cm}^2$ and $14 \times 10^{-20}\,\mathrm{cm}^2$. The strongest emission lines in the 1.3 µm region are at 1314 nm and 1321 nm for the σ- and π-polarizations, with respective emission cross-sections σ_{em} of $\sim 2.4 \times 10^{-20}\,\mathrm{cm}^2$ and $\sim 2.3 \times 10^{-20}\,\mathrm{cm}^2$, which is about an order of magnitude less than for 1.0 µm operation. Operating a Q-switched Nd:YLF laser at 1.0 µm one can therefore expect a pulse energy of up to an order of magnitude more than for 1.3 µm. In a resonator that has been specially designed to favour 1.3 µm oscillation, lasing can easily occur on both 1314 and 1321 nm simultaneously since the emission cross sections for these wavelengths are very similar. Taking special care with the resonator design to favour a weaker or stronger thermal lens is therefore necessary (see Section 2.6).

A partial energy level diagram for Nd:YLF is depicted in Figure 3.3. It indicates the most relevant pump, laser and heat-inducing transitions via the processes of multi-phonon releasing decay, fluorescent decay, ETU and ESA (see Section 2.5.1). Two metastable levels exist: the normal lasing upper-state level $^4F_{3/2}$ with a lifetime of $\tau_{21} \sim 520\,\mu\mathrm{s}$ and the $^2P_{3/2}$ manifold with a lifetime of $\sim 30\,\mu\mathrm{s}$ (Zuegel and Seka, 1999). All other levels have short ($\tau < 10\,\mathrm{ns}$) lifetimes and decay via multi-phonon (non-radiative) or fluorescent emissive

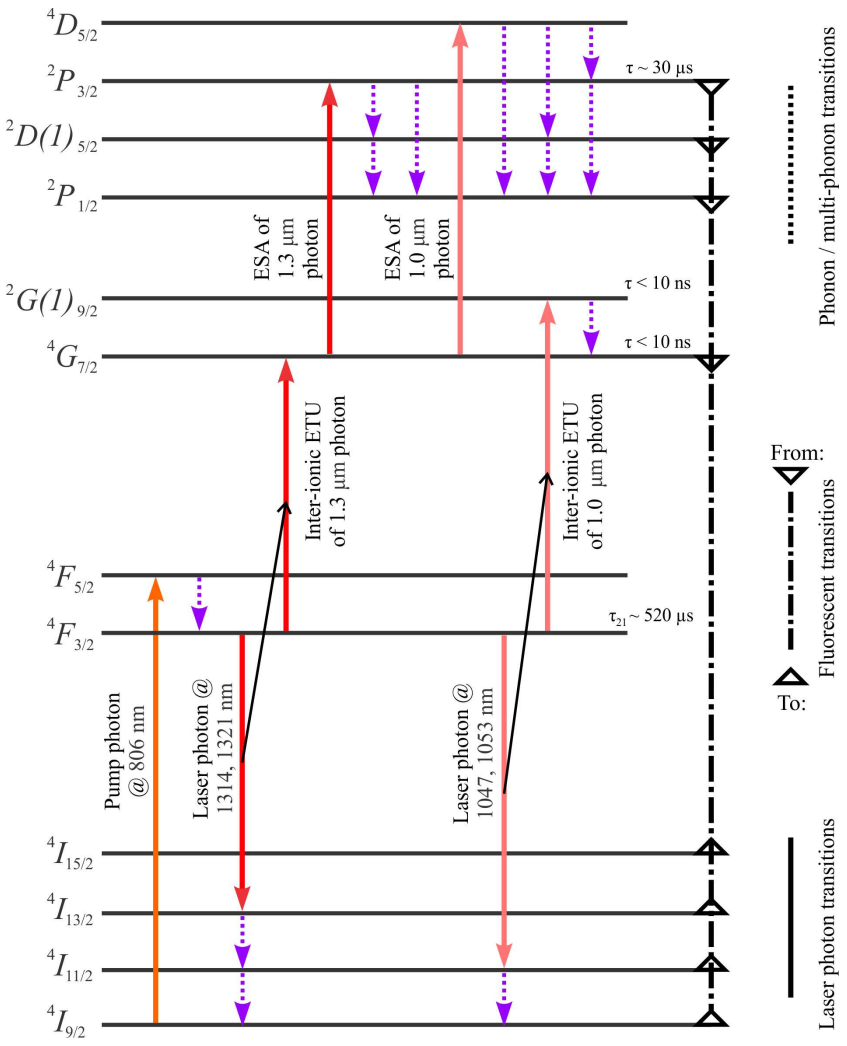

Figure 3.3: A partial energy level diagram of Nd:YLF, depicting processes most relevant to 1.0 and 1.3 µm operation. Adapted from Chuang and Verdun (1996) with additions from Fornasiero et al. (1999) and Zuegel and Seka (1999).

transitions.

The dominant mechanism for populating the $^4G_{7/2}$ multiplet is ETU of 1.0 µm and 1.3 µm photons (Chuang and Verdun, 1996). The processes of ETU in Nd:YLF mostly leads to visible fluorescence due to the decay of the $^4G_{7/2}$ multiplet to lower energy levels. The process of ETU is typically only observed with lasers which are intensely pumped by laser diode modules (Zuegel and Seka, 1999). There is a rapid decline in ETU interaction rates as inter-ionic distances increase and this interaction rate is expected to vary linearly with the doping concentration (Zuegel and Seka, 1999). One can therefore reduce ETU in diode-pumped Nd:YLF by lowering the Nd^{3+} doping concentration.

The process of ESA can usually only occur from the $^4G_{7/2}$ level by the transfer of a 1.0 µm or 1.3 µm photon. During CW operation of Nd:YLF at either 1.0 µm or 1.3 µm the effect of ESA is negligible, especially during moderate pumping conditions (Fornasiero et al., 1999). Furthermore, the ESA is small for pump photons of 803 and 797 nm and negligible

for 792 nm. Only when excitation levels within Nd:YLF become high, ESA becomes relevant and this is typically only observed during Q-switched operation (Fornasiero et al., 1999). During these conditions ESA plays a major role in populating higher level manifolds, thus having a strong influence on pulsed operation (Chuang and Verdun, 1996). The measurement of blue fluorescence by Chuang and Verdun (1996) indicated that ESA of 1.0 µm or 1.3 µm photons from the $^4G_{7/2}$ level may explain the lower than expected efficiency of Q-switched Nd:YLF lasers.

3.3 Thermal lensing

Considering thermal lensing effects within Nd:YLF, one has to consider both heat generating mechanisms, heat flow and the effects resulting from this. As explained in Section 2.5, thermal effects lead to gradients in temperature, refractive index change and internal stresses which all cause laser beam degradation - these effects can lead to thermal fracture at higher pump power levels.

Heat generation mechanisms within Nd:YLF include the quantum defect, ETU and ESA (see Sections 2.5.1 and 3.2). When pumped at 805.5 nm, the quantum defect for Nd:YLF oscillating at 1.0 µm is $\sim$ 23% and for 1.3 µm oscillation it is $\sim$ 39% . The contribution of ETU can be limited by either operating the laser in CW mode, by lowering the pump intensity or decreasing the doping concentration of the active medium (see Section 3.2). The effects of ESA only become relevant if ETU occurs since the ESA originates from an energy manifold that can only be populated by ETU processes. Minimising ETU will therefore automatically inhibit ESA from occuring. A higher level of heat generation due to ETU can, however, be expected for 1.0 µm compared to 1.3 µm operation due to the additional multi-phonon decay from the $^4G(1)_{9/2}$ to the $^4G_{7/2}$ level.

The thermal conductivity coefficient κ_{th} describes the heat flow within the laser gain medium and since Nd:YLF is uni-axial it has values $\kappa_{th(c)} = 5.8\,\mathrm{W\,K^{-1}\,m^{-1}}$ and $\kappa_{th(a)} = 7.2\,\mathrm{W\,K^{-1}\,m^{-1}}$ along the c- and the two a-axis respectively. This results in a non-uniform heat flow within Nd:YLF. For a-cut rods mounted with the c-axis horizontally (as was the case for the experimental setups in Chapters 4 and 5), a larger heat flow will occur in the vertical direction.

The resulting temperature gradients along the c- and the 2 a-axes lead to differential thermal expansions, differential thermo-optical coefficients and differential internal stresses (see Section 2.5.3). The differential thermal expansion coefficients $\alpha_{th(a)} \neq \alpha_{th(c)}$ cause a bulging of the end-face but with different focal lengths along the 2 crystallographic directions of the crystal face. This toric lensing effect distorts a laser beam to be larger along the one axis than the other, making it astigmatic (see Figure 3.4). The index of refraction is temperature dependent and $dn_e/dT \neq dn_o/dT$ for Nd:YLF, which leads to a lensing effect with different focal lengths for different polarisations. Internal stresses resulting from the differential thermal expansion cause gradients in the refractive indices along the c- and a-axis, also resulting in different lensing strengths for e- and o-rays. Since the laser usually resonates only on one polarisation, the resulting laser beam experiences only the lensing effect due to refractive index gradients along its own polarisation axis.

3.4 Diode-end-pumped 1.3 µm Nd:YLF lasers

Power scaling of 1.0 µm Nd:YLF lasers has been investigated by several groups and efficient CW and pulsed operation at sub-100 W powers has been demonstrated (Bollig et al., 2010; Wetter and Deana, 2015). Power scaling of 1.3 µm Nd:YLF is more difficult due to the the larger quantum deficiency as well as the lower emission cross-section σ_{em} in this wavelength region. High-power lasers at 1.3 µm has various fields of application, as discussed in Section 1.2.2. For 1.3 µm Nd:YLF, however, the larger quantum deficiency implies a higher heat load and proper cooling mechanisms should be employed. The long excited $^4F_{3/2}$ state lifetime τ_{21} partially compensates for the low emission cross-section since the laser threshold pump power is inversely proportional to the $\sigma\tau$-product: $P_{threshold} \propto (\sigma_{em}\tau_{21})^{-1}$ (see Equation 2.5 and Bollig (1997)). The efficiency is controlled by the pump beam radius - a smaller pump beam radius leads to higher energy densities and therefore higher efficiencies. However, decreasing the pump beam radius holds the risks of optical damage and thermal fracture and this necessitates a careful resonator and pump beam diameter design (Bollig et al., 2010). Combining a lower threshold with a relatively high slope efficiency will then provide more efficient power scaling of 1.3 µm Nd:YLF.

Nd:YLF has the potential to deliver high pulse energies with a relatively good beam quality. High-power and high-energy 1.3 µm lasers have a wide range of applications (see Section 1.2.2) and can help in obtaining the best beam quality that can be expected from 1.3 µm Nd:YLF lasers (a lower limit to $M^2_{1.3}$) due to thermal effects. Since 1.3 µm operation results in a worse thermal load than for 1.0 µm operation, the achieved $M^2_{1.3}$ will define an upper limit to the $M^2_{1.0}$ for 1.0 µm operation:

$$M^2_{1.0} < M^2_{1.3}. \tag{3.2}$$

Furthermore, one can expect an order of magnitude higher pulse energies from a Q-switched 1.0 µm Nd:YLF laser than for 1.3 µm operation due to the difference in the respective σ_{em}-values. Determining an upper limit of $M^2_{1.0}$ and a lower limit to the 1.0 µm Q-switched pulse energy will help determine the potential for Nd:YLF to be investigated further as a laser source for Lunar Laser Ranging (see Section 1.1). Especially the σ-polarization 1314 nm oscillation is of interest due to the associated weakly negative thermo-optical coefficient dn_o/dT of $-2.0 \times 10^{-6}\,\mathrm{K}^{-1}$, which should partially compensate for the crystal end-face bulging.

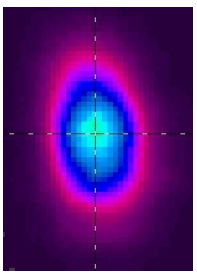

Figure 3.4: The astigmatic intensity profile of an 1314 nm Nd:YLF laser beam as measured during our experimental work.

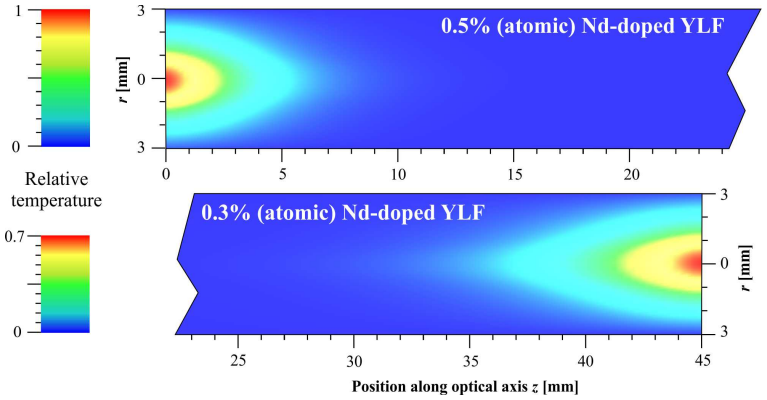

Figure 3.5: The influence of the doping concentration on the temperature inside the Nd:YLF crystals. We partially simulated this image in LAS-CAD (LAS-CAD Altmann and Altmann, 2005).

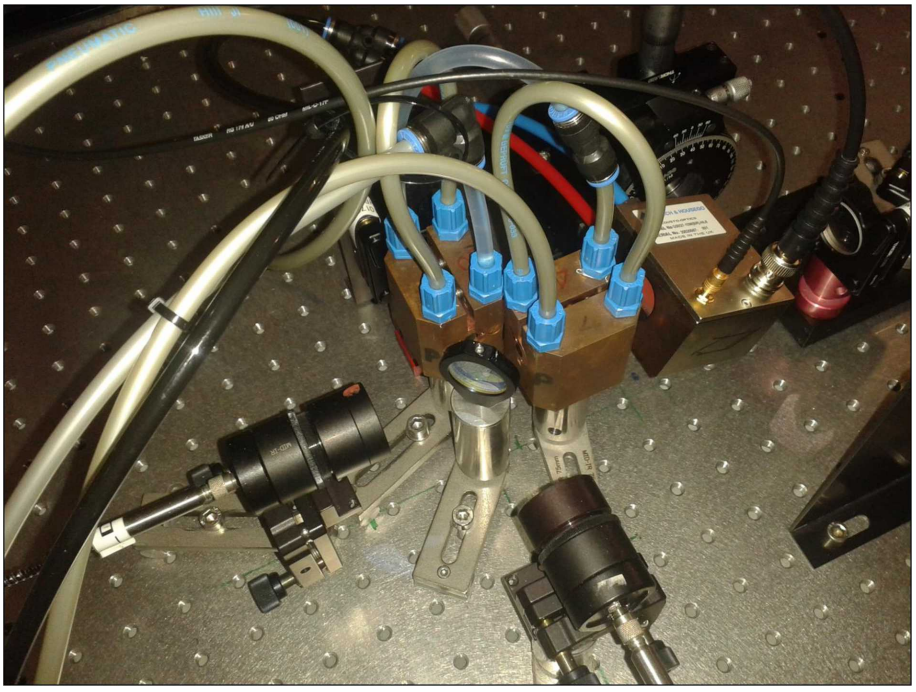

Figure 3.6: A photo of a dual-crystal resonator setup in which the laser crystals are cooled by means of water-cooled copper blocks. The flat resonator folding mirror in this photo allows for the pumping of two crystals through it.

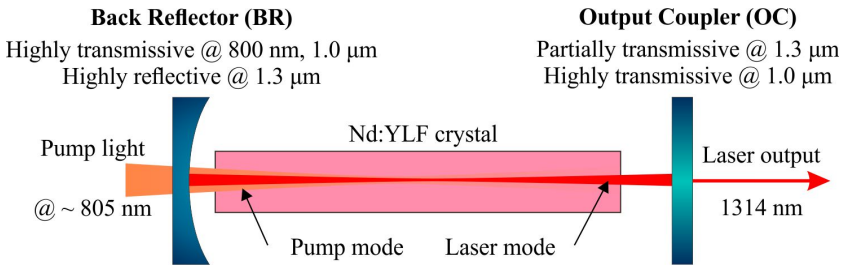

Figure 3.7: A basic schematic of a diode-end-pumped 1.3 µm Nd:YLF laser resonator setup.

Since thermal effects are more pronounced with 1.3 µm operation, one has to a lower doping concentration of the active medium and employ proper cooling mechanisms. Figure 3.5 depicts our simulation for a 75 W pump beam with a diameter of 1.0 mm and a top-hat beam profile at the crystal face, for 2 doping levels of 6 mm diameter Nd:YLF crystals. A lower doping concentration has the dual effects of spreading out the heat load longitudinally along the pump-beam (z-axis) as well as lowering thermal effects due to ETU and ESA (see Section 3.3). A lower doping concentration will, however, lead to lower efficiencies and longer pulse durations during Q-switched operation (thus implying a lower peak power and pulse energy) (Esser, 2005). Figure 3.6 is a photo of a resonator setup with laser crystals which are cooled by means of water-cooled copper blocks, to help alleviate the thermal effects, especially during 1.3 µm operation.

A basic 1.3 µm Nd:YLF resonator setup is depicted in Figure 3.7 and forms the basis of the experimental work described in this thesis. Laser diode modules are used in an end-pumped configuration (see Section 2.4) to excite the active medium with ~805 nm light (see Section 3.2). Operation will be forced on the 1.3 µm emission lines (which has a lower cross-section than the 1.0 µm lines) by employing resonator optics which are highly transmissive at 1.0 µm and highly reflective at 1.3 µm (see Section 2.6). Furthermore, the σ-polarization 1314 nm wavelength can be selected by designing the resonator to only be stable for the weaker thermal lens associated with the a-axis.

3.5 Summary

As a laser host material Nd:YLF has the potential to deliver high pulse energies due to the long excited state ${}^4F_{3/2}$ lifetime τ_{21} ~520 µs compared to τ_{21} ~230 µs for Nd:YAG and τ_{21} ~100 µs for Nd:YVO_4. The emission cross-sections (σ_{em}) for Nd:YLF on the σ-polarization is $\sim 14.0 \times 10^{-20} cm^2$ at 1.0 µm and $\sim 2.3 \times 10^{-20} cm^2$ at 1.3 µm. Compared to the σ_{em} values for Nd:YAG, it is about half of the strongest 1.0 µm value and a factor of 3 less than that of Nd:YAG at 1.3 µm (Czeranowsky, 2002). Due to the lower σ_{em} for Nd:YLF, power scaling such lasers is more difficult than for Nd:YAG, especially for 1.3 µm operation. Operating an end-pumped Nd:YLF laser on the σ-polarization is attractive because of the weak netto thermal lens it exhibits, resulting in good beam quality over a wide range of output power. The $\sigma_{em}\tau_{21}$ product for 1314 nm Nd:YLF enables a reasonably low threshold, while the efficiency is controlled by the pump beam radius.

By using a relatively low Nd doping concentration within the YLF base crystal, one can

reduce upconversion and spread out the thermal load longitudinally in the crystal, which increases the thermal fracture pump limit (Clarkson et al., 1998; Bollig et al., 2010). A lower doping also reduces the thermal effects due to ETU and ESA. Furthermore, Nd:YLF crystals grown by the Czochralski method have a longitudinal gradient in doping, resulting from the physical crystal growth process. Pumping from the lower-doping side of the crystal further lowers the risk of thermal fracture Bollig et al. (2008).

Forcing Nd:YLF to resonate on the σ-polarization wavelength of 1314 nm will allow us to quantify the best beam achievable (a lower limit to $M^2_{1.3}$) for 1.3 µm operation. Since 1.3 µm operation results in a worse thermal load than for 1.0 µm operation, the achieved $M^2_{1.3}$ will define an upper limit to the $M^2_{1.0}$ for 1.0 µm operation. Furthermore, an order of magnitude higher pulse energy can be expected from a Q-switched 1.0 µm Nd:YLF laser than for 1.3 µm operation due to the difference in the respective σ_{em}-values.

The beam quality and pulse energies will give a good indication of the potential use of Nd:YLF in next-generation laser rangers (see Section 1.1). High-power 1.3 µm lasers also have a wide range of applications in remote sensing and ultra-high resolution spectroscopy.

Chapter 4

Passively pulsed Nd:YLF laser at 1314 nm

The initial investigation into the high-power CW and high-energy Q-switched operation of Nd:YLF at 1314 nm is discussed in this chapter. This work was done at Stellenbosch University. In the light of laser ranging as well as other applications mentioned in Chapter 1, the potential high pulse energy that can be delivered by Nd:YLF is of interest. We used a Nd:YLF crystal with a relatively low doping and passively Q-switched it by inserting a Vanadium Yttrium Aluminium Garnet (V:YAG) crystal within the resonator. The use of a saturable absorber for Q-switching allows one to develop a high-energy pulsed laser in a compact package of relatively low cost, compared to actively Q-switched systems. Lower-cost pulsed 1.3 µm laser sources have various uses, some mentioned in Section 1.2.2.

In this chapter we demonstrate high-power 1314 nm operation of a diode end-pumped Nd:YLF laser in CW mode as well as in passively Q-switched mode using a V:YAG crystal.

4.1 Resonator for CW operation

The continuous wave 1.3 µm operation of Nd:YLF was investigated by operating the oscillator on the 1314 nm σ-polarisation emission line. Operation in the 1.3 µm band is more difficult than for the 1.0 µm band because of the lower emission cross-section σ_{em} and the higher quantum defect which leads to increased heat generation (see Section 2.5.1). Pumping was done with a laser diode module (few nm linewidth) using the side-band absorption line around 805 nm. Figures 3.1 and 3.2 depict the selected absorption and emisssion lines.

The laser crystal consisted of a single a-cut Nd:YLF rod of 0.5% atomic doping (average). It was 30 mm long and 5 mm in diameter. This rod was mounted with it's c-axis horizontally, inside a water-cooled copper block. The pump light source was a fibre-coupled Jenoptic (JOLD-140-CAXF) laser diode module capable of delivering up to 140 W of unpolarised CW radiation at ∼805 nm into a 600 µm core diameter fibre with a 0.22 Numerical Aperture (NA) and a beam quality factor of $M^2 \sim 230$. The output power was limited to ∼45 W to help avoid thermal fracture. The laser diode module was water-cooled to 17°C.

The pump beam waist radius of 0.7 mm was determined by us using a gain optimisation

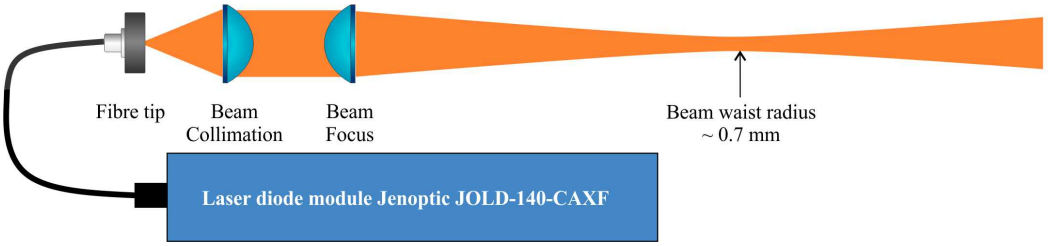

Figure 4.1: The pump setup used to focus the pump beam to the desired beam waist radius of 0.7 mm.

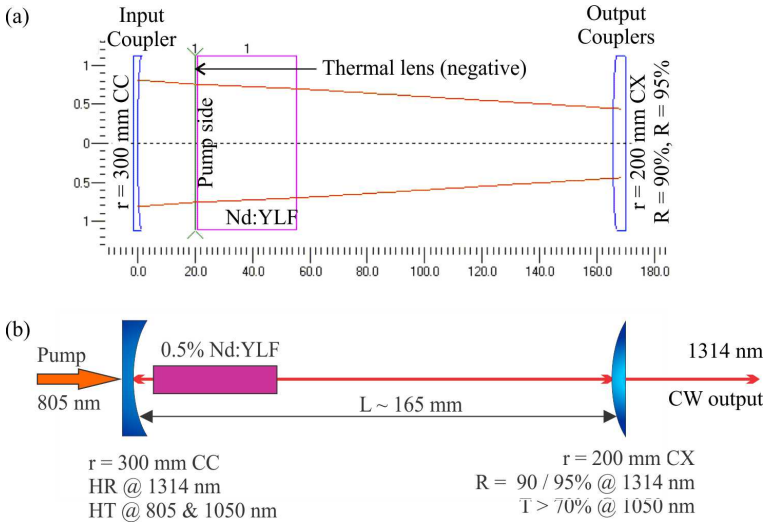

Figure 4.2: (a) The resonator design using a weakly negative netto thermal lens. The resonator mode was determined by a simulation in PSST! (Dunn et al., 2014). (b) The resulting experimental resonator layout for 1314 nm CW operation.

method (which assumes a good overlap between the pump and laser modes (Bollig et al., 2010)). A higher pump energy density was used in our setup to achieve proper levels of gain, due to the lower emission cross section for 1.3 µm compared to 1.0 µm (see Section 3.2). The smallest usable diameter was limited, however, due to the optical damage threshold of the mirrors. The pump light was focussed from the fibre tip by a set of lenses to first collimate and then focus it to the desired beam waist radius (see Figure 4.1). The pump beam had a Rayleigh length of 12.2 mm within the crystal.

The CW resonator (Figure 4.2) was formed by using an $r = 300$ mm concave (CC) input coupler (IC) and an $r = 200$ mm convex (CX) output coupler (OC). Since the thermo-optical coefficient for the 1314 nm σ-polarisation has been reported to be weakly negative (see Section 3.1) and less dominant than for the 1321 nm π-polarisation, this resonator will rather favour oscillations on 1314 nm, even though the polarisations have nearly the same emission cross-section (see Sections 2.6 and 3.2). This is due to the resonator being unstable for the stronger negative thermal lens associated with the π-polarisation of Nd:YLF. The two OCs used had reflections of $R = 90\%$ and $R = 95\%$, respectively. The convex-concave resonator

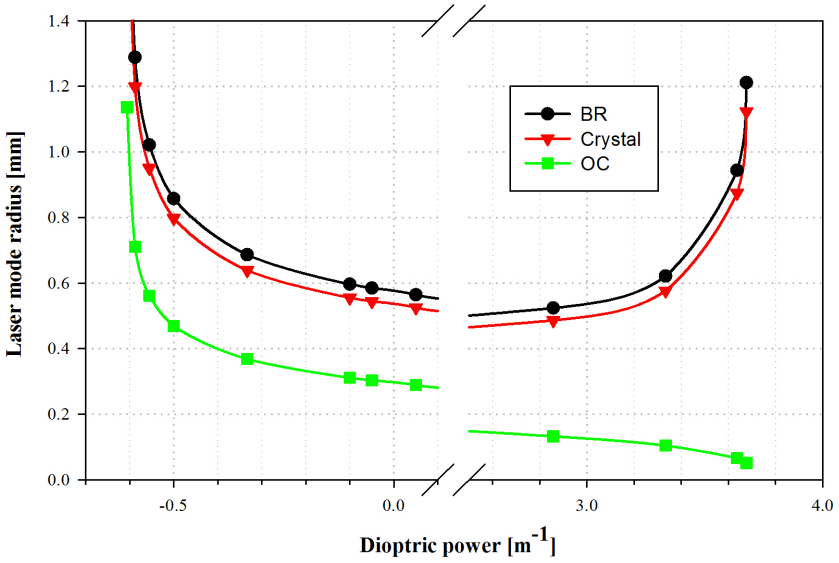

Figure 4.3: Modelled laser mode size radius at various points within the laser resonator (as depicted in Figure 4.2) for a range of dioptric powers of the thermal lens. The simulations were done in the Psst! Laser Resonators package (Dunn et al., 2014).

type was chosen since it allowed a wide range of of laser mode sizes by adjusting the position of the OC. The IC and OC were chosen to be highly reflective (HR) in the 1.3 µm region and highly transmissive (HT) in the 1.0 µm region, to ensure lasing of only 1.3 µm rather than the stronger 1.0 µm emission lines. The OC position then provided a means to choose oscillation of only the 1314 nm σ-polarisation which had the weaker thermal lens. All mirrors used in the resonator were 25 mm in diameter and HT for the pump wavelength region of 805 nm. The Nd:YLF crystal was placed within the resonator, close to the IC. The pump beam was focussed through the IC near the centre of the Nd:YLF crystal. Figure 4.3 depicts the modelled laser mode size at various positions within the resonator for various thermal lens dioptric powers.

The diagnostic setup that was used to characterise the CW (Section 4.1) and the subsequent Q-switched (Section 4.2) laser operation is depicted diagrammatically in Figure 4.4. Mirror 1 reflected 98% of the 1314 nm laser emission to a Coherent LM-10 power meter head. Mirror 2 was used to separate the remaining pump light and laser light. The resulting laser beam was divided by Mirror 3: part of it was focussed into a fibre, the rest was focussed into a beam scanner that was used to determine the M^2. The fibre was connected to either a photo-detector (Thorlabs PDA255) to measure the pulse shape (by connecting it to an oscilloscope during Q-switched operation) or to a spectrometer for wavelength detection.

4.1.1 Results and discussion

The measured CW slope efficiencies are shown in Figure 4.5. The highest CW output power as well as the most efficient operation was achieved with the $R = 95\%$ OC with a resulting optical-to-optical slope efficiency of 29%. The laser had an incident pump power threshold of $P_{pump} = 9.25\,\mathrm{W}$ and a maximum power output of $P_{out} = 10.4\,\mathrm{W}$. This was 70% higher

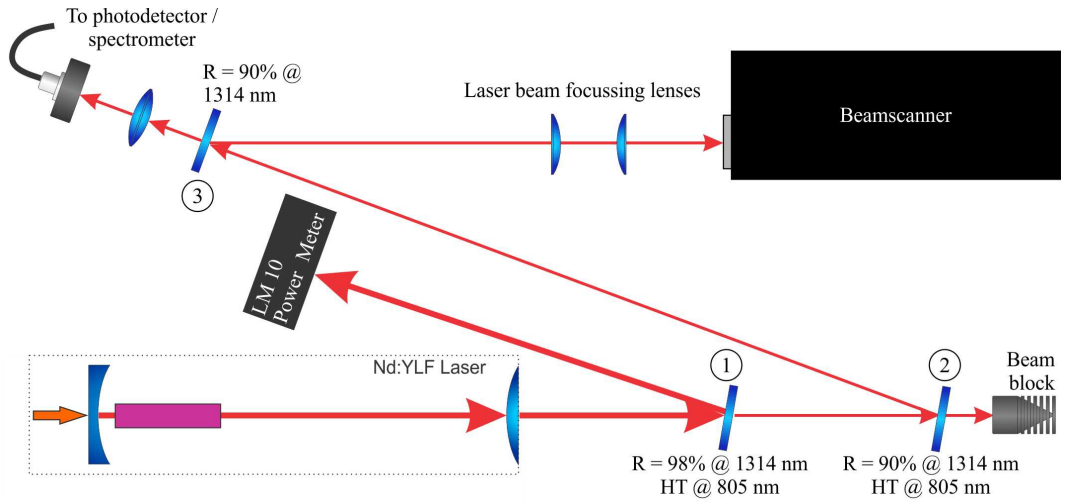

Figure 4.4: Diagramme of the diagnostics setup used for characterising the CW and Q-switched lasers of Sections 4.1 and 4.2.

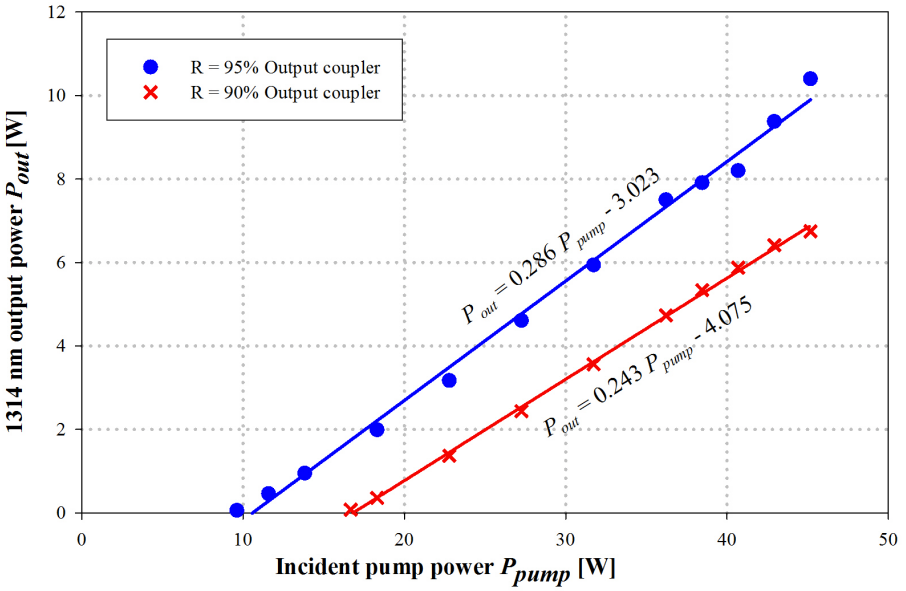

Figure 4.5: Optical-to-optical slope efficiency of the CW laser output.

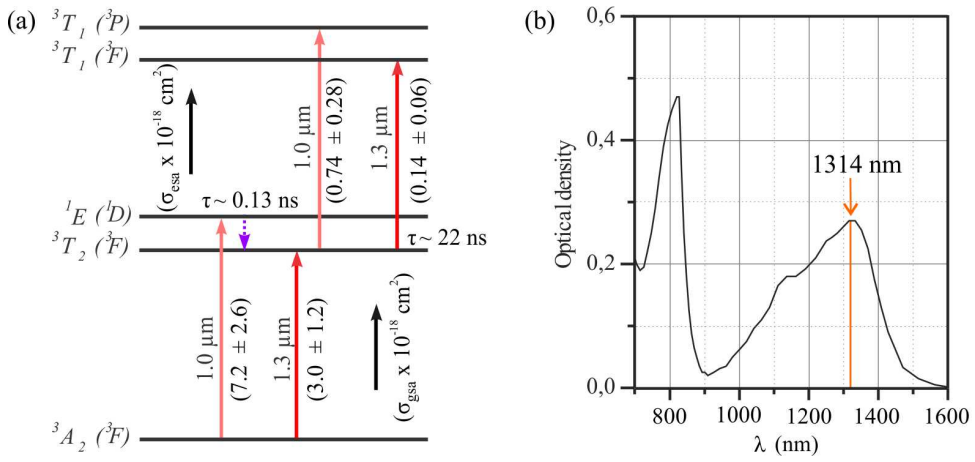

Figure 4.6: (a) The energy levels of V^{3+}associated with saturable absorption in the infrared band (adapted from Malyarevich et al. (1998)). (b) The absorption spectrum of a V^{3+}:YAG crystal (as measured by Podlipensky et al. (2003)).

than the best value (6.2 W) reported in the literature at that stage (Wei et al., 2012). A camera that could operate at 1.3 µm was not available at that stage, so visual inspection of the beam was done with an IR beam viewer. It showed that the beam had a symmetrical Gaussian profile at lower pump power while it became slightly elliptical with the horizontal radius ~25% larger than the vertical at higher pump power. This was due to the astigmatic thermal lensing of Nd:YLF (see Section 3.3). Wavelength measurement indicated that the laser only oscillated on the 1314 nm σ-polarisation emission line, due to the resonator being unstable for the stronger negative thermal lens associated with the π-polarisation of Nd:YLF.

4.2 Passively pulsed operation with V:YAG saturable absorber

4.2.1 Properties of V:YAG as a saturable absorber

The Cr^{4+}:YAG saturable absorber has traditionally been used as a passive Q-switch. However, the absorption of Cr:YAG is *only* in the near-IR band of 800 - 1200 nm, which makes it unsuitable for use in 1.3 µm lasers. It has been demonstrated that V^{3+}:YAG can be effectively used for mode-locking and Q-switching of solid-state lasers at 0.7 µm, 1.06 µm, 1.34 µm and 1.44 µm (Mikhailov et al., 1993; Malyarevich et al., 1998). Figure 4.6 depicts the V^{3+} energy levels associated with saturable absorption and the resulting absorption spectrum (Podlipensky et al., 2003). The different absorption peaks are attributed to V^{3+}-ions that can occupy both tetrahedrally and octahedrally co-ordinated positions in a YAG crystal. It is the tetrahedrally co-ordinated V^{3+}-ions which contribute to the absorption peak at ~1320 nm due to the $^3A_2 \rightarrow ^3 T_2 \left(^3F\right)$ transition. Malyarevich et al. (1998) calculated that their sample had ground- and excited-state absorption cross-sections of $\sigma_{gsa} = (7.2 \pm 2.6) \times 10^{-18}\,\mathrm{cm}^2$ and $\sigma_{esa} = (0.74 \pm 0.28) \times 10^{-18}\,\mathrm{cm}^2$ at 1.3 µm. V:YAG should therefore be suitable as a saturable absorber in 1314 nm Nd:YLF lasers since it has a high ratio $\alpha = \sigma_{gsa}/\sigma_{em}$ (Jabczynski et al., 2001), with $\sigma_{em} \sim 2.4 \times 10^{-20}\,\mathrm{cm}^2$ for 1314 nm

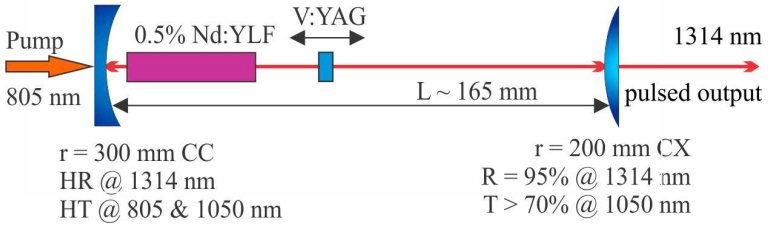

Figure 4.7: Experimental resonator layout for 1314 nm passively Q-switched operation using a V:YAG saturable absorber.

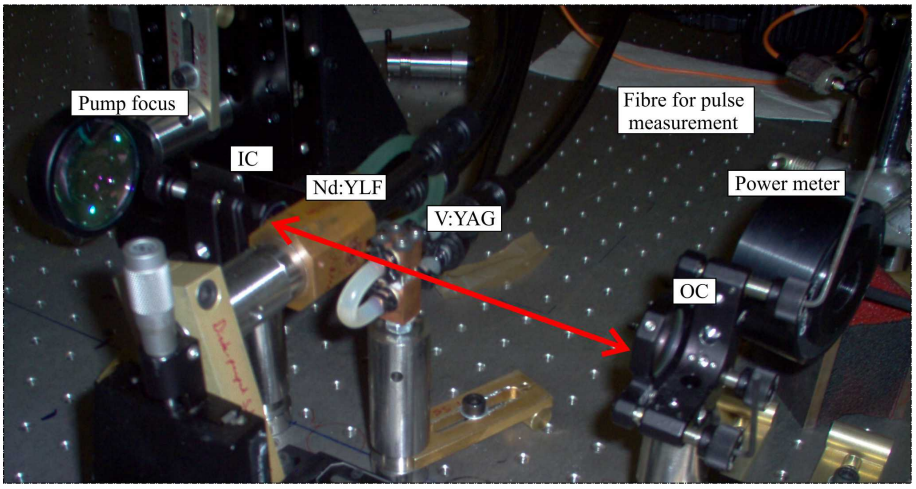

Figure 4.8: A photo of the passively Q-switched resonator.

Nd:YLF (Section 3.2).

4.2.2 Experimental setup

The CW resonator of Section 4.1 was adapted for passive Q-switching by inserting a V:YAG saturable absorber into the cavity between the Nd:YLF crystal and the $R = 95\%$ OC (see Figure 4.7). The V:YAG was 3 mm thick and had an initial single pass absorption of ~3%. Initial experiments indicated that the pulsed performance at various incident pump powers was relatively insensitive to the position of the V:YAG passive absorber and it was subsequently placed ~12 mm from the Nd:YLF crystal. The position of the OC was slightly adjusted to mode-match the pump and the laser mode within the gain medium. A photo of the resonator is shown in Figure 4.8.

4.2.3 Results and discussion

The incident pump power (P_{pump}) threshold was 17.5 W. A maximum average output power (P_{avg}) of 5.2 W was obtained from 45.2 W of incident pump power (Figure 4.9). The pulsed 1314 nm beam had beam quality factors of $M_x^2 = 1.70$ and $M_y^2 = 1.99$, respectively (Figure 4.10). As the incident pump power was increased from threshold to 27 W the pulse repetition frequency PRF increased from 650 Hz to 5.9 kHz. The PRF stayed near-constant at 6.3 kHz

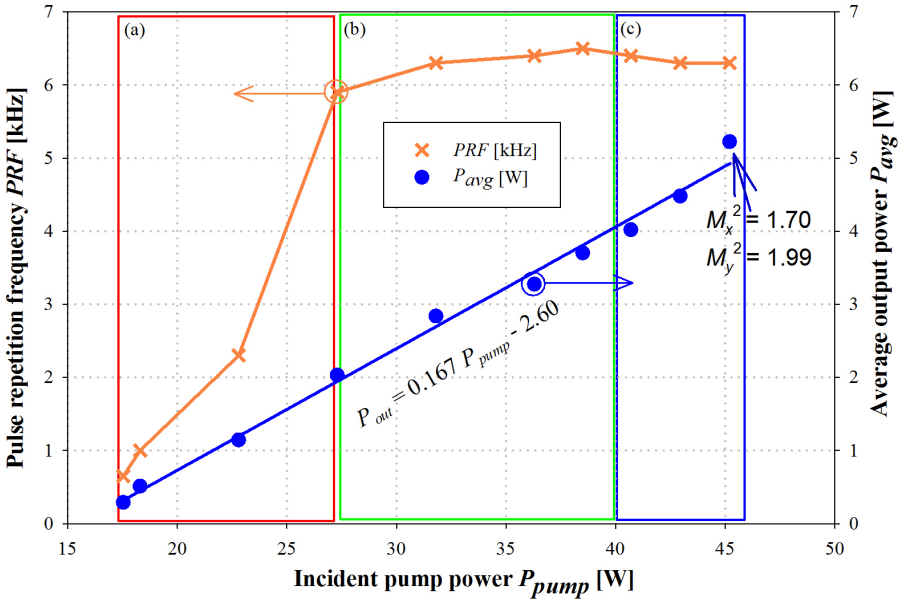

Figure 4.9: Passively Q-switched behaviour: pulse repetition frequency PRF (left axis) and the 1314 nm average output power P_{avg} (right axis). The red (a), green (b) and blue (c) zones are indicative of areas of typical behaviour and are discussed in the text.

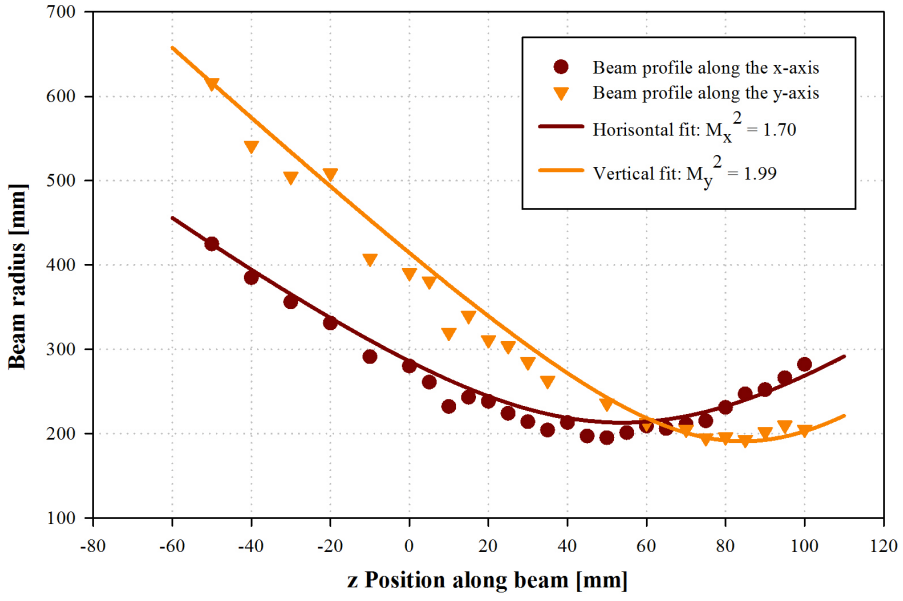

Figure 4.10: The measured horizontal and vertical beam radii, along the beam and through the focus. These were used to determine the M^2 fits.

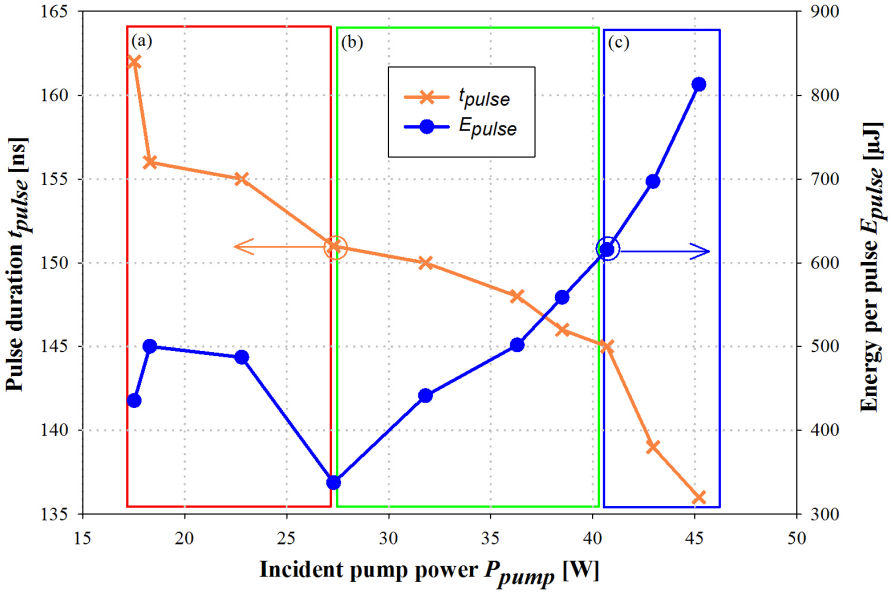

Figure 4.11: Passively Q-switched behaviour: pulse duration t_{pulse} (left axis) and the energy per pulse E_{pulse} (right axis). The red (a), green (b) and blue (c) zones are indicative of areas of typical behaviour and are discussed in the text.

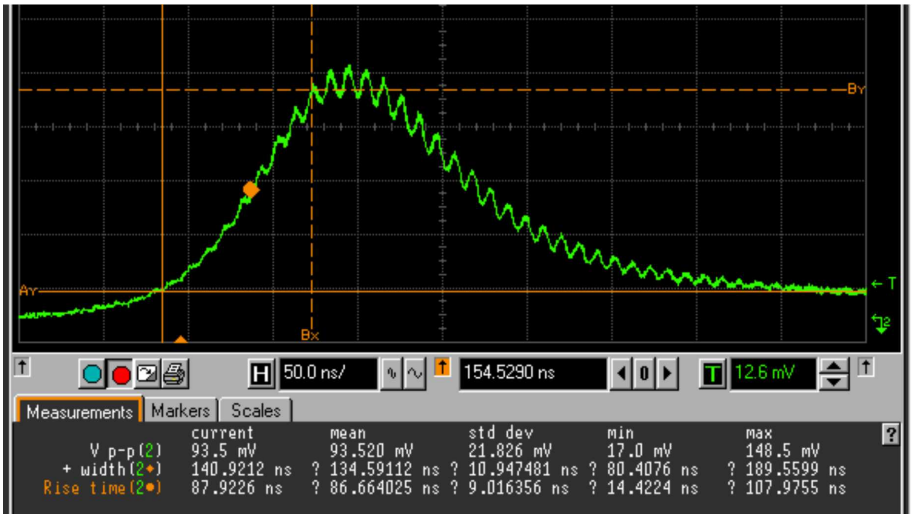

Figure 4.12: A temporal pulse profile as measured for the passively Q-switched laser.

with a further increase in incident pump power. The constant PRF over a wide range of powers may be a desirable characteristic for many applications. This non-standard behaviour is discussed in the next paragraph after all the results have been presented.

The pulse duration at full width at half maximum (FWHM) decreased from 162 ns to 136 ns with an increasing pump power P_{pump} (Figure 4.11). The temporal pulse profile displayed strong spiking behaviour on the pulse shape due to longitudinal mode competition (Figure 4.12). The increase in average output power and an almost constant PRF for $P_{pump} > 27$ W resulted in an increase of pulse energy E_{pulse} up to 825 µJ, which corresponded

to a peak power of 6.1 kW. The average power P_{avg} and energy per pulse was higher than reported for any diode end-pumped 1.3 µm Nd laser which was passively Q-switched with V:YAG at that stage: 2.1 W average power with Nd:YVO_4 (Jabczynski et al., 2001) and 126 µJ pulse energy with Nd:YAG (Sulc, 2004).

The behaviour of the system as observed in Figures 4.9 and 4.11 can be explained by 2 different mechanisms occurring simultaneously, as the pump power is increased:

1. The combined thermal lensing effect from the Nd:YLF and V:YAG crystals: modelling shows that the combined thermal lensing increases the laser mode size as the pump power is increased, with an exponential increase in mode size at high pump powers.

2. Pump light absorbed by the V:YAG crystal: At low pump powers, all the pump light is absorbed by the Nd:YLF crystal. As the pump power is increased, pump liight starts leaking out of the Nd:YLF crystal. It can then be absorbed by the V:YAG crystal since it has a strong absorption at the pump wavelength of 806 nm (see Figure 4.6). The increased absorption by the V:YAG crystal leads to a faster bleaching of the crystal. As the pump power is increased, this effect becomes more pronounced.

The combination of these two mechanisms leads to the behaviour as observed in the three (red, green, blue) zones as indicated in Figures 4.9 and 4.11:

Red: Thermal lensing is low but increasing, leading to a rise in the PRF, E_{pulse} and a decrease in t_{pulse}. Initially the Nd:YLF absorbs all pump power, but as P_{pump} is increased, the pump light starts to reach the V:YAG crystal, bleaching occurs faster and this limits the pulse energy build-up time. This can be seen by the sudden decrease in E_{pulse} in the last part of this zone.

Green: There is a gradual increase in thermal lensing, which slowly increases the laser mode size. Bleaching of the V:YAG due to 1314 nm photon absorption therefore occurs at a lower rate. This is counteracted by a linear increase of pump light incident on the V:YAG crystal. This gives rise to near linear behaviour for the laser characteristics in this zone, as depicted in the green zones of both Figures.

Blue: Thermal lensing becomes so strong that the laser mode starts to increase exponentially with increasing pump power. This leads to much slower bleaching of the V:YAG due to the low flux density of 1314 nm photons. The pump light incident on the V:YAG still increases linearly, which leads to a linear increase in the bleaching due to pump photons. The combination of these lead to a netto decrease in the bleaching rate as pump power is increased, especially since the absorption of 1314 nm is higher than for 806 nm (Figure 4.6).

4.3 Summary

High average power 1314 nm oscillation of a Nd:YLF laser was demonstrated for CW operation and delivered up to 10.4 W of output power (Botha et al., 2013). Passively Q-switched operation of a Nd:YLF laser using a V:YAG saturable absorber was demonstrated for the

first time. Pulsed operation delivered 825 µJ of energy per pulse with a pulse duration of 135 ns and an average power of 5.2 W. The pulsed beam had a slight elliptical shape due to astigmatism and had beam quality factors of $M_x^2 = 1.70$ and $M_y^2 = 1.99$ respectively.

The high CW output power as well as high energy per pulse combined with a good beam quality indicates that Nd:YLF is a good candidate for further scaling in terms of CW power as well as pulse energies. Especially the power and energy scaling of 1314 nm Nd:YLF lasers is of interest because of the applications mentioned in Section 1.2.2. In Chapter 5 we continue the investigation into further power and energy scaling of Nd:YLF lasers at 1314 nm.

Chapter 5

Actively Q-switched dual crystal Nd:YLF laser at 1314 nm

In Chapter 4 up to 10.4 W of CW power and up to 825 µJ energy per pulse from a passively Q-switched Nd:YLF laser at 1314 nm was demonstrated. These results are promising, especially for the high pulse energies required for LLR and some other applications mentioned in Chapter 1. The following experiments were done to investigate power scaling of 1314 nm Nd:YLF lasers to even higher powers and pulse energies than reported in Chapter 4. Especially the potential high pulse energies are of interest. Power scaling was achieved by using crystals with a lower average doping, pumping from the lower-doping side and implementing a dual-crystal setup. We also wanted to demonstrate actively pulsed operation of such a laser since high pulse energies are expected for a 1314 nm Nd:YLF laser when actively Q-switched with an AOM.

In this chapter we demonstrate high-power 1314 nm operation of a diode end-pumped dual-crystal Nd:YLF laser in both CW and actively Q-switched modes.This work was done at the CSIR National Laser Centre.

5.1 Active media

VLOC is a company that, amongst other capabilities, specialises in the growth of laser materials. Through a collaboration between VLOC and the CSIR National Laser Centre, we obtained several Nd:YLF crystals. The crystals were all cut from the same, specially manufactured low-doping boule that was grown with the Czochralski-method. Laser crystals grown by this method have a longitudinal gradient in the doping resulting from the physical growth process. VLOC estimated the doping concentration throughout the boule and maintained the crystal orientation information during the cutting process. The two crystals used in our experiment were a-cut rods which were 45 mm in length and had a 6 mm diameter (Figure 5.1). The atomic doping concentration gradient of Nd^{3+}-ions within these crystals varied linearly from 0.30% to 0.52%. The lower average Nd^{3+} doping (than for the setup in Chapter 4) of 0.41% implied an increased inter-ionic distance between the Nd^{3+}-ions within the YLF crystal substrate. This reduces the ETU (see Section 2.5) which

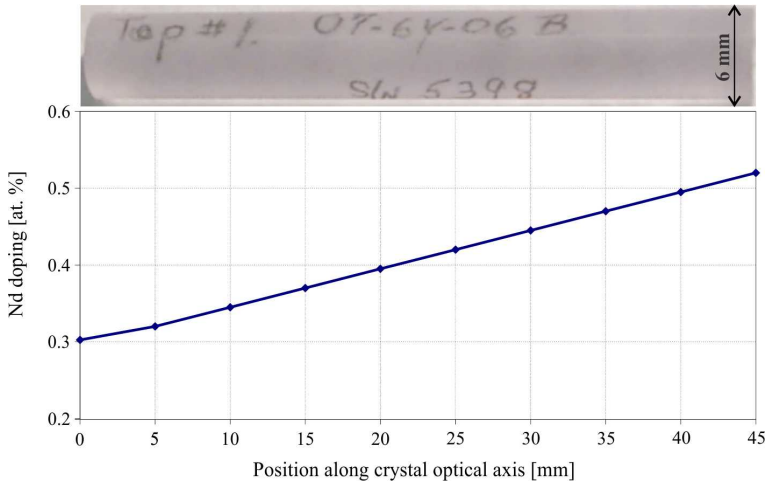

Figure 5.1: A single Nd:YLF crystal from the batch that was used in our experimental setup. The low-doping side was indicated by the manufacturer VLOC with the word *'Top'* on the left-side of the crystal as depicted (Photo credit: W. Koen). The atomic Nd^{3+}-doping concentration within the Nd:YLF crystal as estimated by the manufacturer, VLOC.

Orientation	Axis	Polarisation	Main emission line @ 1.3 µm	Refractive index
Horizontally	c	π	∼1321 nm	n_e= 1.470
Vertically	a	σ	∼1314 nm	n_o= 1.448

Table 5.1: Nd:YLF crystal orientation and polarisation properties.

has been identified as the limiting factor in high-power end-pumped solid-state Nd-doped laser materials (Clarkson et al., 1998; Pollnau et al., 1998a; Zuegel and Seka, 1999). A higher ETU implies a higher heat load and therefore a lower pump limit before thermal fracture occurs. Furthermore, pumping from the lower-doping end-face further reduces the risk of thermal fracture because it spreads out the heat load longitudinally along the crystal (Bollig et al., 2008).

The two Nd:YLF crystals were mounted with the c-axis horizontal, within copper blocks which were maintained at 20°C by water cooling. The crystal orientation implied a horizontal π-polarization for 1321 nm emission and a vertical σ-polarisation for 1314 nm emission (Table 5.1). This orientation was chosen to aid in the selection of the σ-polarization lasing wavelength of 1314 nm within the resonator (see Sections 5.3 and 5.4).

5.2 Pump scheme

As pump light sources we used two Jenoptic laser diode modules of model type JOLD-75-CPXF-2P (Figure 5.2). These modules each delivered up to 75 W of unpolarised CW radiation at ∼803 nm into a 400 µm fibre (0.22 Numerical Aperture) with a beam quality of $M^2 \sim 145$. The two modules were electrically connected in series so that both modules could be controlled by the same power supply and were supplied with the same current. The two modules were characterised and the relation of total pump power P_{pump} (from both laser diode modules togeher) to laser diode current I_{diode} was calculated by a linear regression on

Figure 5.2: One of the two laser diode modules used in this experimental setup. Each module could produce up to 75 W of pump power at ~805 nm. The modules were mounted on a water-cooled copper block for thermal control.

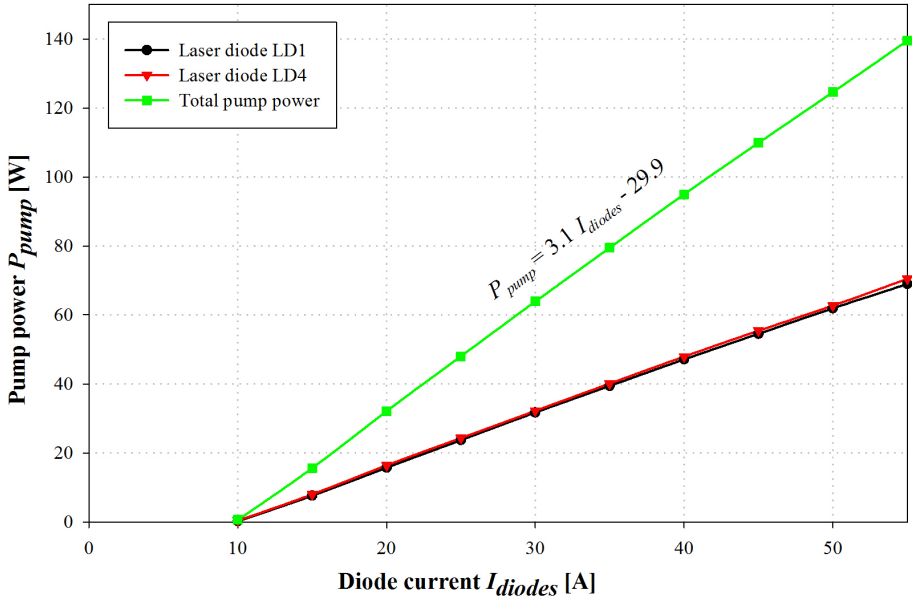

Figure 5.3: The pump power P_{pump} from the 2 laser diodes due to a change in diode module current I_{diode}, as well as the calculated total pump power.

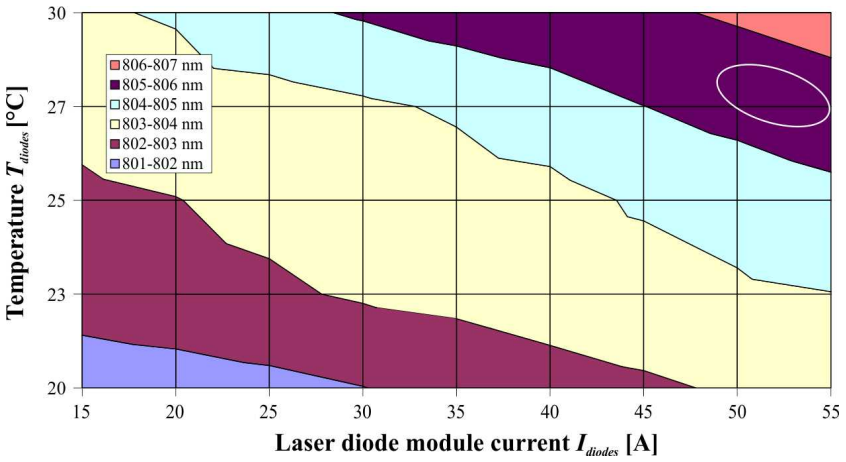

Figure 5.4: Laser diode emission wavelengths λ_{pump} for the Jenoptik JOLD-75-CPXF-2P modules as characterised by Koen (2009), as a function of the diode module current I_{diodes} and junction temperature T_{diodes} within the modules. The white ellipse indicates the full-power working area selected to obtain optimal pump light absorption.

the data as presented in Figure 5.3 to be

$$P_{pump} = 3.1 I_{diodes} - 29.9. \tag{5.1}$$

The output power was limited to 62.5 W per diode ($\sim$125 W in total) to help avoid thermal fracture of the Nd:YLF crystals. The diode modules were mounted on proportional-integral-derivative (PID) temperature controlled thermocouple units, which in turn were water-cooled to 20°C. The exact emission wavelength of a laser diode module λ_{pump} is directly proportional to both the supply current I_{diodes} and the junction temperature within the diode modules T_{diodes}:

$$\lambda_{pump} \propto I_{diodes}, \quad \lambda_{pump} \propto T_{diodes}. \tag{5.2}$$

By precisely controlling the diode current and temperature we could therefore control the pump wavelength within the range of 801 - 807 nm (see Figure 5.4).

Considering the absorption cross-section of Nd:YLF for the 2 polarisations (Figure 3.1), 805.5 nm was determined as an ideal wavelength at full pump power since it maximises the total absorption of the unpolarised pump light and also absorbs into a side-band which will help lower the thermal load. To obtain 805.5 nm output at full pump power (62.5 W / 50 A) we controlled the temperature of the diode modules to 27°C.

For this experimental setup, we determined we determined the ideal pump beam waist radius as 0.4 mm, by using the gain optimisation method of Bollig et al. (2010), as 0.4 mm. Their 1.0 mm pump beam waist radius delivered efficient operation of an Nd:YLF laser at 1053 nm. A higher pump energy density is required to achieve similar levels of gain in our case, since the emission cross-section for 1.3 µm operation is about an order of magnitude lower than for 1.0 µm. We wanted to limit the laser energy density on the resonator optics and since we require a good overlap between the pump and laser modes, and a pump beam waist radius of 0.5 mm was used instead.

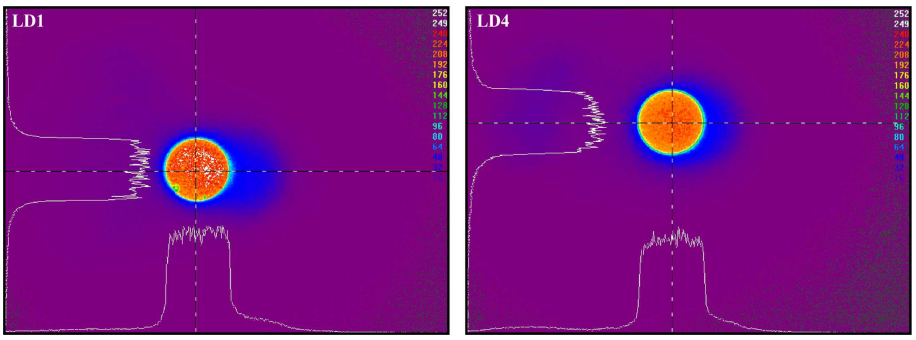

Figure 5.5: Images of the two pump beams at the focus, where it has a top-hat intensity profile and a waist of 0.5 mm radius.

We used the Paraxia simulation software package (Siegman, 2005) to choose a focussing lens and obtain the correct pump beam waist. A Spiricon Point Grey SCOR 20 camera was used to measure the beam waist radius and its position. Images of the top-hat beam profile within the beam waist are depicted in Figure 5.5. The focussing lens positions relative to the fibre tips were adjusted to obtain a measured pump beam waist radius of 0.5 mm for both pumps. By measuring the positions of these beam waists we could locate the pump focus near the centre of each Nd:YLF crystal. These pump beams had a calculated Rayleigh length of 9.9 mm inside the crystals.

5.3 Resonator assuming a netto negative thermal lens

5.3.1 Design and experimental layout

Figures 3.1 and 3.2 depicts the chosen pump and laser wavelengths for the experiments described in this chapter. The literature on thermal lensing in Nd:YLF usually assumes that the negative values of the thermo-optical coefficients dn/dT for both the σ- and π-polarisation are the major contributing factors (see Section 2.5.3). Nd:YLF should therefore exhibit a netto negative thermal lens (see Section 3.1) and the initial resonator design was based on this assumption (see Figure 5.6). All mirrors used in the resonator were 25 mm in diameter and highly transmissive for the pump wavelength region of 806 nm. The CW resonator (Figure 5.6) was formed by using an $r = 200$ mm concave BR and a flat OC. The OCs used had 1.3 µm reflections of 85, 90, 95 and 98%, respectively. The curved-flat resonator type was chosen since it allowed a wide range of laser mode sizes by adjusting the OC or BR positions. Since two Nd:YLF crystals were to be included in the resonator, a flat resonator folding mirror was used to enable end-pumping of one of the Nd:YLF crystals through this mirror while the other Nd:YLF crystal was pumped through the BR.

The BR and OC were chosen to be HR in the 1.3 µm region and HT in the 1.0 µm region, to ensure lasing of only 1.3 µm rather than the stronger 1.0 µm emission lines. Furthermore, the folding mirror was coated to be HR at 1.3 µm, only for light with the electric field parallel to the mirror surface at an incidence angle of 45°. In our setup only the vertically polarised 1.3 µm light experienced a high reflection coefficient. Since the Nd:YLF crystals were oriented to emit the σ-polarisation 1314 nm light vertically (see Section 5.1), the σ-

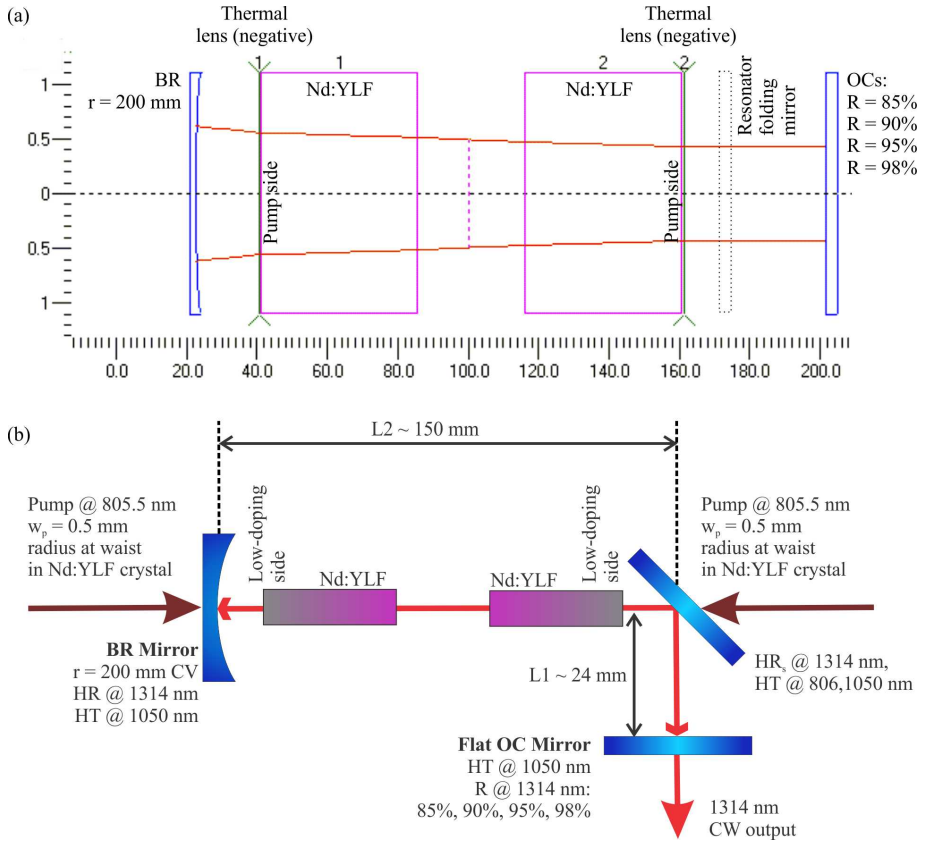

Figure 5.6: (a) The resonator design assuming a netto negative thermal lens. The resonator mode was determined by a simulation in the Psst! Laser Resonators package (Dunn et al., 2014). (b) The resulting experimental resonator layout for 1314 nm CW operation.

polarised light was more likely to be reflected by the folding mirror than the horizontally (π-)polarised 1321 nm light.

5.3.2 Results and discussion of thermal lensing effects

The slope efficiencies for the various OCs are depicted in Figure 5.7. The experimental data match expected behaviour at low ($<$ 40 W per crystal) pump power and the resulting laser beams had symmetrical Gaussian profiles. As the total pump power was increased beyond 80 W, the beam changed to multi-mode and then back to a single mode (as seen on the imaged beam as well as in the output power curves in Figure 5.7), but with a non-symmetrical Gaussian profile. The vertical radius was slightly larger than the horizontal radius. Unfortunately no images of this behaviour were recorded. A maximum output power of 19.0 W was obtained for the 90% OC. The 95% OC delivered results very similar to the 90% OCs. However, the 90% OC implies only half the intra-cavity power of the 95% OC and will therefore help minimise the risk of thermal fracture.

It is evident from Figure 5.6 that the pump power level plays the most important role in the strength of the thermal lens since the unstable behaviour for different OC's all occur at the same pump power level (~90 W). Only for the 98% OC the roll-over effect occurs at a

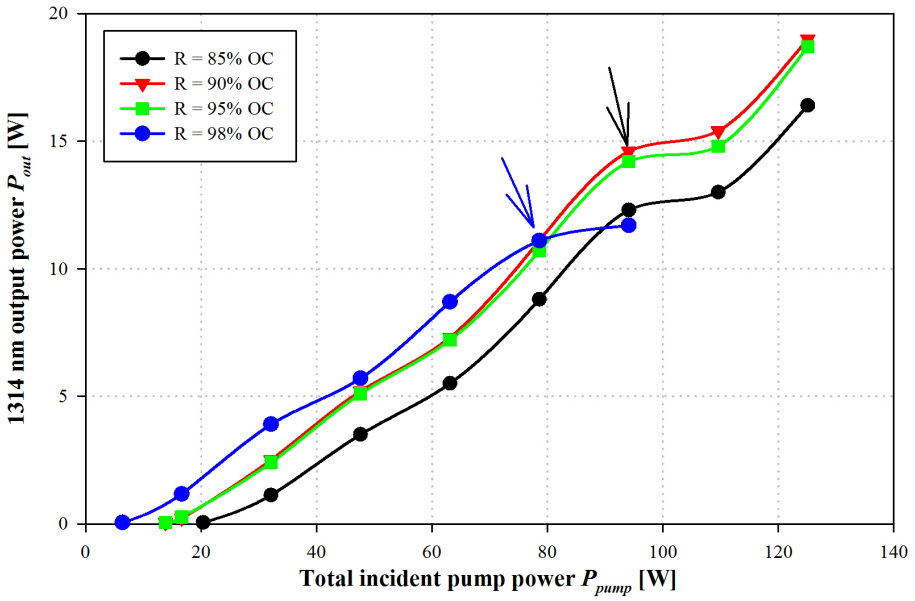

Figure 5.7: Optical-to-optical slope efficiency of the CW laser output. The 98% OC incident pump power was limited to <100 W to limit the intra-cavity power. The arrows indicate where the beams became multi-mode.

lower pump power- this can be ascribed to the higher intra-cavity power which then leads to ETU, and possibly even ESA (see Sections 3.2 and 3.3). This contributes towards a higher heat load within the Nd:YLF crystal and the unstable behaviour due to thermal lensing is observed at a lower pump power level than for the other OCs.

The behaviour of the laser at high pump power due to BR and OC movement was qualitatively very different from the behaviour expected (from software modelling in the Psst!! Laser Resonators package (Dunn et al., 2014)). We noticed that a slight increase in the resonator length resulted in the output becoming unstable, especially at a higher pump power. An increase in pump power also resulted in the output beam becoming more divergent, behaviour not expected from the simulation depicted in Figure 5.6. Various variations on this resonator design as well as completely different resonator designs were tested, all of these behaved as expected only at low pump powers. At higher pump power the laser beam either became multimode or unstable.

Figure 5.8 depicts the modelled laser mode sizes on the BR, OC and in the crystals (average) assuming a wide range of negative and positive thermal lens strengths as for the resonator of Figure 5.6. Stronger pumping will lead to a stronger thermal lens (larger absolute dioptric power). Very strong thermal lens strengths implies unstable behaviour for both positive and negative dioptric powers. For this modelled setup, there are then 2 regions:

- Assuming a negative thermal lens, the laser mode size will increase throughout the resonator for increasing pump power
- Assuming a positive thermal lens, the laser mode size on only the OC will decrease while it increases throughout the rest of the resonator with increasing pump power.

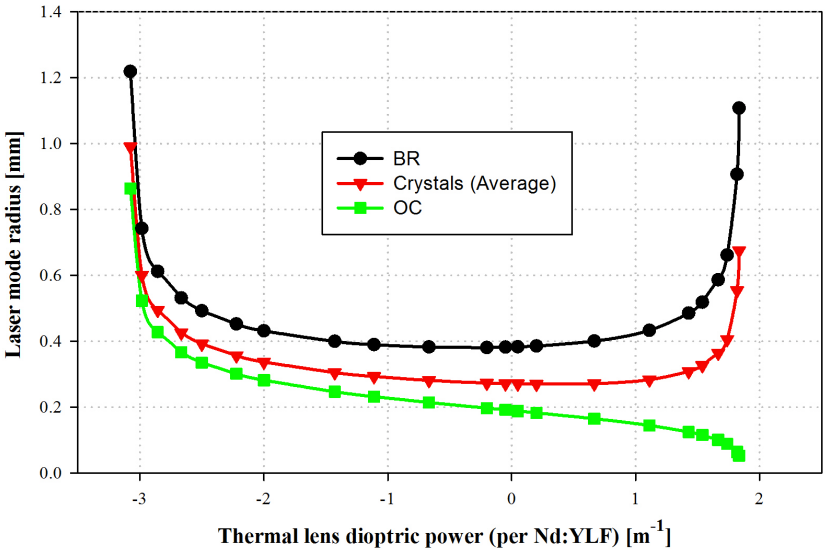

Figure 5.8: Modelled laser mode size radius at various points within the laser resonator (as depicted in Figure 5.6) for a range of thermal lens dioptric powers. The simulations were done in the Psst! Laser Resonators package (Dunn et al., 2014).

> Since the laser mode within the resonator is strongly convergent towards the OC, a focus point is expected near the OC, leading to a strongly diverging beam some distance after the OC.

Considering the observation that an increase in pump power resulted in the output beam becoming more divergent, the resonator must therefore experience a netto positive thermal lens for each crystal, for the σ-polarisation 1314 nm operation of Nd:YLF.

In summary the results therefore indicated that ETU and ESA only becomes relevant at a high intra-cavity power and 1314 nm Nd:YLF has a netto positive thermal lens effect during lasing. Lowering the OC's reflection of laser light will thus reduce the effects of ETU and ESA and designing the resonator for a positive thermal lens should lead to expected results.

5.4 Resonator design assuming a netto positive thermal lens

5.4.1 Design and experimental layout

Subsequently we based our resonator designs on the assumption of a netto positive thermal lens at full pump power (Figure 5.9). All mirrors used in the resonator were 25 mm in diameter and HT for the pump wavelength region of 806 nm. The CW resonator was formed by using an $r = 200$ mm concave BR and a flat 90% OC. This OC was chosen because it resulted in a good optical to optical slope efficiency (Figure 5.7) and had a lower intra-cavity power than for the 95% OC. A flat resonator folding mirror was used to enable end-pumping of both Nd:YLF crystals through this mirror (see Figure 3.6). Using a curved-flat resonator type allowed a wide range of laser mode sizes by adjustment of the OC or BR position. Furthermore this resonator design allows for stable resonator operation over a wide range of

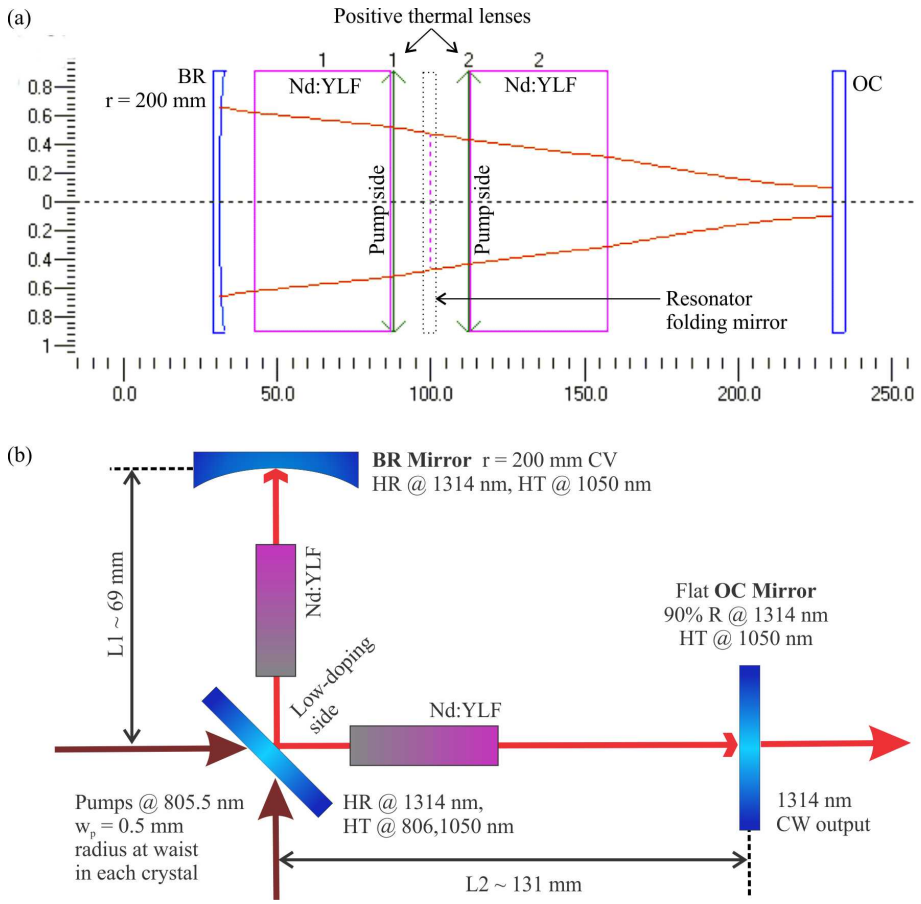

Figure 5.9: a) The resonator design assuming a netto positive thermal lens. The resonator mode was determined by a simulation in Psst! (Dunn et al., 2014). b) The subsequent experimental resonator layout for 1314 nm CW operation.

positive ($f_{th} \gtrsim 1200\,\text{mm}$) as well as negative ($f_{th} \lesssim$-400 mm) thermal lens strengths, which translates to dioptric powers in the range $-2.5\,\text{m}^{-1} \lesssim D_{th} \lesssim 0.83\,\text{m}^{-1}$ for each Nd:YLF crystal.

To ensure 1.3 µm σ-operation the BR, OC and folding mirrors had special coatings, similar as implemented for the previous resonator (see Section 5.3.1). The laser was optimised at full pump power by adjusting both OC and BR positions to mode-match the pump and laser modes within the crystals.

The diagnostic setup used to characterise this CW (Section 5.4) and the subsequent *Q*-switched (Section 5.5) laser operation is depicted diagrammatically in Figure 5.10. Both 1314 nm laser as well as 805.5 nm pump light not absorbed by the crystals, were emitted at the OC. The pump light was removed by a mirror being HR for only the pump wavelength and a once-off measurement was made of the percentage of laser light also being reflected here. The resulting 1314 nm beam was subsequently split up in ~90% and ~10% components for power measurement and further diagnostics. The ~90% laser beam power was measured with a Gentec-EO Maestro power meter with a Gentec UP50N-40S-W9-D0 head. A once-off measurement of the exact percentage of laser light not reflected by this

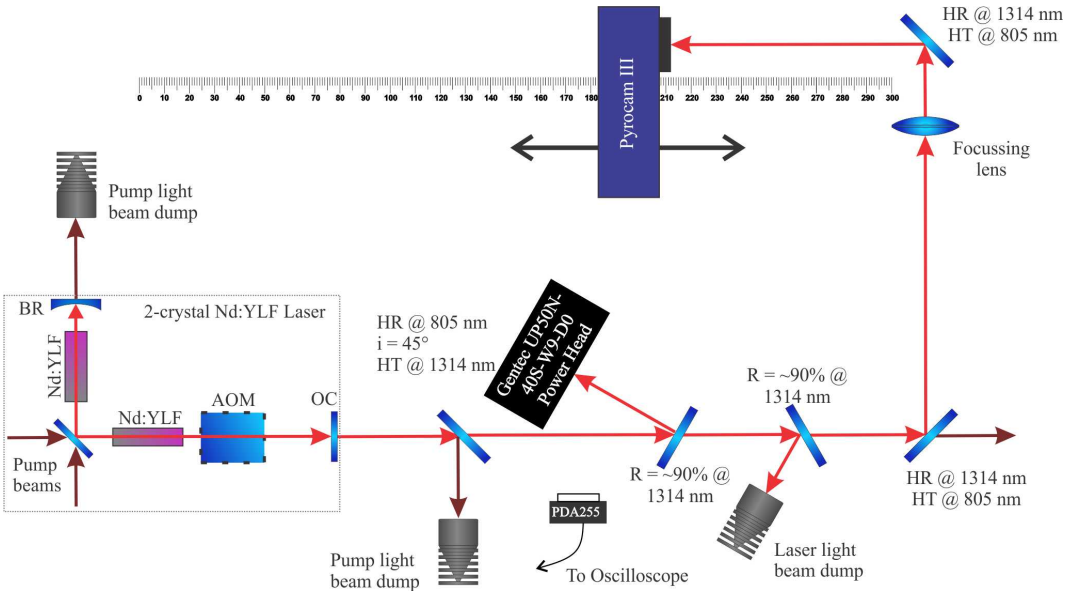

Figure 5.10: Diagnostics setup diagram used for characterising the CW and Q-switched lasers of Sections 5.4 and 5.5.

mirror was also made to calibrate the calculated total laser power output P_{out}. The ~10% beam was attenuated by another ~90% and any remaining pump light was removed. The resulting low-intensity 1314 nm beam was focussed by a lens to create an artificial beam waist. An Ophir Optronics Pyrocam III laser camera was used to image the beam as well as measure the beam diameter at various positions along the focussed beam. During Q-switched operation a Thorlabs PDA255 amplified InGaAs detector was used to detect the laser pulses by measuring light scattered from the power meter head. This detector was connected to a Tektronix DPO5104 oscilloscope which calculated and displayed the various laser pulse parameters. A HighFinesse WS6 IR PID wavelength meter was used to determine the wavelength of the laser.

5.4.2 Results

The slope efficiency of the CW laser is shown in Figure 5.11. The laser had an incident pump power threshold of 15.3 W and a maximum power output of 26.5 W. This result was 2.5 times the value reported in Chapter 4 and 1.4 times the value obtained from the dual crystal laser reported in Section 5.3.2. It was also higher than reported in the literature for a side-pumped setup: 14.9 W of CW output power (Deana et al., 2013). The overall optical-to-optical efficiency was 25% compared to 17% for the $R = 90\%$ OC dual-crystal laser in Section 5.3 and 29% for the single-crystal laser in Chapter 4. Wavelength measurements showed oscillation of only the 1314 nm σ-polarisation. The beam had a symmetrical Gaussian profile but at maximum pump power it became slightly elliptical with a vertical radius ~20% larger than the horizontal. This is due to the astigmatic thermal lensing of Nd:YLF (see Section 3.1). The beam quality was measured as $M_x^2 = 2.0$ and $M_y^2 = 2.6$ (ISO11146-method).

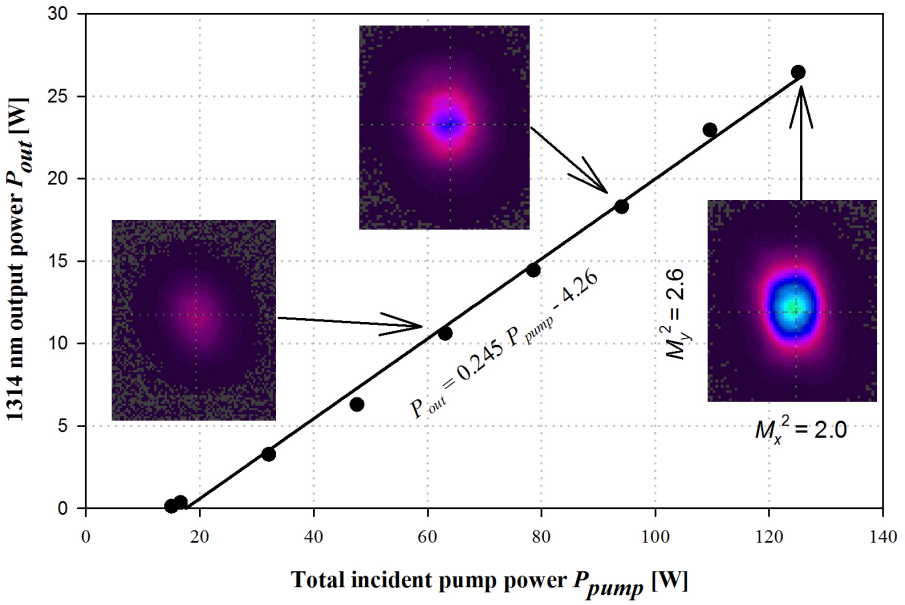

Figure 5.11: Optical-to-optical slope efficiency together with beam profiles of the 1314 nm CW laser. At higher pump powers the beam became slightly elliptical due to astigmatic thermal lensing.

5.5 Actively Q-switched operation

5.5.1 Design and experimental layout

We subsequently inserted an AOM within the CW laser resonator from Section 5.4, to operate the laser in actively Q-switched pulsed mode (Figure 5.12). The Q-switch was a Brewster-cut Gooch & Housego model QS027-10M(BR)-NL6. It was positioned between the one Nd:YLF crystal and the OC. The reflection of the flat OC was decreased to 85% to limit the intra-cavity peak power and energy during pulsed operation, allowing us to operate at a low PRF. The positions of the BR and OC were also slightly adjusted at full pump power to mode-match the pump and laser modes within the Nd:YLF crystals.

The AOM unit was water-cooled to 20°C and was operated with a Gooch & Housego

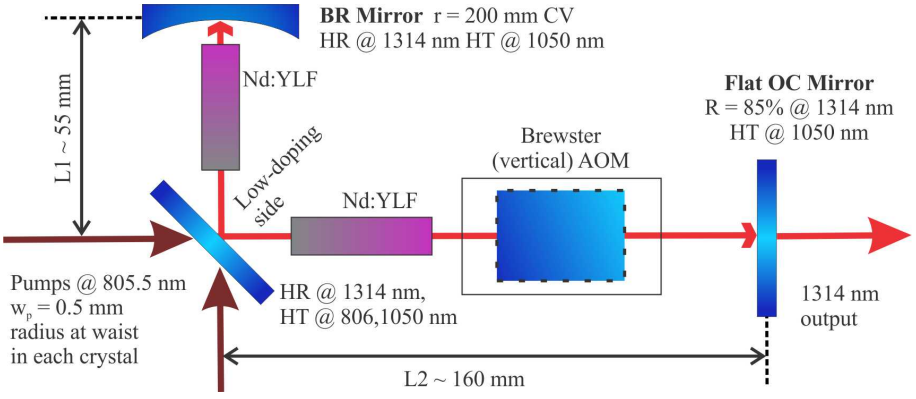

Figure 5.12: Experimental resonator layout for 1314 nm Q-switched operation.

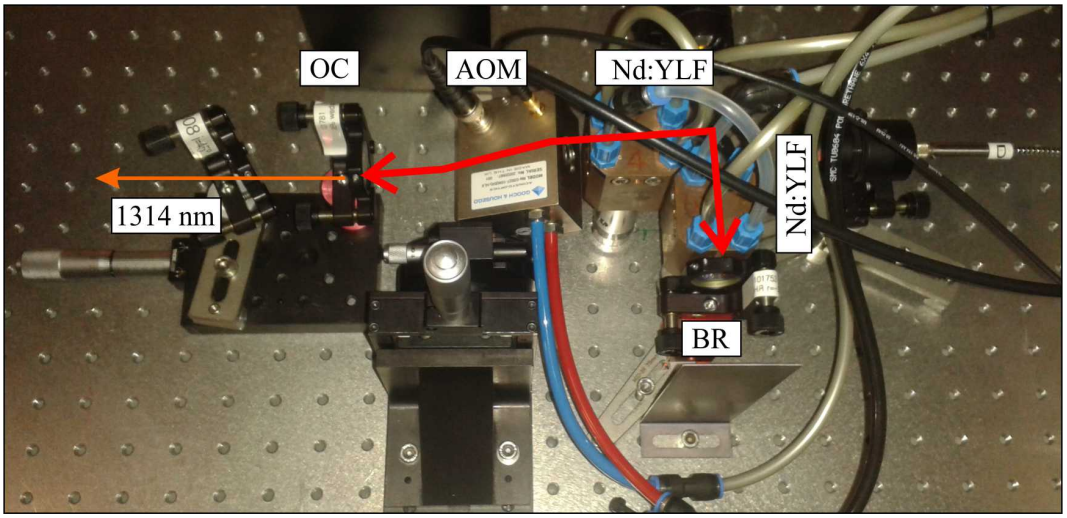

Figure 5.13: The Q-switched resonator setup.

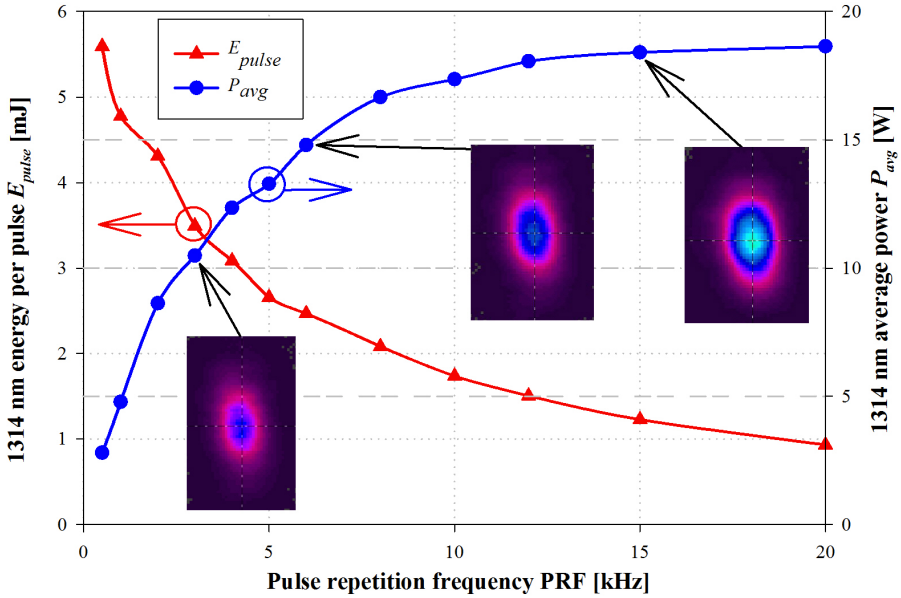

Figure 5.14: Actively Q-switched behaviour at full pump power: energy per pulse E_{pulse} (left axis) and average power P_{avg} (right axis). The beam profiles are slightly elliptical due to astigmatic thermal lensing.

driver (model MQH027-100DS3-A05) which delivered up to 100 W of 27 MHz RF power to the AOM. The driver was controlled by a programmable function generator, a Tektronix AFG3000C. A photo of the implementation of the Q-switched resonator is shown in Figure 5.13.

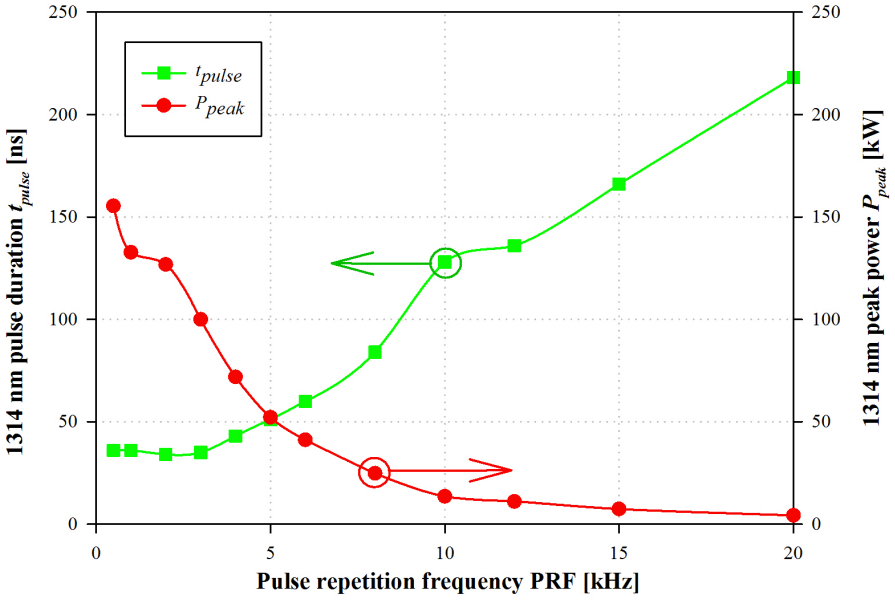

Figure 5.15: Actively Q-switched behaviour at full pump power: Pulse duration t_{pulse} (left axis) and peak power P_{peak} (right axis).

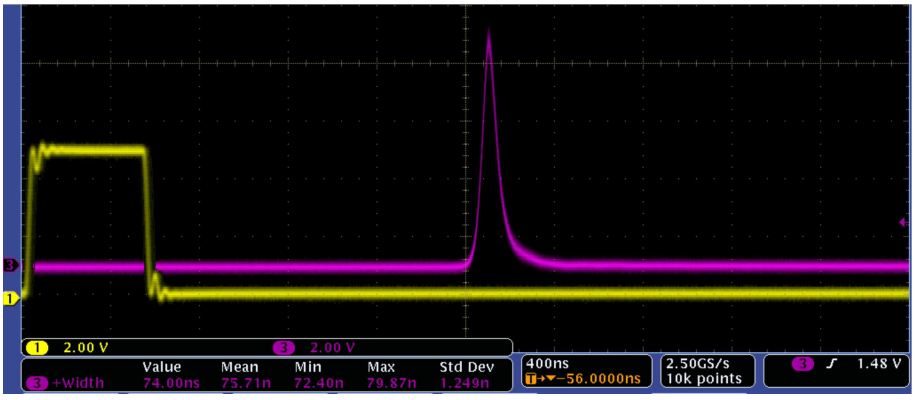

Figure 5.16: The temporal pulse shape (purple) as measured at a PRF of 4 kHz. The AOM high-Q trigger is represented by the yellow line.

5.5.2 Results

The maximum average output power achieved was 18.6 W at an incident pump power of 125 W and a PRF of 20 kHz (Figure 5.14). The decrease in the maximum output power from that of the CW setup of Section 5.4 is attributed to the decrease of the OC reflectivity from 90% to 85% (to help minimise ETU and ESA) as well as an increase in losses within the resonator because of the AOM. The energy per pulse E_{pulse} increased from 0.93 mJ to 5.59 mJ for a decreasing PRF from 20 kHz to 500 Hz.

The highest peak output power P_{peak} of 155 kW was obtained at the PRF of 500 Hz (Figure 5.15). The pulse duration t_{pulse} decreased from 218 ns to 36 ns (FWHM) for a decreasing PRF from 20 kHz to 500 Hz . At a PRF of 4 kHz the laser had a pulse duration

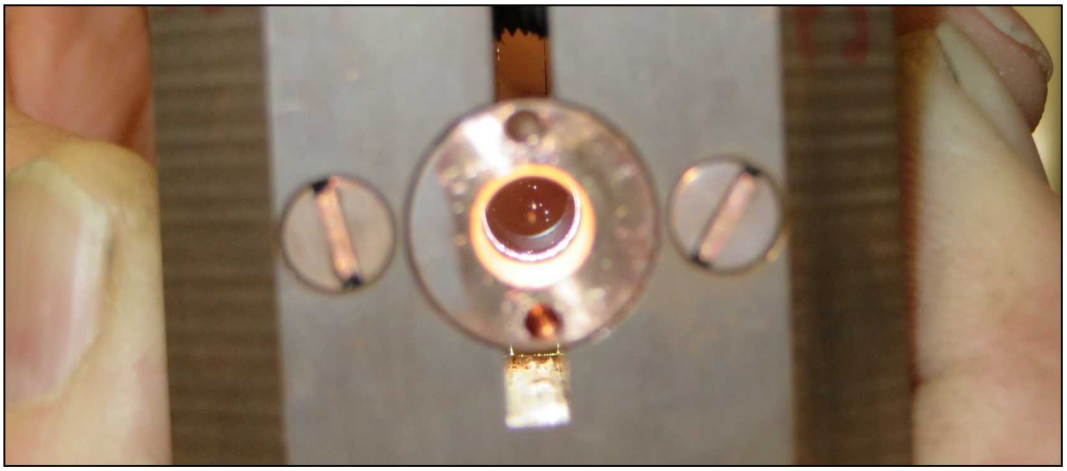

Figure 5.17: The fractured Nd:YLF crystal, with the damage near the pump beam focus position within the crystal.

of 74 ns and the temporal pulse profile is depicted in Figure 5.16. The Q-switched laser had a slightly elliptical beam because of astigmatic thermal lensing (see Section 3.1).

This was, to the best of our knowledge, the first published actively Q-switched diode *end*-pumped 1314 nm Nd:YLF laser. The obtained E_{pulse} and P_{avg} were, to the best of our knowledge, also higher than previously reported (3.8 mJ and 12.3 W respectively) for any diode *side*-pumped actively Q-switched Nd:YLF lasers resonating in the 1.3 µm region (Liu et al., 2014).

5.5.3 Total pump power increase beyond 125 W

The total pump power was subsequently increased to 140 W at a PRF of 20 kHz. The higher pump power at the high pulse repetition rate of 20 kHz did not fracture the crystal, therefore enough energy was extracted from the crystal to keep the overall thermal effects to just below the damage threshold of Nd:YLF. The PRF was subsequently reduced to increase the pulse energy. While decreasing the PRF from 20 kHz, one of the Nd:YLF crystals fractured at a PRF of 12.5 kHz (Figure 5.17). Several micro-fractures occurred within the pump and laser region, from the pump side to about one third into the crystal. These micro-fractures were all much smaller than 1.0 mm in size and were scattered throughout the crystal volume mentioned.

The higher pump power did not fracture the crystal, but the decrease in the PRF did. A decreased PRF allowed for higher levels of population inversion to be obtained. The population inversion level became high enough at a pump power of 140 W and a PRF of 12.5 kHz to enable ETU and subsequent ESA to occur. Since ESA is dependent on ETU first occurring, it leads to a run-away thermal load increase within the Nd:YLF crystal. The sudden increase in heat load resulted in an increase in the thermal stresses, up to a level above the fracture limit for Nd:YLF. The several small micro-fractures observed within the Nd:YLF crystal can be attributed to regions of a slightly higher Nd-doping concentration,

confirming just how sensitive the level of ETU is on the doping concentration. We therefore operated the CW and Q-switched lasers described in Sections 5.4 and 5.5 just below the damage threshold of the Nd:YLF crystals.

5.6 Summary and discussion of results

The experimental setup in Chapter 5 was made with two low-doping Nd:YLF a-cut crystals, mounted with the c-axis horizontally. These crystals were each end-pumped from the lower-doping side by up to 62.5 W of 805.5 nm pump light (up to 125 W of total pump power). The final resonator design assumed a netto positive thermal lens for each of the two Nd:YLF crystals (at full pump power) and consisted of an $r = 200$ mm concave BR and a flat OC (R = 90% for CW and R = 85% for Q-switched operation). The Nd:YLF σ-polarisation of 1314 nm had the potential for high pulse energies and a better beam quality than for the π-polarization of 1321 nm. Operation was forced on the 1314 nm emission line of Nd:YLF by the use of specially coated mirrors. The laser was Q-switched by inserting a brewster-cut AOM in the resonator between the OC and the one Nd:YLF crystal.

The resulting experimental data matched expected behaviour of the laser at low (< 40 W per crystal) pump power but the behaviour at high pump power was qualitatively very different from the modelled behaviour. Resonator modelling assuming a netto positive thermal lens for each Nd:YLF crystal was carried out and did explain the experimental results at high pump powers. We therefore deduced that Nd:YLF can exhibit a netto positive thermal lens at high pump powers. This can be ascribed to the positive lensing effect from end-face bulging becoming more pronounced than the $dn/dT < 0$ at high pump powers.

High average power operation of a diode end-pumped 1314 nm Nd:YLF laser was demonstrated for CW operation, delivering up to 26.5 W of output power. The CW beam quality was measured as $M_x^2 = 2.0$ and $M_y^2 = 2.6$. Active Q-switching resulted in up to 5.59 mJ of energy per pulse at a pulse duration of 36 ns, with an average power of 18.6 W. These results are the highest reported (Botha et al., 2015), considering all Nd-doped end-pumped lasers resonating in the 1.3 µm region.

Chapter 6

Conclusion

There is an international drive in the Geodesy community towards achieving mm-level precision in position measurements. This goal is pursued by upgrading current equipment as well as the development of new measurement technologies. The HartRAO Space Geodesy Programme is currently developing a new Lunar Laser Ranging system. This new LLR system is a next-generation space geodetic technique and aims to achieve sub-centimetre orbital position measurements of the Moon. Initially it will use a Nd:YAG laser with an estimated beam quality of $M^2 \sim 2$, which will lead to an estimated return photon detection rate of $\ll 1$ photon per pulse. Using a laser host material that can deliver better beam quality will result in less beam divergence, which will ensure the detection of more return photons.

Nd:YLF as a laser host material is a promising alternative to Nd:YAG because it should be able to deliver high pulse energies as well as operate with a better beam quality. Operating Nd:YLF on the σ-polarization should result in a weaker thermal lens than for the π-polarization, due to the weakly negative thermo-optical coefficient dn_o/dT associated with it. Investigating Nd:YLF operation on the σ-polarization wavelength of 1314 nm will enable us to quantify an upper limit to the beam quality M^2 expected for 1.3 µm operation. This will enable one to quantify an expected upper limit to the M^2 for 1.0 µm operation, due to the lower thermal load that the gain medium experiences at 1.0 µm than for 1.3 µm operation. High-power 1.3 µm lasers also have a wide range of scientific and commercial applications such as Lidar and large-scale RGB display technologies.

Compared to the excited state lifetime values for Nd:YAG and Nd:YVO_4, the relatively long excited state $^4F_{3/2}$ lifetime of τ_{21} ∼520 µs of Nd:YLF indicates its potential to deliver high pulse energies. The emission cross-section (σ_{em}) for Nd:YLF on the 1.3 µm σ-polarization is $\sim 2.3 \times 10^{-20} cm^2$ which is a factor of 3 less than for Nd:YAG at 1.3 µm. Due to its long excited state lifetime, we know from the $\sigma_{em}\tau_{21}$ product that one can achieve a reasonably low threshold and efficiency for 1.3 µm Nd:YLF.

Using a relatively low Nd doping concentration within the YLF crystal as well as pumping from the lower-doping crystal end-face reduces ETU. Reducing the ETU will also result in a reduction of ESA, which is dependent on ETU. Thermal effects due to ESA become especially pronounced during Q-switched operation. A reduction in the Nd doping reduces

the ETU and therefore ESA - this helps to spread out the thermal load longitudinally in the crystal, which increases the thermal fracture pump limit.

The power-scaling of 1314 nm Nd:YLF lasers was investigated for CW, passively Q-switched and actively Q-switched operation. These lasers were operated at power levels up to the damage threshold.

A single-crystal 1314 nm Nd:YLF laser was demonstrated. In CW mode it delivered up to 10.4 W of output power. This result was ~70% higher than reported in the literature at that time. Passively Q-switched operation was achieved by using a V:YAG saturable absorber. This was the first demonstration of a Nd:YLF laser being passively $Q-$switched with V:YAG. Pulsed operation delivered 825 µJ of energy per pulse with a pulse duration of 135 ns and an average power of 5.2 W. The pulsed beam had a slight elliptical shape due to astigmatism and beam quality factors of $M_x^2 = 1.70$ and $M_y^2 = 1.99$, respectively. The Q-switched power and energy results obtained were, at that time, higher than reported for any diode end-pumped Nd laser at 1.3 µm being passively Q-switched with V:YAG.

A dual-crystal Nd:YLF laser was subsequently designed and built. The resulting experimental data at high pump power was qualitatively very different from the behaviour as expected from modelling behaviour. Through resonator modelling it was realised that the Nd:YLF crystals exhibited a netto positive thermal lens during lasing. Implementation of a resonator design which assumed a positive thermal lens led to experimental results which followed the modelled behaviour at high pump power. We concluded that Nd:YLF exhibits a netto positive thermal lens at high pump powers, this result being ascribed to the positive lensing effect from end-face bulging being slightly more pronounced than that of the negative thermo-optical coefficient dn_o/dT. Subsequently, high average power operation of a diode end-pumped dual-crystal 1314 nm Nd:YLF laser was demonstrated for both CW as well as actively Q-switched modes. In CW mode it delivered up to 26.5 W of output power, with a beam quality of $M_x^2 = 2.0$ and $M_y^2 = 2.6$ respectively. Active Q-switching resulted in up to 5.59 mJ of energy per pulse at a pulse duration of 36 ns, with an average power of 18.6 W. These CW and pulsed results were, at the time, higher than reported for any Nd-doped end-pumped lasers operating in the 1.3 µm region.

Power-scaling of 1314 nm Nd:YLF lasers was therefore successfully demonstrated for CW, as well as passively and actively $Q-$switched operation. The resulting CW power and pulse energies were higher than reported at that stage for any Nd-doped 1.3 µm lasers in an end-pumped configuration. These results indicate that Nd:YLF is an ideal active medium to obtain high output power and pulse energies for lasers operating in the 1.3 µm region, and that further power-scaling of 1.0 µm Nd:YLF should also result in very high output power and pulse energy, with an expected beam quality of $M^2 < 2$.

Further investigation into Nd:YLF lasers for the use in Lunar Laser Ranging should therefore be undertaken. The energy-scaling of σ-polarization 1053 nm Nd:YLF lasers delivering $M^2 < 2$ mode-locked Q-switched (< 20 ps) pulses at the millijoule level is of special interest. These experiments require stronger pump sources, longer Nd:YLF crystals rods of a low doping (for increased absorption), optics that will be able to handle the peak energies and additional optical elements to obtain mode-locking and pulse-picking.

List of Publications

Journal Articles

Botha, R. C., Strauss, H. J., Bollig, C., Koen, W., Collett, O., Kuleshov, N. V., Esser, M. J. D., Combrinck, W. L., von Bergmann, H. M. March 2013. High average power 1314 nm Nd:YLF laser, passively $Q-$switched with V:YAG. Optics Letters 38 (6), 980-982. doi: 10.1364/OL.38.000980. URL http: //ol.osa.org/abstract.cfm?URI=ol-38-6-980.

Botha, R. C., Koen, W., Esser, M. J. D., Bollig, C., Combrinck, W. L., von Bergmann, H. M., Strauss, H. J., Feb. 2015. High average power Q-switched 1314 nm two-crystal Nd:YLF laser. Optics Letters, 40 (4), 495-497. doi: 10.1364/OL.40.000495. URL http: //ol.osa.org/abstract.cfm?URI=ol-40-4-495.

International Conference Papers

Bollig, C., **Botha, R. C.**, Ngcobo, S., Kuleshov, N. V., Esser, M. J. D., Nov 2005. High-power CW and passively Q-switched 1314-nm end-pumped Nd:YLF laser. Conference on Mid-Infrared Coherent Sources (MICS 2005), We6, Barcelona, Spain.

Bollig, C., Koen, W., Strauss, H., Bernhardi, E., **Botha, R. C.**, Esser, M. J. D., Preussler, D., 2008. Exploiting the natural doping gradient of Nd:YLF crystals for high-power end-pumped lasers. In: 3rd EPS-QEOD Europhoton Conference, Paper TUp.20, Paris, France.

International Workshop Papers

Botha, R. C., Combrinck, W. L., Nov. 2013. System design of the South African Lunar Laser Ranger. In: Proceedings of the 18th International Workshop on Laser Ranging, Fujiyoshida, Japan. URL http://cddis.gsfc.nasa.gov/lw18/

Combrinck, W. L., **Botha, R. C.**, Nov. 2013. Challenges and progress with the development of a Lunar Laser Ranger for South Africa. In: Proceedings of the 18th International Workshop on Laser Ranging, Fujiyoshida, Japan. URL http://cddis.gsfc.nasa.gov/lw18/.

National Conference Papers

Bollig, C., Jacobs, C., **Botha, R. C.**, Ngcobo, S., Strauss, H. J., Burger, J. P., von Bergmann, H. M., Esser, M. J. D., Preussler, D., Moodley, M. K., July 2005. Diode-Pumped Solid-State Laser Research in South Africa. In: 50th annual conference of the South African Institute of Physics, talk C-18, Pretoria.

Botha, R. C., Bollig, C., Koen, W. S., Kuleshov, N. V., July 2005. High-Power Continuous-Wave and Passively Q-switched 1314 nm Nd:YLF laser. In: 50th annual conference of the South African Institute of Physics, talk C-22, Pretoria.

Strauss, H. J., Bollig, C., **Botha, R. C.**, von Bergmann, H. M., Burger, J. P., July 2006. High power vanadate lasers. In: 51st annual conference of the South African Institute of Physics, talk C-9, University of the Western Cape, Cape Town.

Bollig, C., Preussler, D., Esser, M. J. D., Ngcobo, S., Jacobs, C., **Botha, R. C.**, Koen, W. S., Bernhardi, E. H., Sarmani, A. R., Botha, L. R., July 2007. Solid-state laser source research at the CSIR - National Laser Centre. In: 52nd annual conference of the South African Institute of Physics, talk 419, University of the Witwatersrand, Johannesburg.

Koen, W. S., Bollig, C., Forbes, A., Sarmani, A. R., **Botha, R. C.,** Esser, M. J. D., July 2007. Ultra short-pulse (USP) laser development. *52nd annual conference of the South African Institute of Physics*, talk 366, University of the Witwatersrand, Johannesburg.

Botha, R. C., Bollig, C., Koen, W. S., Saramani, A. R., Botha, L. R., Jacobs, C., July 2007. Energy scaling techniques in ultra-short pulse lasers. In: 52nd annual conference of the South African Institute of Physics, talk 373, University of the Witwatersrand, Johannesburg.

Koen, W. S., Bollig, C., Strauss, H., **Botha, R. C.**, Bernhardi, E., Esser, M. J. D., July 2008. Power Scaling of a High-Power End-Pumped Nd:YLF Laser. In: 53rd annual conference of the South African Institute of Physics, talk 152, University of Limpopo, Polokwane.

Botha, R. C., Strauss, H., Combrinck, W. L., von Bergmann, H. M., July 2013. A 2-crystal high-power CW and Q-switched Nd:YLF laser at 1314nm. In: 58th annual conference of the South African Institute of Physics, talk 479, University of Zululand, Richards Bay. URL http://events.saip.org.za/contributionDisplay.py?contribId=479&sessionId=3&confId=32

Ndlovu, S., Combrinck, W. L., Nkosi, N., **Botha, R. C.**, July 2015. An Integrated Software Based Analytical Model for the Signal Path Efficiency of the HartRAO Lunar Laser Ranger Optical System. In: 60th annual conference of the South African Institute of Physics, talk 96, Nelson Mandela Metropolitan University, Port Elizabeth. URL http://events.saip.org.za/contributionDisplay.py?contribId=96&sessionId=20&confId=53

Bibliography

Altmann, K., Altmann, G., 2005. Laser Cavity Analysis and Design (LAS-CAD).
URL https://www.las-cad.com/

Bollig, C., 1997. Single-frequency diode-pumped solid-state lasers. PhD thesis, University of Southampton, Southampton, United Kingdom.

Bollig, C., Jacobs, C., Esser, M. J. D., Bernhardi, E. H., von Bergmann, H. M., Jun. 2010. Power and energy scaling of a diode-end-pumped Nd:YLF laser through gain optimization. Optics Express 18 (13), 13993–14003.
URL http://www.opticsexpress.org/abstract.cfm?URI=oe-18-13-13993

Bollig, C., Koen, W., Strauss, H., Bernhardi, E. H., Botha, R., Esser, D., Preussler, D. R., 2008. Exploiting the natural doping gradient of Nd:YLF crystals for high-power end pumped lasers. In: 3rd EPS-QEOD Europhoton Conference. European Physical Society, Paris, France.
URL http://researchspace.csir.co.za/dspace/handle/10204/3317

Botha, R. C., Combrinck, W. L., Nov. 2013. System design of the South African Lunar Laser Ranger. In: Proceedings of the 18th International Workshop on Laser Ranging. Fujiyoshida, Japan.
URL http://cddis.gsfc.nasa.gov/lw18/

Botha, R. C., Koen, W., Esser, M. J. D., Bollig, C., Combrinck, W. L., von Bergmann, H. M., Strauss, H. J., Feb. 2015. High average power Q-switched 1314 nm two-crystal Nd:YLF laser. Optics Letters 40 (4), 495–497.
URL http://ol.osa.org/abstract.cfm?URI=ol-40-4-495

Botha, R. C., Strauss, H. J., Bollig, C., Koen, W., Collett, O., Kuleshov, N. V., Esser, M. J. D., Combrinck, W. L., von Bergmann, H. M., Mar. 2013. High average power 1314 nm Nd:YLF laser, passively Q-switched with V:YAG. Optics Letters 38 (6), 980–982.
URL http://ol.osa.org/abstract.cfm?URI=ol-38-6-980

Castech, 2015. Castech Crystal Catalog (2012-2013). Catalog.
URL http://www.castech.com/

Chuang, T., Verdun, H., Jan. 1996. Energy transfer up-conversion and excited state absorption of laser radiation in Nd:YLF laser crystals. IEEE Journal of Quantum Electronics 32 (1), 79–91.

Clarkson, W. A., Aug. 2001. Thermal effects and their mitigation in end-pumped solid-state lasers. Journal of Physics D: Applied Physics 34 (16), 2381.
URL http://iopscience.iop.org/0022-3727/34/16/302

Clarkson, W. A., Hardman, P. J., Hanna, D. C., 1998. High-power diode-bar end-pumped Nd:YLF laser at 1.053 µm. Optics Letters 23 (17), 1363–1365.
URL http://ol.osa.org/abstract.cfm?URI=ol-23-17-1363

Combrinck, W. L., Botha, R. C., Nov. 2013. Challenges and progress with the development of a Lunar Laser Ranger for South Africa. In: Proceedings of the 18th International Workshop on Laser Ranging. Fujiyoshida, Japan.
URL http://cddis.gsfc.nasa.gov/lw18/

Cousins, A., Apr. 1992. Temperature and thermal stress scaling in finite-length end-pumped laser rods. IEEE Journal of Quantum Electronics 28 (4), 1057–1069.
URL http://ieeexplore.ieee.org/xpl/tocresult.jsp?isnumber=3682

Czeranowsky, C., 2002. Resonatorinterne Frequenzverdopplung von diodengepumpten Neodym-Lasern mit hohen Ausgangsleistungen im blauen Spektralbereich. PhD, University of Hamburg, Hamburg.

Deana, A. M., Lopez, M. A. P. A., Wetter, N. U., Oct. 2013. Diode-side-pumped Nd:YLF laser emitting at 1313 nm based on DBMC technology. Optics Letters 38 (20), 4088–4091.
URL http://ol.osa.org/abstract.cfm?URI=ol-38-20-4088

Degnan, J. J., 1993. Millimeter Accuracy Satellite Laser Ranging: a Review. In: Smith, D. E., Turcotte, D. L. (Eds.), Contributions of Space Geodesy to Geodynamics: Technology. American Geophysical Union, pp. 133–162.
URL http://onlinelibrary.wiley.com/doi/10.1029/GD025p0133/summary

Degnan, J. J., Oct. 2002. Asynchronous laser transponders for precise interplanetary ranging and time transfer. Journal of Geodynamics 34 (3–4), 551–594.
URL http://www.sciencedirect.com/science/article/pii/S0264370702000443

Dunn, M., Sinclair, B., Lindsay, P., Gillies, A., 2014. Photonics Simulation Software for Teaching (Psst!).
URL http://www.st-andrews.ac.uk/~psst/

Einstein, A., 1917. Zur Quantentheorie der Strahlung. Physikalische Zeitschrift XVIII.
URL http://adsabs.harvard.edu/abs/1917PhyZ...18..121E

Esser, M. J. D., 2005. Diode-end-pumped solid-state lasers. Thesis, University of Stellenbosch, Stellenbosch, South Africa.
URL https://scholar.sun.ac.za/handle/10019.1/2796

Fornasiero, L., Kellner, T., Kück, S., Meyn, J. P., Möbert, P. E.-A., Huber, G., Jan. 1999. Excited state absorption and stimulated emission of Nd^{3+} in crystals III: $LaSc_3(BO_3)_4$, $CaWO_4$, and $YLiF_4$. Applied Physics B 68 (1), 67–72.
URL http://link.springer.com/article/10.1007/s003400050587

Fornasiero, L., Kück, S., Jensen, T., Huber, G., Chai, B. H. T., Nov. 1998. Excited state absorption and stimulated emission of Nd^{3+} in crystals. Part 2: YVO_4, $GdVO_4$, and $Sr_5(PO_4)_3F$. Applied Physics B 67 (5), 549–553.
URL http://link.springer.com/article/10.1007/s003400050543

Guochang, X., Aug. 2012. Sciences of Geodesy - II: Innovations and Future Developments. Springer Science & Business Media.

Hardman, P. J., Clarkson, W. A., Friel, G. J., Pollnau, M., Hanna, D. C., Apr. 1999. Energy-transfer upconversion and thermal lensing in high-power end-pumped Nd:YLF laser crystals. IEEE Journal of Quantum Electronics 35 (4), 647–655.

Hobbs, P. C. D., 2000. Building Electro-Optical Systems: Making It all Work, 1st Edition. Wiley, Hoboken, NJ.

Hodgson, N., Weber, H., Jun. 2005. Laser Resonators and Beam Propagation: Fundamentals, Advanced Concepts and Applications, 2nd Edition, 2nd Edition. Springer, New York.

Hu, X. P., Zhao, G., Yan, Z., Wang, X., Gao, Z. D., Liu, H., He, J. L., Zhu, S. N., Feb. 2008. High-power red-green-blue laser light source based on intermittent oscillating dual-wavelength Nd:YAG laser with a cascaded $LiTaO_3$ superlattice. Optics Letters 33 (4), 408–410.
URL http://ol.osa.org/abstract.cfm?URI=ol-33-4-408

Jabczynski, J. K., Kopczynski, K., Mierczyk, Z., Agnesi, A., Guandalini, A., Reali, G., 2001. Application of V(3+):YAG crystals for Q-switching and mode-locking of 1.3-μm diode-pumped neodymium lasers. Optical Engineering 40 (12), 2802.
URL http://link.aip.org/link/OPEGAR/v40/i12/p2802/s1&Agg=doi

Koechner, W., Jan. 1999. Solid-state laser engineering (5th edition). Springer Science & Business Media.

Koen, W. S., 2009. End-pumped solid-state lasers. M.Sc. Dissertation, University of KwaZulu-Natal, Westville.

Krennrich, D., Knappe, R., Henrich, B., Wallenstein, R., L'huillier, J. A., Aug. 2008. A comprehensive study of Nd:YAG, Nd:YAlO3, Nd:YVO4 and Nd:YGdVO4 lasers operating at wavelengths of 0.9 and 1.3 μm. Part 1: cw-operation. Applied Physics B 92 (2), 165–174.
URL http://link.springer.com/article/10.1007/s00340-008-3069-4

Liu, S., Dong, L., Zhang, B., He, J., Wang, Z., Ning, J., Wang, R., Liu, X., Mar. 2014. Generation of high power laser at 1314 nm from a diode-side-pumped Nd:YLF module. Chinese Optics Letters 12 (3), 031402.
URL http://col.osa.org/abstract.cfm?URI=col-12-3-031402

Louyer, Y., Plimmer, M. D., Juncar, P., Himbert, M. E., Balembois, F., Georges, P., 2003. Nd:YLF Laser at 1.3 µm for Calcium Atom Optical Clocks and Precision Spectroscopy of

Hydrogenic Systems. Applied Optics 42 (24), 4867–4870.
URL http://ao.osa.org/abstract.cfm?URI=ao-42-24-4867

Ma, Z., Li, D., Gao, J., Wu, N., Du, K., Jul. 2007. Thermal effects of the diode end-pumped Nd:YVO_4 slab. Optics Communications 275 (1), 179–185.
URL http://www.sciencedirect.com/science/article/pii/S0030401807002568

Malyarevich, A., Denisov, I., Yumashev, K., Mikhailov, V., Conroy, R., Sinclair, B., Nov. 1998. V:YAG - a new passive Q-switch for diode-pumped solid-state lasers. Applied Physics B: Lasers and Optics 67 (5), 555–558.
URL http://www.springerlink.com/content/dwrd5f00ax8xefw0/

Mikhailov, V. P., Kuleshov, N. V., Zhavoronkov, N. I., Prokohsin, P. V., Yumashev, K. V., Sandulenko, V. A., Oct. 1993. Optical absorption and nonlinear transmission of tetrahedral V^{3+} (d2) in yttrium aluminum garnet. Optical Materials 2 (4), 267–272.
URL http://www.sciencedirect.com/science/article/B6TXP-46JYHBF-27/2/418ab96bb3b86f2e546363fb312d0cf8

Murray, J. T., Powell, R. C., Peyghambarian, N., Smith, D., Austin, W., Stolzenberger, R. A., May 1995. Generation of 1.5 µm radiation through intracavity solid-state Raman shifting in $Ba_3(NO)_2$ nonlinear crystals. Optics Letters 20 (9), 1017–1019.
URL http://ol.osa.org/abstract.cfm?URI=ol-20-9-1017

Ndlovu, S., Combrinck, W. L., Nkosi, N., Botha, R. C., Jul. 2015. An Integrated Software Based Analytical Model for the Signal Path Efficiency of the HartRAO Lunar Laser Ranger Optical System. 60th annual conference of the South African Institute of Physics.
URL http://events.saip.org.za/contributionDisplay.py?contribId=96&sessionId=20&confId=53

Ohanian, H. C., Jan. 1995. Modern Physics. Prentice-Hall.

Paschotta, R., Apr. 2015. Solid-state Lasers.
URL http://www.rp-photonics.com/solid_state_lasers.html

Podlipensky, A., Yumashev, K., Kuleshov, N., Kretschmann, H., Huber, G., 2003. Passive Q-switching of 1.44 μm and 1.34 μm diode-pumped Nd:YAG lasers with a V:YAG saturable absorber. Applied Physics B: Lasers and Optics 76 (3), 245–247.
URL http://www.springerlink.com/content/r7cxjvh7j8w7tbgw/abstract/

Pollnau, M., Hardman, P., Clarkson, W., Hanna, D., Feb. 1998a. Upconversion, lifetime quenching, and ground-state bleaching in Nd^{3+}:$LiYF_4$. Optics Communications 147 (1-3), 203–211.
URL http://www.sciencedirect.com/science/article/pii/S0030401897005245

Pollnau, M., Hardman, P. J., Kern, M. A., Clarkson, W. A., Hanna, D. C., Dec. 1998b. Upconversion-induced heat generation and thermal lensing in Nd:YLF and Nd:YAG. Physical Review B 58 (24), 16076–16092.
URL http://link.aps.org/doi/10.1103/PhysRevB.58.16076

Prochazka, I., Schreiber, U., Schäfer, W., Jan. 2011. Laser time transfer and its application in the Galileo programme. Advances in Space Research 47 (2), 239–246.
URL http://www.sciencedirect.com/science/article/pii/S0273117710001134

Ryan, J. R., Beach, R., Oct. 1992. Optical absorption and stimulated emission of neodymium in yttrium lithium fluoride. Journal of the Optical Society of America B 9 (10), 1883–1887.
URL http://josab.osa.org/abstract.cfm?URI=josab-9-10-1883

Sato, Y., Taira, T., May 2007. Thermo-Optical and -Mechanical Parameters of Nd:$GdVO_4$ and Nd:YVO_4. In: Conference on Lasers and Electro-Optics/Quantum Electronics and Laser Science Conference and Photonic Applications Systems Technologies (2007), paper JWA87. Optical Society of America, p. JWA87.
URL http://www.osapublishing.org/abstract.cfm?uri=QELS-2007-JWA87

Siegman, A. E., Jan. 1986. Lasers. University Science Books.

Siegman, T., Oct. 2005. Paraxia-Plus.
URL http://www.sciopt.com/

Sulc, J., 2004. V:YAG saturable absorber for flash-lamp and diode-pumped solid state lasers. Vol. 5460. SPIE, pp. 292–302.
URL http://spie.org/x648.html?product_id=544822

Sun, X., Skillman, D. R., Hoffman, E. D., Mao, D., McGarry, J. F., McIntire, L., Zellar, R. S., Davidson, F. M., Fong, W. H., Krainak, M. A., Neumann, G. A., Zuber, M. T., Smith, D. E., Jan. 2013. Free space laser communication experiments from Earth to the Lunar Reconnaissance Orbiter in lunar orbit. Optics Express 21 (2), 1865–1871.
URL http://www.opticsexpress.org/abstract.cfm?URI=oe-21-2-1865

Walters, D. L., Bradford, L. W., Oct. 1997. Measurements of r_0 and θ_0: two decades and 18 sites. Applied Optics 36 (30), 7876–7886.
URL http://ao.osa.org/abstract.cfm?URI=ao-36-30-7876

Weber, R., Neuenschwander, B., Weber, H. P., Jan. 1999. Thermal effects in solid-state laser materials. Optical Materials 11 (2–3), 245–254.
URL http://www.sciencedirect.com/science/article/pii/S0925346798000470

Wei, Y., Xu, S., Huang, C., Zhuang, F., Chen, W., Huang, L., Wang, X., Zhang, G., 2012. 6.2 W diode-end-pumped 1313 nm Nd:YLF laser. Laser Physics 22 (6), 1029–1032.
URL http://www.springerlink.com/content/w5175g47471g8r78/abstract/

Wetter, N. U., Deana, A. M., Jul. 2014. Power scaling of a side-pumped Nd:YLF laser based on DBMC technology. Applied Physics B 117 (3), 855–860.
URL http://link.springer.com/article/10.1007/s00340-014-5897-8

Wetter, N. U., Deana, A. M., Apr. 2015. Influence of pump bandwidth on the efficiency of side-pumped, double-beam mode-controlled lasers: establishing a new record for Nd:$YLiF_4$ lasers using VBG. Optics Express 23 (7), 9379.
URL https://www.osapublishing.org/oe/abstract.cfm?uri=oe-23-7-9379

Zuegel, J. D., Seka, W., Apr. 1999. Upconversion and Reduced $^4F_{3/2}$ Upper-State Lifetime in Intensely Pumped Nd:YLF. Applied Optics 38 (12), 2714.
URL https://www.osapublishing.org/ao/abstract.cfm?uri=ao-38-12-2714

Appendix A

High average power 1314 nm Nd:YLF laser, passively Q-switched with V:YAG

High average power 1314 nm Nd:YLF laser, passively *Q*-switched with V:YAG

R. C. Botha,[1,2,*] H. J. Strauss,[2,3] C. Bollig,[2,4] W. Koen,[2,3] O. Collett,[2,3] N. V. Kuleshov,[5] M. J. D. Esser,[3] W. L. Combrinck,[1] and H. M. von Bergmann[2]

[1]*HartRAO, P.O. Box 443, Krugersdorp 1740, South Africa*

[2]*Stellenbosch University, P/Bag X1, Matieland 7602, South Africa*

[3]*National Laser Centre, Council for Scientific and Industrial Research, P.O. Box 395, Pretoria 0001, South Africa*

[4]*Physics Department, Carl von Ossietzky University, Oldenburg 26111, Germany*

[5]*Centre for Optical Materials and Technologies, Belarus National Technical University, Minsk, Belarus*

**Corresponding author: roelf@hartrao.ac.za*

Received November 22, 2012; revised February 8, 2013; accepted February 8, 2013; posted February 11, 2013 (Doc. ID 180380); published March 14, 2013

A 1314 nm Nd:YLF laser was designed and operated both CW and passively *Q*-switched. Maximum CW output of 10.4 W resulted from 45.2 W of incident pump power. Passive *Q*-switching was obtained by inserting a V:YAG saturable absorber in the cavity. The oscillator delivered a maximum of 825 μJ energy per pulse, with a pulse duration of 135 ns at a pulse repetition frequency of 6.3 kHz, effectively delivering 5.2 W of average power. © 2013 Optical Society of America

OCIS codes: 140.0140, 140.3070, 140.3480, 140.3530, 140.3540.

High-power 1.3 μm lasers have a wide range of applications, which include communications, sensing, timing systems, and monitoring techniques. The 1.3 μm output can be Raman-shifted to the 1.5 μm region, which is useful for applications requiring eye-safe operation at high powers, such as Lidar and free-space optical communication [1]. Furthermore, 1314.0 nm (specifically the 657.0 nm harmonic) is required to probe the relevant transition [2] for optical calcium clocks.

The main 1.3 μm emission lines of Nd:YLF are at 1314 nm for the σ polarization and 1321 nm for the π polarization. To our knowledge, the highest 1.3 μm CW output power reported from a diode-end-pumped Nd:YLF laser is 6.2 W [3], which leaves room for power scaling as was done for 1.0 μm Nd:YLF [4,5], or 1.3 μm Nd:YAG, and Nd:$GdVO_4$ [6,7] lasers. Operating an end-pumped Nd:YLF laser at 1.3 μm is attractive because of the weak thermal lens when it is operated on the σ polarization [8,9]. This results in excellent beam quality over a wide range of output powers.

Nd:YLF also has a long upper-laser-level ($^4F_{3/2}$) lifetime of $\tau \sim 520$ μs compared to ~250 μs for Nd:YAG and ~100 μs for Nd:YVO_4 [10,11]. The resulting high energy storage capability makes Nd:YLF suitable to generate high pulse energies during *Q*-switched operation. However, the emission cross section σ_{em} at 1.3 μm for Nd:YLF is ~2–2.5 × 10^{-20} cm^2 (for the two polarizations), which is a factor of three less than that of Nd:YAG and an order of magnitude less than that of Nd:YVO_4 [11], which implies lower gain.

Power scaling Nd lasers at 1.3 μm are more difficult than at 1.0 μm because of the lower σ_{em}. The relatively longer lifetime τ of Nd:YLF partially compensates for this. The σ_{em} and τ values of Nd:YLF also necessitate a careful design of the pump beam radius where a trade-off has to be made between a reasonably low threshold and the risk of thermal fracture [5]. Thermal effects are especially problematic under 1.3 μm operation (compared to 1.0 μm operation) due to the larger quantum defect. By using a relatively low Nd doping, one can reduce upconversion and spread out the thermal load longitudinally in the crystal, which increases the thermal fracture pump limit [4,5,12].

Nd-doped active media are suitable for an efficient *Q*-switched operation at 1.3 μm using a V:YAG saturable absorber because they have a high ratio $\alpha = \sigma_{GSA}/\sigma_{em}$, with σ_{GSA}, the ground-state absorption cross section of the saturable absorber and σ_{em} the emission cross section of the laser crystal [13]. It has been demonstrated that V:YAG operates efficiently as a saturable absorber for Nd lasers operating in the 1.0 and 1.3 μm bands. Nd:YAG, Nd:YVO_4, Nd:YAP, Nd:KGW, Nd:$GdYVO_4$, and Nd:GGG have previously been passively *Q*-switched with V:YAG at 1.3 μm [13–21]. To the best of our knowledge, V:YAG has not been used to passively *Q*-switch Nd:YLF lasers at either 1.0 or 1.3 μm. Considering other diode end-pumped 1.3 μm Nd lasers passively *Q*-switched with V:YAG, the highest average power was 2.1 W for Nd:YVO_4 [13] while Nd:YAG delivered the highest energy per pulse of 126 μJ and peak power of 6.1 kW in different setups [18]. Nd:YLF has the potential to significantly increase the pulse energy due to its longer upper-laser-level lifetime [5,22].

Here we demonstrate high-power 1314 nm operation of a diode end-pumped Nd:YLF laser in both CW and passively *Q*-switched modes.

The linear two mirror resonator (Fig. 1) consists of a 300 mm concave input coupler (IC) mirror which is highly reflective at 1314 nm and is highly transmissive

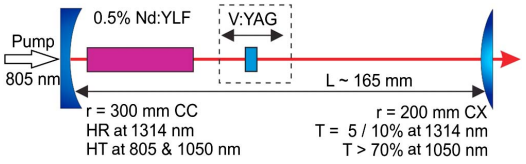

Fig. 1. (Color online) Experimental resonator layout for CW and a passively *Q*-switched (with V:YAG) operation.

0146-9592/13/060980-03$15.00/0

at 805 nm. Two 200 mm convex output couplers (OCs) with transmissions of 5% and 10% at 1.3 μm were available and placed ~165 mm from the IC. Operation was forced onto the 1.3 μm line by specifying both the IC and OC to be highly transmissive at ~1 μm. The size of the fundamental laser mode in the crystal was adjusted at full pump power to match the pump beam by adjusting the position of the OC.

The laser crystal consisted of a single 0.5% doped a-cut Nd:YLF rod which was 5 mm in diameter and 30 mm in length. It was mounted in a water-cooled copper block with its *c*-axis horizontally and was placed next to the IC. The laser crystal was end-pumped from one side with a fiber-coupled diode laser module (Jenoptik JOLD-140-CAXF, 0.6 mm, 0.22 NA fiber, ~805 nm) with the pump power limited to ~45 W to avoid thermal fracture. The pump beam was focused to a waist radius of ~700 μm in the center of the gain medium and had a roughly bell-shaped energy distribution. This waist radius was determined with a gain optimization method similar to the one described in [5] because both the pump and laser beam radii have a strong influence on the gain as well as on the thermal load. In this method, we also set the parameters so that the threshold would be at about 25% of the maximum pump power.

The CW slope efficiencies of the oscillators with the two OCs are shown in Fig. 2. The most efficient CW operation, as well as highest output power, was achieved with a 5% OC with a resulting slope efficiency of 29%. This laser had an incident pump power threshold of 9.25 W and a maximum power output of 10.4 W, which is 1.7 times higher than recently reported [3]. The beam had a symmetrical Gaussian profile, but at the maximum pump power the beam became slightly elliptical with the horizontal radius being ~25% larger than the vertical. This was due to the YLF's astigmatic thermal lensing [23]. Wavelength measurements showed oscillation only at 1314 nm on the σ polarization due to the oscillator being unstable for the stronger negative thermal lenses associated with the π polarization [8,9].

The 5% OC oscillator was subsequently passively *Q*-switched by inserting a 3 mm thick V:YAG saturable absorber with an initial single pass absorption of ~3% in the cavity between the gain medium and OC (Fig. 1). The V:YAG crystal was cut along [111] to avoid anisotropy. Initial experiments indicated that the pulsed performance at various input powers was relatively insensitive to the position of the V:YAG *Q*-switch and the *Q*-switch was subsequently placed ~12 mm from the Nd:YLF crystal. The incident pump-power threshold of the *Q*-switched laser was 17.5 W, and the maximum average output power was 5.2 W at an incident pump power of 45.2 W (Fig. 3). As the incident pump power was increased from threshold to 27 W, the pulse repetition frequency (PRF) increased from 650 Hz to 5.9 kHz, after which the PRF stayed nearly constant at ~6.3 kHz with increasing incident power (Fig. 3). Thermal lensing of both the Nd:YLF and V:YAG crystals change the laser-beam size within the resonator, which in turn influences the bleaching properties of the V:YAG crystal. This gives rise to a nonlinear behavior in the pulse repetition rate [24]. The constant PRF over a range of high powers may be a desirable characteristic for some applications.

Pulse duration at full width at half-maximum decreased from 162 to 136 ns with increasing pump power (Fig. 4). The increase in average output power and almost constant PRF above 27 W resulted in an increase in pulse energy up to 825 μJ (Fig. 4) with a peak power of 6.1 kW. Energy per pulse and average power was higher than previously reported with other diode-end-pumped

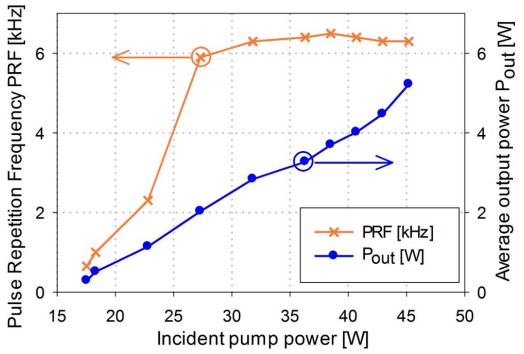

Fig. 3. (Color online) Passively *Q*-switched behavior: PRF (left axis) and average output power (right axis).

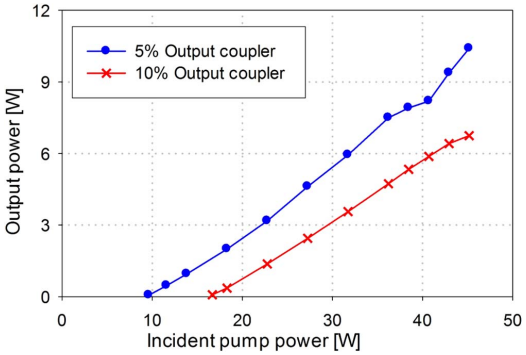

Fig. 2. (Color online) Slope efficiencies of the CW laser for the different OCs used.

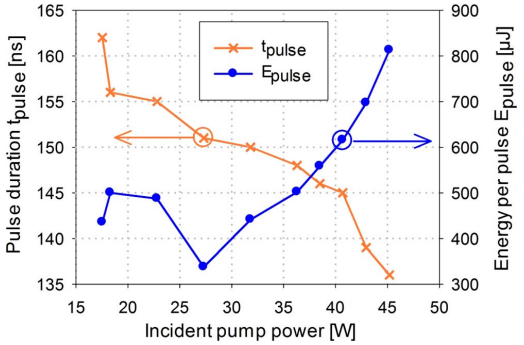

Fig. 4. (Color online) Passively *Q*-switched behavior: pulse duration (left axis) and energy per pulse (right axis).

passively *Q*-switched 1.3 μm Nd lasers with V:YAG: by 6.5 times (126 μJ with Nd:YAG) [18]) and 2.5 times (2.1 W with Nd:YVO_4 [13]), respectively.

In conclusion, high average power 1314 nm oscillation of an Nd:YLF laser was demonstrated for CW operation and delivered up to 10.4 W of output power. Passively *Q*-switched operation of an Nd:YLF laser using a V:YAG saturable absorber was demonstrated for the first time. Pulsed operation delivered 825 μJ of energy per pulse with a pulse duration of 135 ns and an average power of 5.2 W. These results are, to the best of our knowledge, the highest reported values for all diode-end-pumped passively *Q*-switched 1.3 μm Nd lasers with V:YAG.

References

1. J. T. Murray, R. C. Powell, N. Peyghambarian, D. Smith, W. Austin, and R. A. Stolzenberger, Opt. Lett. **20**, 1017 (1995).
2. Y. Louyer, M. D. Plimmer, P. Juncar, M. E. Himbert, F. Balembois, and P. Georges, Appl. Opt. **42**, 4867 (2003).
3. Y. Wei, S. Xu, C. Huang, F. Zhuang, W. Chen, L. Huang, X. Wang, and G. Zhang, Laser Phys. **22**, 1029 (2012).
4. W. A. Clarkson, P. J. Hardman, and D. C. Hanna, Opt. Lett. **23**, 1363 (1998).
5. C. Bollig, C. Jacobs, M. J. D. Esser, E. H. Bernhardi, and H. M. von Bergmann, Opt. Express **18**, 13993 (2010).
6. C. Du, S. Ruan, H. Zhang, Y. Yu, F. Zeng, J. Wang, and M. Jiang, Appl. Phys. B **80**, 45 (2005).
7. D. Sauder, A. Minassian, and M. J. Damzen, Opt. Express **15**, 3230 (2007).
8. M. Pollnau, P. J. Hardman, M. A. Kern, W. A. Clarkson, and D. C. Hanna, Phys. Rev. B **58**, 16076 (1998).
9. P. J. Hardman, W. A. Clarkson, G. J. Friel, M. Pollnau, and D. C. Hanna, IEEE J. Quantum Electron. **35**, 647 (1999).
10. J. R. Ryan and R. Beach, J. Opt. Soc. Am. B **9**, 1883 (1992).
11. C. Czeranowsky, "Resonatorinterne Frequenzverdopplung von diodengepumpten Neodym-Lasern mit hohen Ausgangsleistungen im blauen Spektralbereich," Ph.D. dissertation (University of Hamburg, 2002).
12. C. Bollig, C. Jacobs, H. M. von Bergmann, and M. J. D. Esser, in *CLEO/Europe 2005 Conference on Lasers and Electro-Optics Europe* (IEEE, 2005), p. 14.
13. J. K. Jabczyński, K. Kopczyński, Z. Mierczyk, A. Agnesi, A. Guandalini, and G. Reali, Opt. Eng. **40**, 2802 (2001).
14. V. P. Mikhailov, N. V. Kuleshov, N. I. Zhavoronkov, P. V. Prokohsin, K. V. Yumashev, and V. A. Sandulenko, Opt. Mater. **2**, 267 (1993).
15. A. M. Malyarevich, I. A. Denisov, K. V. Yumashev, V. P. Mikhailov, R. S. Conroy, and B. D. Sinclair, Appl. Phys. B **67**, 555 (1998).
16. A. S. Grabtchikov, A. N. Kuzmin, V. A. Lisinetskii, V. A. Orlovich, A. A. Demidovich, K. V. Yumashev, N. V. Kuleshov, H. J. Eichler, and M. B. Danailov, Opt. Mater. **16**, 349 (2001).
17. A. V. Podlipensky, K. V. Yumashev, N. V. Kuleshov, H. M. Kretschmann, and G. Huber, Appl. Phys. B **76**, 245 (2003).
18. J. Sulc, Proc. SPIE **5460**, 292 (2004).
19. J. Janousek, P. Tidemand-Lichtenberg, J. L. Mortensen, and P. Buchhave, Opt. Commun. **265**, 277 (2006).
20. C. Zuo, B. Zhang, Y. Liu, J. He, H. Huang, J. Yang, and J. Xu, Laser Phys. **20**, 1717 (2010).
21. T. Omatsu, K. Miyamoto, M. Okida, A. Minassian, and M. Damzen, Appl. Phys. B **101**, 65 (2010).
22. W. Koechner, *Solid-State Laser Engineering* (Springer, 2006).
23. H. Vanherzeele, Appl. Opt. **28**, 4042 (1989).
24. X. Li, G. Li, S. Zhao, K. Yang, T. Li, G. Zhang, K. Cheng, and X. Wang, Opt. Laser Technol. **44**, 929 (2012).

Appendix B

High average power Q-switched 1314 nm two-crystal Nd:YLF laser

High average power *Q*-switched 1314 nm two-crystal Nd:YLF laser

R. C. Botha,[1,2,*] W. Koen,[3] M. J. D. Esser,[3,4] C. Bollig,[3,5] W. L. Combrinck,[1,6] H. M. von Bergmann,[2] and H. J. Strauss[3]

[1]*HartRAO, P.O. Box 443, Krugersdorp, 1740 South Africa*

[2]*Stellenbosch University, P/Bag X1, Matieland, 7602 South Africa*

[3]*National Laser Centre, CSIR, PO Box 395, Pretoria, 0001 South Africa*

[4]*Formerly at CSIR, now at Heriot-Watt University, EH14 4AS Edinburgh, UK*

[5]*Formerly at CSIR, now at Abacus Laser, Göttingen, Germany*

[6]*Department of Geography, Geoinformatics and Meteorology, University of Pretoria, Pretoria 0132, South Africa*

**Corresponding author: roelf@hartrao.ac.za*

Received October 28, 2014; revised December 18, 2014; accepted December 25, 2014;
posted January 7, 2015 (Doc. ID 225843); published February 5, 2015

A 1314 nm two-crystal Nd:YLF laser was designed and operated in both CW and actively *Q*-switched modes. Maximum CW output of 26.5 W resulted from 125 W of combined incident pump power. Active *Q*-switching was obtained by inserting a Brewster-cut acousto optic modulator. This setup delivered an average power of 18.6 W, with a maximum of 5.6 mJ energy per pulse with a pulse duration of 36 ns at a pulse repetition frequency of 500 Hz. © 2015 Optical Society of America

OCIS codes: (140.0140) Lasers and laser optics; (140.3070) Infrared and far-infrared lasers; (140.3480) Lasers, diode-pumped; (140.3530) Lasers, neodymium; (140.3540) Lasers, Q-switched.
http://dx.doi.org/10.1364/OL.40.000495

High-power 1.3 μm lasers have a wide range of applications, including communications, remote sensing, timing systems, and display technology [1–4]. The 1.3 μm output can be Raman-shifted to the 1.5 μm region, which is useful for applications requiring eye-safe operation at high powers such as lidar and free-space optical communication [1]. Furthermore, 1314.0 nm (specifically the 657.0 nm second harmonic) is required to probe the relevant transition for optical calcium clocks [2]. Harmonic conversion of 1.3 μm can also be used for the generation of red and blue light which is used in display technologies [3,4].

The stronger 1.3 μm emission lines of Nd:YLF are at 1314 nm for the σ-polarization and 1321 nm for the π-polarization. Operating an end-pumped Nd:YLF laser at 1.3 μm is attractive because of the weak thermal lens when emitting on the σ-polarization [5,6]. This results in excellent beam quality over a wide range of output powers.

The upper-laser-level ($^4F_{3/2}$) lifetime of $\tau \sim 520$ μs for Nd:YLF is longer compared to ~250 μs for Nd:YAG and ~100 μs for Nd:YVO_4 [7,8]. The resulting high energy storage capability makes Nd:YLF suitable for generating high pulse energies during *Q*-switched operation [7–10]. The emission cross section (σ_{em}) at 1.3 μm for Nd:YLF is ~2–2.5 × 10^{-20} cm^2 (for both polarizations). This σ_{em} is about an order of magnitude less than for the strongest Nd:YLF emission lines at 1.0 μm and is also a factor of 3 less than that of Nd:YAG at 1.3 μm and an order of magnitude less than 1.3 μm σ_{em} for Nd:YVO_4 [8]. Because of this low σ_{em} for 1.3 μm Nd:YLF, power scaling such lasers is more difficult than for either 1.0 μm Nd:YLF or other Nd-doped media at 1.3 μm. The relatively longer upper-laser-level lifetime τ of Nd:YLF however partially compensates for this.

The σ_{em} and τ values of Nd:YLF necessitate a careful design of the pump beam radius in pulsed lasers where a trade-off has to be made between a reasonably low threshold and the risks of optical damage and thermal fracture [9]. Thermal effects are especially problematic under 1.3 μm operation (compared to 1.0 μm) because of the larger quantum defect. By using a relatively low Nd doping, one can reduce upconversion and spread out the thermal load longitudinally in the crystal, which increases the thermal fracture pump limit [9,11,12]. Furthermore, Nd:YLF crystals grown by the Czochralski method have a longitudinal gradient in doping resulting from the physical crystal growth process. Pumping from the lower-doping side of the crystal further lowers the risk of thermal fracture [13].

We previously reported the highest 1.3 μm continuous wave (CW) output power from a diode-*end*-pumped Nd:YLF laser of 10.4 W and the highest energy per pulse of 825 μJ for a *passively* *Q*-switched Nd:YLF 806 nm *end*-pumped setup [14]. Recent 1.3 μm Nd:YLF work by other groups based on *side*-pumped setups delivered CW powers of up to 14.9 W [15] and for *actively* *Q*-switched Nd:YLF pumped at 796 nm average powers of up to 12.3 W (from 180 W of pump power) with corresponding pulse energies of 3.8 mJ [16].

Here we demonstrate high-power 1314 nm operation of a diode end-pumped Nd:YLF laser in both CW and actively *Q*-switched modes.

The resonator used for CW operation at 1314 nm is shown in Fig. 1. It consists of an $r = 200$ mm concave back reflector (BR) and a flat 10% transmission output coupler (OC). The resonator was folded with a flat mirror (HR at 1314 nm, HT at 806, 1050 nm) to pump both crystals. Operation was forced onto the 1.3 μm emission line by specifying both the input and output couplers to be highly transmissive at ~1 μm. Mode-matching at full pump power was achieved by adjusting the positions of the OC and BR.

The Nd:YLF laser crystals were obtained through a collaboration with VLOC, who estimated the doping gradient of a specially manufactured boule and maintained

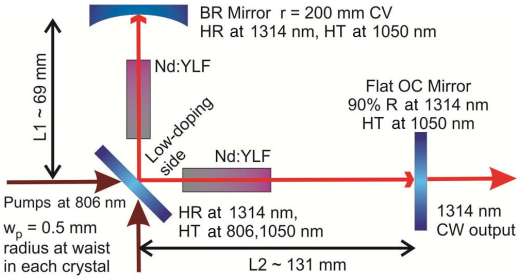

Fig. 1. Experimental resonator layout for CW operation.

the crystal orientation information during the manufacturing process. The two crystals used were a-cut rods with 6 mm diameter and 45 mm length; each had a linear doping gradient along the rod from 0.30% to 0.52%. Each crystal was mounted in a water-cooled copper block with its c-axis horizontal and placed next to the resonator folding mirror. The laser crystals were end-pumped from the low-doping (0.30%) side using fiber-coupled diode laser modules (Jenoptik JOLD-75-CPXF-2 P, 0.4 mm 0.22 NA fiber, ~808 nm) with the pump powers each limited to ~62.5 W (125 W total) to avoid thermal fracture. The laser diodes were also temperature controlled to 27°C to provide a pump wavelength of 805.5 nm (at full pump power), ensuring an absorption efficiency of ~91.5% in this setup. The pump beam was focused to a waist radius of ~500 μm in the center of the gain medium with a roughly top-hat shaped energy distribution at that position. This waist radius was determined through a gain optimization method similar to the one described in [9] since both the pump and laser beam radii have a strong influence on the gain as well as on the thermal load.

The CW incident optical-to-optical slope efficiency of the oscillator is shown in Fig. 2. The most efficient CW operation, as well as highest output power, was achieved with a 10% OC with a resulting incident optical-to-optical slope efficiency of 25%. This laser had an incident pump power threshold of 15.3 W and a maximum power output of 26.5 W, which is 2.5 times higher than what was recently reported by our group [14]. Wavelength measurements showed oscillation only at 1314 nm on the σ-polarization because of the oscillator being unstable

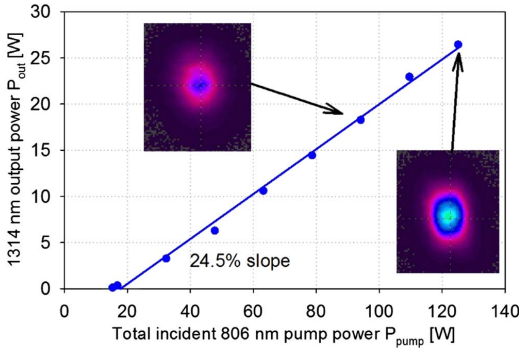

Fig. 2. Incident 806 nm optical-to-optical slope efficiency, together with beam profiles of the 1314 nm CW laser.

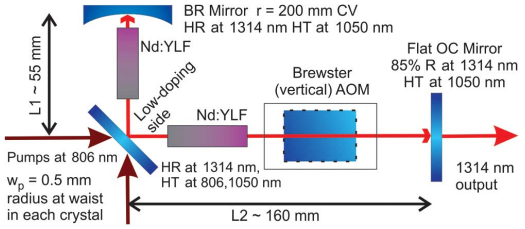

Fig. 3. Experimental resonator layout for actively Q-switched (with AOM) operation.

for the stronger negative thermal lenses associated with the π-polarization [5,6]. The beam mostly had a symmetrical Gaussian profile, but at the maximum pump power it became slightly elliptical with a horizontal radius ~20% smaller than the vertical. This is because of the YLF's astigmatic thermal lensing [17]. The beam was measured by the ISO11146 method (knife-edge) to have an M^2 value of 2.0 (horizontal) and 2.6 (vertical).

The oscillator in our setup was subsequently slightly modified for active Q-switched operation. An acousto optic modulator (AOM) [a Brewster-cut Gooch & Housego, Model QS027-10M(BR)-NL6] was inserted in the cavity between the second Nd:YLF crystal and output coupler (Fig. 3). The flat OC's transmission was increased to 15% to limit the intra-cavity peak power which, in turn, allowed us to operate at a low pulse repetition frequency (PRF). The positions of the BR and OC were also slightly adjusted to mode-match the pump and laser modes within the Nd:YLF crystals.

A maximum average output power of 18.6 W was achieved at an incident pump power of 125 W and a PRF of 20 kHz (Fig. 4). The energy per pulse E_{pulse} increased from 0.93 mJ at a PRF of 20 kHz, to 5.59 mJ at 0.5 kHz. Pulse duration at full width at half-maximum (FWHM) decreased from 218 ns at a PRF of 20 kHz to 36 ns for 0.5 kHz (Fig. 5). The highest peak output power was 155 kW at a PRF of 0.5 kHz. A slight elliptical beam profile was observed because of astigmatic thermal lensing [17]. The decrease in the maximum output power from that of the CW setup is attributed to the increase of OC losses, as well as a slight change in the mode-matching

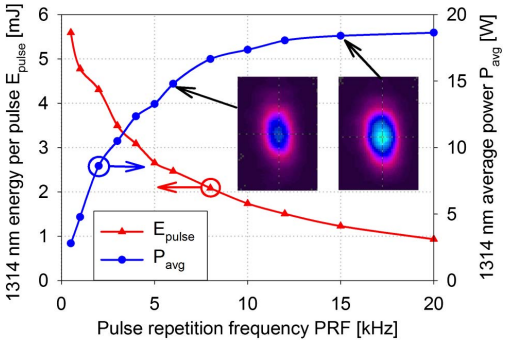

Fig. 4. Actively Q-switched behavior at full pump power of 125 W: Energy per pulse (left axis) and average output power (right axis), as a function of the PRF.

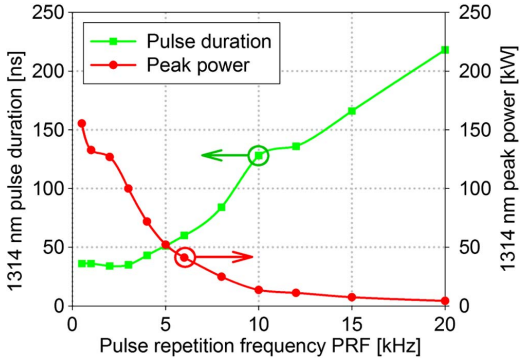

Fig. 5. Actively Q-switched behavior at full pump power of 125 W: Pulse duration (left axis) and peak power (right axis), as a function of the PRF.

which resulted from the additional optical element in the resonator.

This is, to the best of our knowledge, the first demonstration of an actively Q-switched *end*-pumped Nd:YLF laser at 1314 nm. The resulting energy per pulse and average power are also higher than previously reported for other diode *side*-pumped actively Q-switched 1.3 μm Nd:YLF lasers [16].

Subsequently, an attempt was made to increase the total pump power to 140 W. This resulted in one of the crystals fracturing at a PRF of 12.5 kHz, when decreasing it from 20 kHz. We therefore operated the laser just below the crystal damage threshold, since the increase in pump power resulted in a higher heat load (because of upconversion), which increased the stress inside the Nd:YLF above the fracture limit [9].

In conclusion, high average power 1314 nm oscillation of an end-pumped Nd:YLF laser has been demonstrated for CW operation delivering up to 26.5 W of output power. Active Q-switching of the laser using a Brewster-cut AOM resulted in pulsed operation with 5.59 mJ energy per pulse, pulse duration of 36 ns, and an average power of 18.6 W. These results are, to the best of our knowledge, the highest reported values to date for diode-*end*-pumped 1.3 μm Nd lasers.

R. C. Botha hereby acknowledges Inkaba yeAfrica (as managed by AEON-NMMU) for the partial financial support toward this research. This is Inkaba yeAfrica Publication No. 82.

References

1. J. T. Murray, R. C. Powell, N. Peyghambarian, D. Smith, W. Austin, and R. A. Stolzenberger, Opt. Lett. **20**, 1017 (1995).
2. Y. Louyer, M. D. Plimmer, P. Juncar, M. E. Himbert, F. Balembois, and P. Georges, Appl. Opt. **42**, 4867 (2003).
3. X. P. Hu, G. Zhao, Z. Yan, X. Wang, Z. D. Gao, H. Liu, J. L. He, and S. N. Zhu, Opt. Lett. **33**, 408 (2008).
4. S. Ngcobo, C. Bollig, C. Jacobs, and J. P. Burger, "Blue–violet frequency-tripled Nd:YLF ring laser for holography application," presented at South African Institute of Physics 50th Annual Conference, Pretoria (2005).
5. M. Pollnau, P. J. Hardman, M. A. Kern, W. A. Clarkson, and D. C. Hanna, Phys. Rev. B **58**, 16076 (1998).
6. P. J. Hardman, W. A. Clarkson, G. J. Friel, M. Pollnau, and D. C. Hanna, IEEE J. Quantum Electron. **35**, 647 (1999).
7. J. R. Ryan and R. Beach, J. Opt. Soc. Am. B **9**, 1883 (1992).
8. C. Czeranowsky, "Resonatorinterne Frequenzverdopplung von diodengepumpten Neodym-Lasern mit hohen Ausgangsleistungen im blauen Spektralbereich," Ph.D. thesis (University of Hamburg, 2002).
9. C. Bollig, C. Jacobs, M. J. D. Esser, E. H. Bernhardi, and H. M. von Bergmann, Opt. Express **18**, 13993 (2010).
10. W. Koechner, *Solid-State Laser Engineering* (Springer, 2006).
11. W. A. Clarkson, P. J. Hardman, and D. C. Hanna, Opt. Lett. **23**, 1363 (1998).
12. C. Bollig, C. Jacobs, H. M. von Bergmann, and M. J. D. Esser, in *CLEO/Europe 2005 Conference on Lasers and Electro-Optics Europe* (IEEE, 2005), p. 14.
13. C. Bollig, W. Koen, H. Strauss, E. H. Bernhardi, R. Botha, D. Esser, and D. R. Preussler, in *3rd EPS-QEOD Europhoton Conference* (European Physical Society, 2008).
14. R. C. Botha, H. J. Strauss, C. Bollig, W. Koen, O. Collett, N. V. Kuleshov, M. J. D. Esser, W. L. Combrinck, and H. M. von Bergmann, Opt. Lett. **38**, 980 (2013).
15. A. M. Deana, M. A. P. A. Lopez, and N. U. Wetter, Opt. Lett. **38**, 4088 (2013).
16. S. Liu, L. Dong, B. Zhang, J. He, Z. Wang, J. Ning, R. Wang, and X. Liu, Chin. Opt. Lett. **12**, 031402 (2014).
17. H. Vanherzeele, Appl. Opt. **28**, 4042 (1989).